Marine X-band radar derived wave field quality on an ebb tidal delta

Master Thesis
2nd Version

Jantien Rutten
3402169

Supervisors
dr. B.G. Ruessink
ir. C. Gautier
ir. C. Swinkels

18-01-2013
Universiteit Utrecht
Departement Fysische Geografie
Faculteit Geowetenschappen

Universiteit Utrecht

Deltares
Enabling Delta Life

SEA DARQ

Cover: Benson Beach (Oregon), 2012.

Table of contents

1. Introduction

The marine radars at ships or positioned along the shoreline monitoring the sea surface for navigational purposes, can be used to observe waves. In their navigational images noise arises by the interaction of the electromagnetic signal with the small wind ripples at the sea surface, known as sea clutter. This sea clutter has been used for sea surface monitoring for a few decades (for example Hasselman et al., 1978; Shemdin et al., 1978). 3D Fast Fourier Transforms on time sequences of wavy sea clutter images provides wave field, current and bathymetric information, with large spatial and temporal coverage. Such remote sensing devices imaging coastal zones may be preferred over in-situ instruments (e.g. velocity sensor, wave buoy) measuring at a limited number of locations.

Yet algorithms to derive wave, current and bathymetric information have not yet reached an operational status and are surrounded by considerable uncertainty and lack of robustness, especially in complicated morphological settings. We study the sea surface using radar data collected by the radar system located at the lighthouse of Ameland, monitoring the tidal inlet and the ebb tidal delta, a prime example of a complicated morphological setting.

Ebb or flood tidal deltas are sub- or intertidal sand bodies seaward and shoreward of a tidal inlet, in between two barrier islands. The tidal inlet connects the sea with the tidal basin, which contains (flood- or ebb-dominated) channels and shoals. Behind the narrow tidal inlet the tidal current diverges and sediment deposits, resulting in such deltas. Erosion or accretion of a specific location at the shoreline is related to the shape of the ebb delta and to the distance from the tidal inlet (Oertel, 1977). Shi et al. (2011) found from a modelling study, that near-shore net circulations drive shoreline changes. Robin et al. (2009) observed shoreline changes in the neighbourhood of an ebb delta.

In the Netherlands, by law the Kader Richtlijn Kustlijn demands preservation of the shoreline to protect the densely populated and highly cultivated country. Measures such as nourishments or hard structures (dikes, groynes) should protect for shoreline retreat. However, shorelines might be preserved and protected more effectively when the hydrodynamic and morphodynamic processes around the delta are better known, which can be achieved by measuring and modelling. In the framework of the SBW-HL (‘Strength and Loading of Water Defences- Hydraulic Loads’) project 2011-2016, numerical models have to be improved that are used to derive the Hydraulic Loads for primary sea or flood defense safety prediction.

Numerical models can be improved by validation to ground-truth measurements. Swinkels (2011) used radar inferred currents to validate a hydrodynamic model in Delft3D of the Ameland Inlet. Similarly, Gautier and Westhuysen (2010) compared radar inferred wave field

data to SWAN model runs. Unfortunately, wave data appeared more complicated to compare than currents, partly because wave height cannot be obtained directly from the radar images. Thus for proper model validation, the quality of the marine (X-band) radar wave field should be known beforehand. Coastal monitoring by radar prescribes image processing techniques different from radar monitoring in deep water (Young et al. (1985), Nieto Borge et al. (2004)) and therefore brings new difficulties to derive radar inferred wave fields. Wave field quality will vary more in the complicated morphology of the coastal zone than in deep water where the morphology and the hydrodynamics is more consistent.

The aim of this thesis is to estimate temporal and spatial wave field quality variability in marine X-band radar images from the Ameland Inlet for two storms in 2010, to determine the appropriateness of radar images as a validation tool for a wave model of a complex bathymetry.

The outline of this thesis is as follows. Section 2 describes the most important literature about ebb delta systems and marine radars, required for this study. This literature study leads to the research questions introduced in Section 3. Section 4 describes the in-situ and radar data available, followed by the methods (Section 5) used to estimate radar wave field quality. The radar data is filtered for proper comparison to SWAN. Wave height is determined from radar image spectra using a Modulation Transfer Function. Then, radar wave field quality is estimated (Section 6) by predicting quality reduction factors, found by two methods; evaluating when and where the filter removes wave field outliers and comparing radar to SWAN wave fields. Finally, the results and potential improvements for future are discussed (Section 7) and concluded (Section 8).

2. Literature study

The concepts introduced here for the ebb tidal delta and for waves and currents in such systems will be of significance to the subsequent chapters.

2.1 Ebb tidal delta system

After a short introduction into barrier island coasts, this chapter zooms in on their individual morphological components and ebb tidal deltas in particular. Then, the hydrodynamic forcing and the largest sediment transport fluxes on and around the ebb tidal delta system are described.

Barrier island coasts are located at several locations over the world, for example the United States east coast, the Adriatic Sea and the German Bight (Ehlers 1988, in De Swart and Zimmerman, 2009). Generally, barrier(s) (islands) arise by drowning of the country behind the shoreline as a result of the rising sea level (Sha, 1989b) or due to sediment deposition by the interaction of wave- or tide-induced longshore and cross-shore currents. Barriers migrate landward, seaward and/or alonghore depending on sea level fluctuations, sediment availability and littoral drift. Along elongated barriers, tidal inlets can be formed due to breaching of the sea through the barrier, resulting in barrier islands. The scouring of the barrier breaches toward an inlet (Pacheco et al., 2010) depends on the stability of the small channel. Remaining prerequisites for barrier island formation are a mild sloping bottom, sufficient sediment supply and a certain tide and wave climate (Section 2.2).
In addition to barrier islands and tidal inlets, barrier island coasts hold back-barrier tidal basins and sandy shoals seaward and landward protruding from the tidal inlet, known as respectively ebb (outer) and flood (inner) tidal delta (Figure 2.1). Flood- and ebb- dominated channels connect the tidal basin with the inlet. Toward the mainland, those channels bifurcate into several small channels with intervening tidal flats. The watershed separates the tidal basin from adjacent tidal basins and indicates (tidal) flow reversal. To some degree, water may flow between adjacent basins.
The ebb tidal delta protrudes into the sea between 500m and 5km (De Swart and Zimmerman, 2009). Ebb tidal deltas have a similar volume as the adjacent barrier islands along mixed energy coasts, with both tidal and wave influence (FitzGerald, 1988). However, the ebb tidal delta is smaller when waves are more dominant. The ebb delta holds a sub-tidal terminal lobe at the ebb channel fan (Figure 2.1) (FitzGerald, 1988) with adjacent (intertidal) shoals and is bordered by one or two flood dominated channels. At the outer delta (dynamic) sand or swash bars could arise by wave forcing (FitzGerald, 1988). Elias and Van der Spek (2006) mention

the distal and proximal part of the ebb channel are respectively wave and tide dominated, when they modelled the decadal evolution of a tidal inlet system.

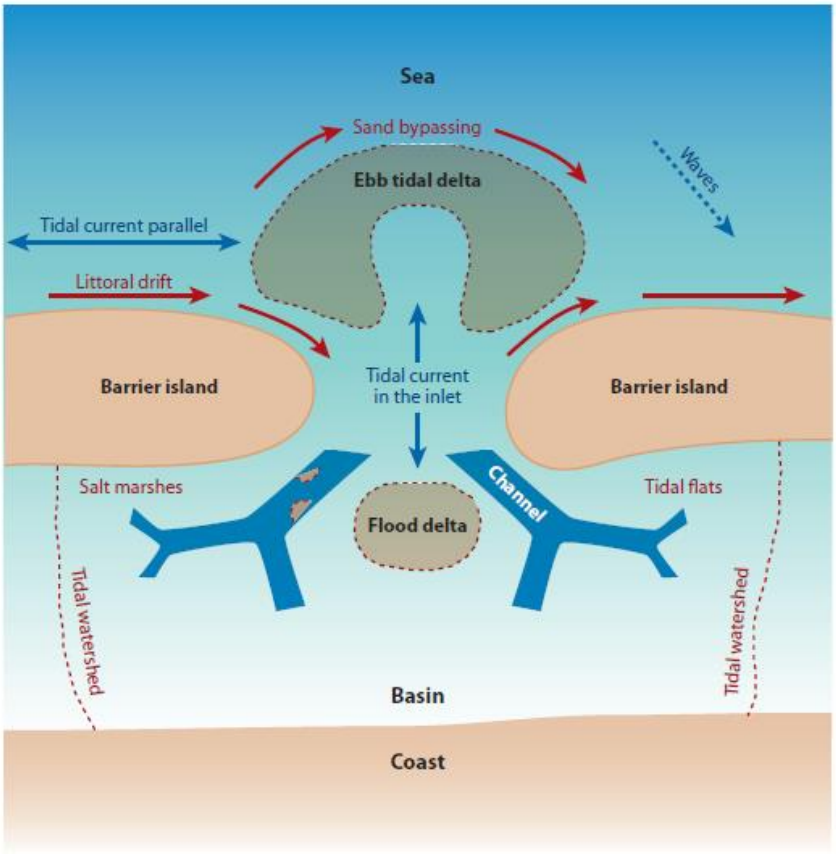

Figure 2.1. The main morphological components of a barrier island coast, with large scale water and sediment fluxes (De Swart and Zimmerman, 2009).

Generally, barrier island coasts arise at mixed-energy coasts, where the dominance of wave or tidal processes determines the specific barrier island and ebb delta development. Sha (1989b) showed that an increase of the tidal range results in a decrease of barrier island length. Then, the hydraulic gradient increases along the barrier island, inducing barrier breaching. Ebb tidal deltas are more pronounced in large (meso-) tidal ranges, while flood tidal deltas are small or absent. In contrast, in micro-tidal conditions, barrier islands are narrow and elongated and have pronounced flood deltas, but small or no ebb deltas.

The barrier coast morphology depends on the dominant wave or tide induced currents. Incident waves drive a current in a similar direction, the current bends away to alongshore in the near-shore zone. Tide induced currents are related to the geographic location (amphidromic system (Section 2.2.2)) of the study site. In Figure 2.1 tidal currents show a cross- and an alongshore component. The cross-shore current accelerates in the narrow inlet and decelerates seaward (and shoreward) of the inlet due to flow divergence. In those flow divergence zones an ebb and flood tidal delta arise (also due to bottom friction), since

sediment transport and sediment deposition is related to the dominant currents and velocity gradients. The mutual angle and ratio between incoming waves and the tidal currents determine the delta configuration and potentially delta asymmetry (Section 2.2.2, Figure 2.12) (Oertel, 1977; Sha, 1989b). The ebb tidal deltas can show an asymmetric shape, because the direction of the flood and ebb channels do not always correspond to the direction of inlet in- or outflow, which was observed by Sha. Sha (1989b) related the asymmetry of the ebb delta shape to wave or tide dominance.

Sediment is transported in the direction of the dominant currents. The net sediment transport parallel to the barrier islands is known as littoral drift. Nearby a tidal inlet this alongshore directed sediment flux is disturbed. Partially, sediment is transported into the tidal inlet and basin by the cross-shore tidal currents and partially the sediment transport continues alongshore, crossing the inlet (Cleveringa et al., 2004). The sediment transported from up- to down-drift of barrier islands is known as bypassing, first observed by Bruun and Gerritsen, 1959 (in FitzGerald, 1988). Bruun and Gerritsen (1959) (in FitzGerald, 1988) summarized three types of sediment bypassing; sand transport by waves, sand transport by tide (through tidal channels) and the migration of swash bars over the outer end of the ebb delta. FitzGerald (1988) studied the sediment bypassing more thoroughly and developed a sediment bypassing model building on the findings of Bruun and Gerritsen (1959) and follow-up studies. The model (FitzGerald, 1988) describes three types of sediment bypassing at different inlet types along mixed energy coasts: inlet migration and spit breaching, stable inlet processes and ebb tidal delta breaching (Figure 2.2). On the other hand, Bartholomä et al. (2010) found that sediment recirculates in the Otzum ebb tidal delta system between the German Bight barrier islands Langeoog and Spiekeroog. Sediment appears not to bypass this ebb tidal delta, proved by sedimentological sequences collected over the ebb tidal shoal.

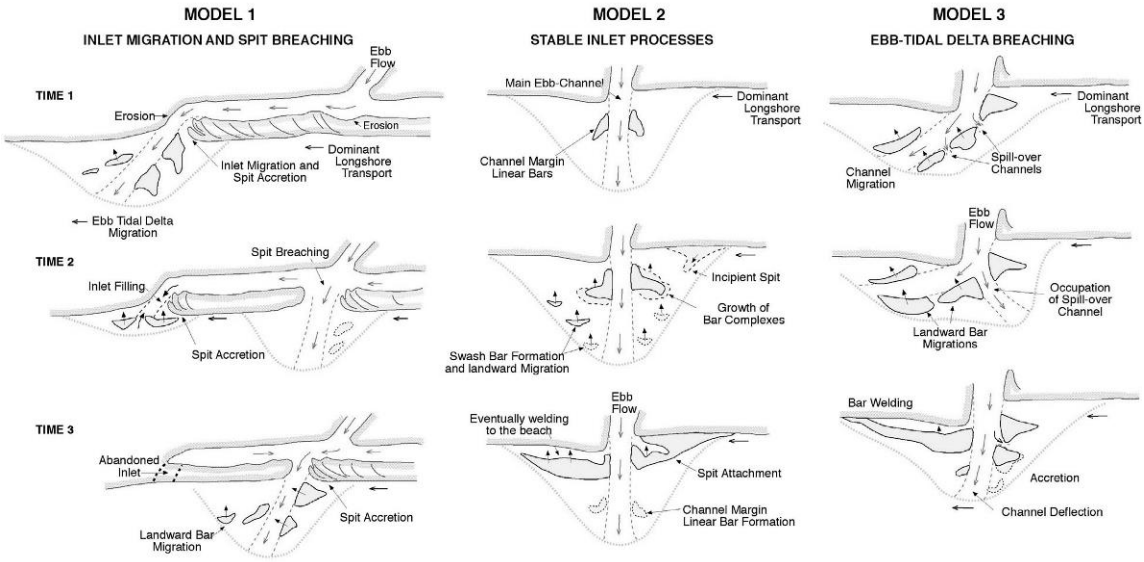

Figure 2.2. FitzGerald et al. (1978 and 1982 in FitzGerald 1988) distinguished three models for mixed energy coasts how sediment bypasses an inlet, in addition to the sediment bypassing mechanisms by Bruun and Gerritsen (1959). An inlet should not be fixed at one particular model, since an inlet can switch between the different models during larger timescales. When at a mixed energy coast the inlet throat is restricted (model 1), sediment bypasses and the inlet migrates by the successive build-up and welding of beach ridges resulting in a spit. At some moment, the spit will breach, so the inefficient long ebb channel resets to the original position. In model 2, the inlet is stable and sediment accumulates as swash bars by wave action at the distal part of the ebb delta. The bars migrate shoreward, decelerate, weld to each other and form bar complexes, which finally weld to the coast. In model 3, the inlet is stable, but sediment accumulates at the up-drift side of the inlet, bending the ebb channel down-drift by the dominant alongshore sediment transport. Similar to model 1 the ebb channel becomes inefficiently long and the ebb flow breaches through the ebb tidal delta. The remains of the ebb channel fills up with sediment and weld to the shore.

FitzGerald et al. (1984) observed swash bar migration over the ebb delta and finally bar welding to the down-drift barrier island. They found the ebb delta shape in combination with the inlet position determines the barrier morphology, when waves satisfy for swash bar migration. The ebb delta shape and inlet width determine the location of bar welding, resulting in barrier islands ranging from a ‘drumstick’ shape (increased width at up-drift end) to a further down-drift located cross-shore increased width (Figure 2.3).

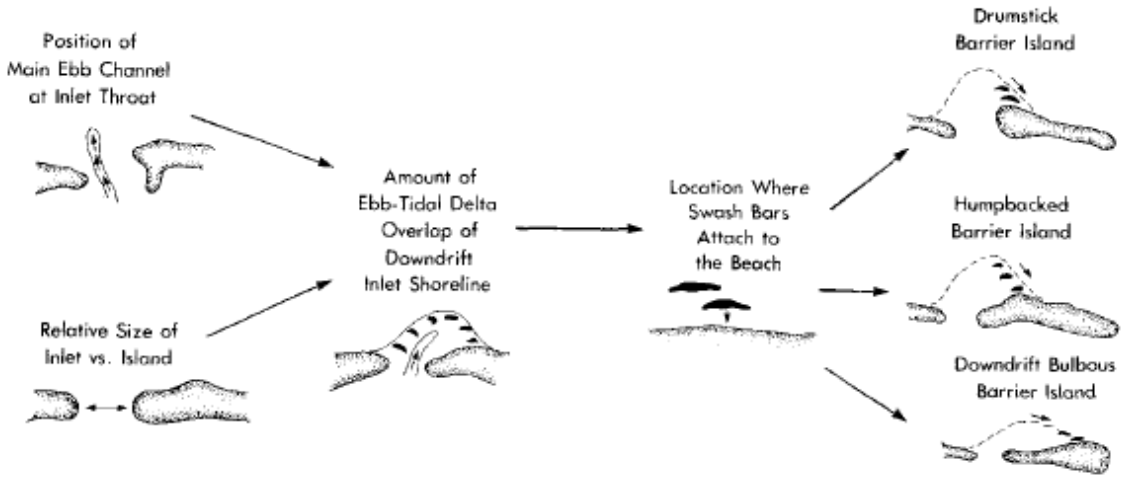

Figure 2.3. When the ebb channel is positioned down-drift in the tidal inlet or the inlet width is relatively large, then the swash bars weld down-drift to the barrier island as well. In contrast, the distance between inlet and location of swash bar welding decreases, when the ebb channel is located up-drift or the ebb channel is small. The barrier island shape varies from drumstick to down-drift bulbous due to the varying location of bar welding location (FitzGerald et al., 1984).

2.2 Hydrodynamics in the ebb delta system

The large scale wave and tide induced currents were mentioned in the previous section. This section describes waves propagating and deforming over the ebb tidal delta, followed by wave and tide driven currents.

2.2.1 Waves

Waves propagating through a water volume transfer energy to the water. The wave energy drives vertical and horizontal (orbital motion) water fluctuations. Wave energy E (J m^{-2}) is represented as

$$E = \tfrac{1}{8}\rho g H^2 \qquad (1)$$

with water density ρ (kg m^{-3}), gravity acceleration g (m s^{-2}) and wave height H (m).
Toward the shore, wave energy increases by shoaling and then dissipates due to wave breaking and bottom friction. In 1D frequency energy spectra these energy in- and decreases or frequency shifts by wave deformation can be noticed clearly (Figure 2.4). Besides, statistical (point) measures of the sea surface are derived from wave energy spectra, which are widely used to represent the sea state measured (wave buoys), but also to compute with numerical wave models (e.g. SWAN).

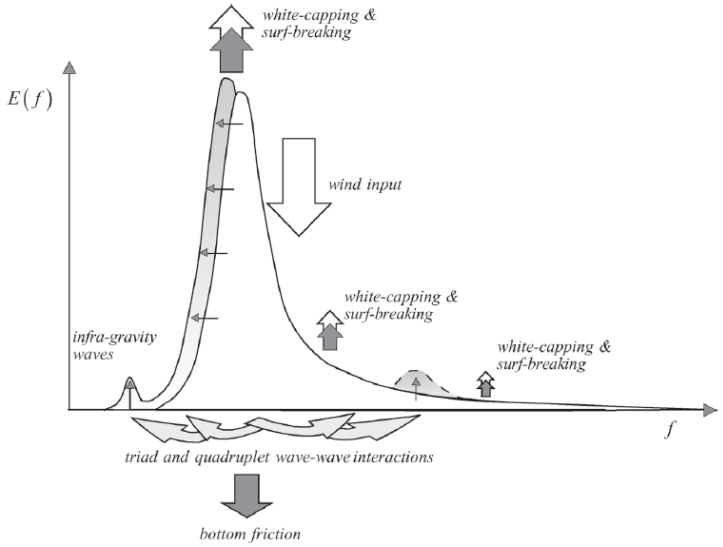

Figure 2.4 (Holthuijsen, 2007). The wave energy against frequency in shallow water. The wave energy peak increases during shoaling, low- and mid- frequent energy decreases by bottom friction, and energy decreases during wave breaking by breaker (white-capping and surf-breaking) dissipation. The spectrum slighlty gains energy at high frequencies. Energy is transferred to interference frequencies by triad and quadruplet wave-wave interactions.

Dispersion relation

Waves tend to disperse, assuming an irregular wave field in deep water where wave height and wave period differ. As long period or long (wavelength) waves propagate faster than short period and short waves, the long waves group over a larger distance and disperse from the shorter waves. So, over very large distances the wave field will transform to a regular or 'swell' wave field (Masselink and Hughes, 2003). The dispersion of waves is described in the dispersion relation, derived from the simplest mathematical representation of waves; linear wave theory (Masselink and Hughes, 2003). The dispersion relation reads

$$\omega = \sqrt{g\left|\vec{k}\right|\tanh\left|\vec{k}\right|h} + \vec{k}\vec{U} \qquad (2)$$

where ω is the angular frequency (Hz), $\vec{k}$ the wave number vector (m^{-1}), $\vec{U}$ the current vector ($m\ s^{-1}$) and h the water depth (m). The second term represents a shift of the still water dispersion relation due to a current.

Wave celerity c ($m\ s^{-1}$) follows from the equations above

$$c = \frac{\omega}{\vec{k}} \qquad (3)$$

The dispersion relation is the simplest equation to predict wave propagation for an irregular wave field. However, in shallower water higher order equations are needed to describe accurately the wave motion, since waves become affected by the sea bottom. Waves deform from sinuous symmetric waves (similar wave crest and trough height) toward asymmetric. The wave crest steepens and skews, the wave trough flattens. Thereby, the shoreward velocity (under the wave crest) increases, but the *duration* the water propagates onshore decreases. The seaward velocity (under the wave trough) decreases but water propagates off-shore for longer. This asymmetry cannot be represented optimally anymore by linear wave theory. A well- known higher-order mathematical formulation representing (non-linear) waves is the second order Stokes theory. In contrast to symmetric waves, the sediment transport direction does not reverse continually under asymmetric waves, so (net) sediment is transported and may change morphology.

2.2.1.1 Wave deformation

Waves deform and become asymmetric in shallow water due to the effect of the bottom on the waves, as described in the next seven subsections.

Shoaling

Waves grow when the waves start 'feeling' the sea bottom, known as shoaling. When waves 'feel' the sea bed, their propagation velocity decreases. Then, the water particles (and wave energy (Figure 2.4)) start to accumulate and the water level increases, since water particles cannot be compressed. In the complex bathymetry of an ebb tidal delta system, waves shoal at the steep edge of the ebb tidal delta and near the shorelines of the barrier island coasts (Figure 2.5). Taking tide into account complicates the prediction of shoaling zones, because the location of 'feeling the bottom' shifts during the tidal cycle.

Reflection

Obliquely incident waves can reflect partly back to sea under a similar angle, when hitting a feature or (sloping or vertical) surface or by an abrupt change in the sea bottom slope. Wave reflection is negligible at weak sloping beaches without surging waves. Van Rijn (1989) mentions reflection is negligible at beaches with a slope between 1: 100 and 1: 150. When a wave reflects, a standing wave arises and the wave height increases by the interaction of the incoming and the reflected wave. The ratio of reflected wave energy depends on the bottom slope, roughness, wave height and wave length (the last two parameters are combined in the wave steepness parameter). Low or long (infra- gravity) waves reflect more. Moreover, more waves reflect at steep surfaces. Summarizing these findings, wave reflection seems to be

negligible at the weak slopes of an ebb tidal delta system, but waves could reflect at the steeper edge of the ebb delta and perhaps at the steeper beaches of the barrier island heads (Figure 2.5). In addition, field measurements have shown that infra-gravity waves reflect at least partly at the north-west part of the Dutch barrier island Ameland (De Bakker, 2012).

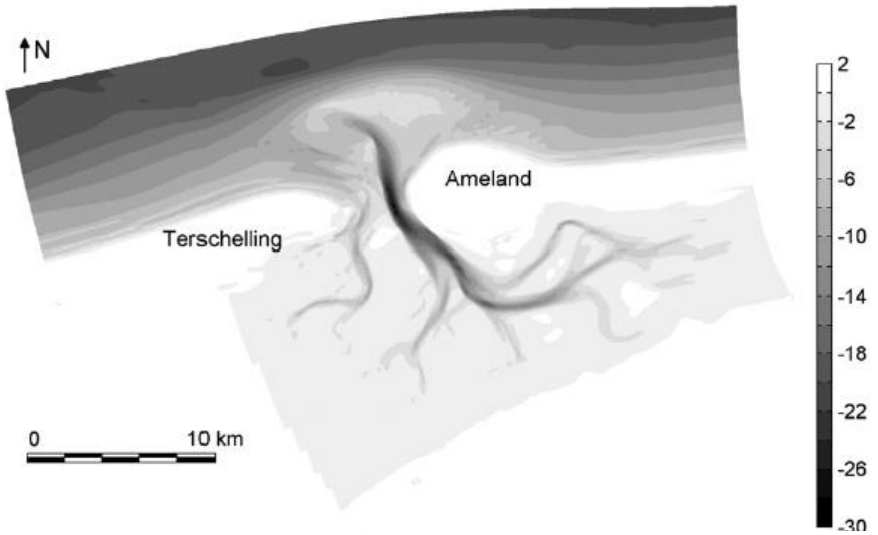

Figure 2.5. An example of an ebb tidal delta system bathymetry, depth (m) in color scale; the Ameland Inlet, The Netherlands (De Fockert et al., 2008 in Dissanayake et al., 2009), derived from field measurements in 2004. Bathymetry and particularly the bottom gradients are an important factor in wave deformation.

Refraction

The propagation speed of waves depends on the water depth (dispersion relation). Waves travel faster in deeper water than in shallower water. Assuming depth contours parallel to the shoreline and an obliquely incident wave, the seaward part of the wave crest travels faster than the shoreward wave crest. The wave crest bends toward the shore (normal to the depth contours) by the difference in propagation velocity. This change in wave direction is also known as refraction. Waves refract differently alongshore in a more complex bathymetry. There, the energy of the wave converges (or focuses) and diverges (or spreads) alongshore. The wave height increases or decreases with, respectively, an increase or decrease in the wave energy alongshore. This is illustrated by measurements performed near the ebb tidal delta in front of the San Francisco Bay (Shi et al., 2011), where waves enter the adjacent coasts from different directions alongshore and the wave height differs alongshore, both due to refraction. Shi et al. (2011) modelled waves and current patterns nearby this ebb tidal delta and noticed waves focus at the adjacent beaches (Figure 2.6). Bertin et al. (2009) observed in their numerical morphodynamic model a net force directed into the inlet of the wave-dominated Óbidos Lagoon (Portugal), due to wave refraction around the ebb tidal delta (Figure 2.9). Besides, waves may refract on currents, known as wave-current refraction. A current can weaken (enhance) the wave propagation speed. Then, the wave crest bends toward (away

from) the current, because the wave crest propagates with a different velocity. Wave-current refraction may be important near the ebb- and flood channels of an ebb tidal delta system.
A particular case of refraction (and reflection) is wave trapping, which is successive reflection and refraction of a wave along a shore. When waves are reflected (with a certain angle), waves refract again toward the shore.

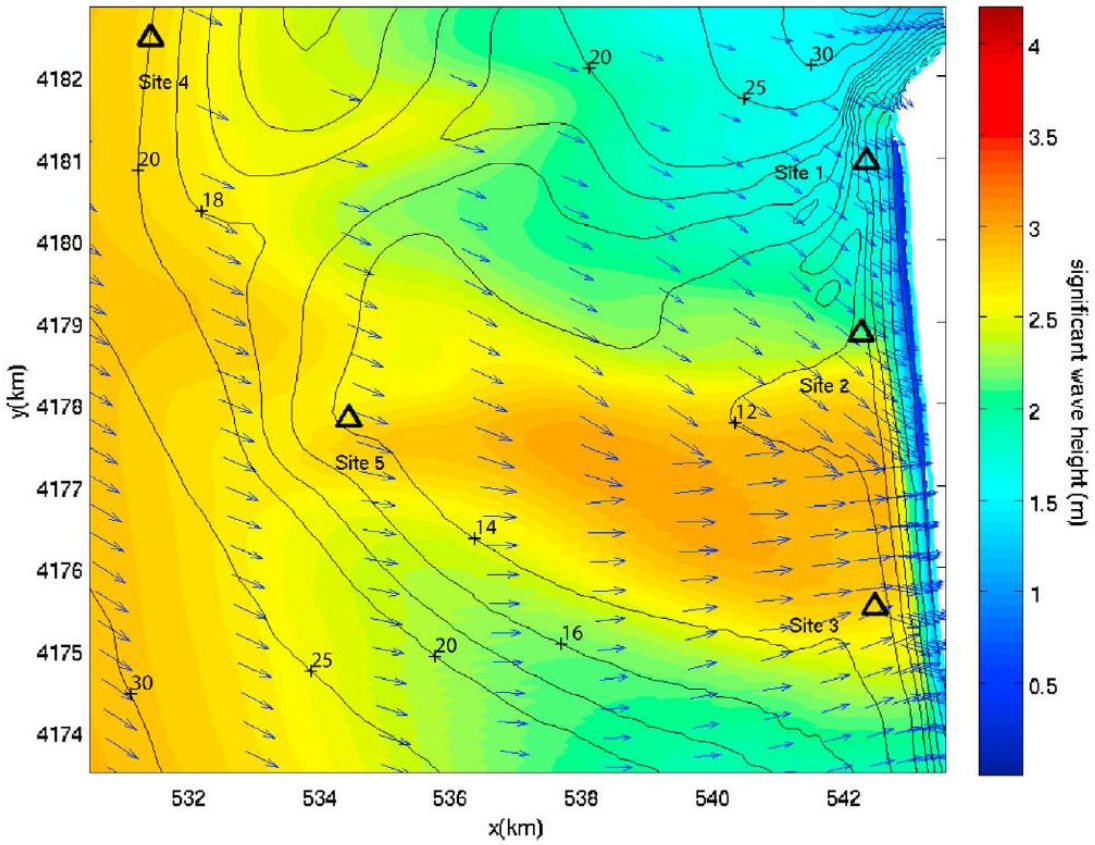

Figure 2.6. Shi et al. (2011) modelled the waves and currents near the ebb tidal delta of San Francisco. Here the arrows indicate the wave propagation direction, the black lines the depth contours (m) and the color scale the significant wave height (m). Waves with an off-shore direction from the north west bend normal to the depth contours in shallow water. For this complex bathymetry, waves focus around the delta on the coast. The wave height increases due to the increase of wave energy at the focus area.

Diffraction

Super-tidal irregularities in bathymetry or shoreline, such as groins or sheltered bays, could create certain wave shadow zones where waves do not propagate. Wave energy leaks toward this shadow zone, in a direction different from wave propagation. This energy leakage is termed wave diffraction. The energy leakage is shown by the decreasing wave height behind the irregular feature.

Possibly, shadow zones for wave diffraction could be located on the back-barrier coast of the barrier islands or behind spits (Figure 2.7). However, wave diffraction will not be one of the dominant wave deformation mechanisms in an ebb delta system.

Figure 2.7. Satellite image (1993) of the Ameland Inlet between the barrier islands Terschelling and Ameland. Possibly, waves diffract behind the spit 'Noorderhaak' of Ameland (Cheung et al., 2007).

Breaking

Wave height decreases abruptly due to wave breaking when waves propagate into shallow water. Waves break when a certain limiting wave steepness or limiting wave height (corresponding to certain water depth) is exceeded. Then the water particle velocity becomes larger than the wave velocity, resulting in breaking.

Waves shoal and steepen on the outer edge of the ebb delta and on the adjacent shorelines (Figure 2.5), followed by wave breaking. During low (high) tide, the zone of wave breaking shifts seaward (shoreward) for both the ebb tidal delta and the shorelines. During storms, when the wave height increases due to the stronger wind, waves shoal earlier, become asymmetric and reach their limiting steepness. So, the breaking zone shifts seaward and moreover intensifies, since more waves reach their limiting steepness.

Wave energy dissipation

Wave energy dissipates (wave height decreases) when waves interact with the sea bed. The rate of wave energy dissipation by bed friction is related to bed shear stress; more energy dissipates during large shear stresses. The wave- and current- related bed shear stress depend on flow velocity and respectively wave and current bed roughness. So, both the rate and the direction of shear stress vary with time and depend on location. Especially the longer waves dissipate energy by bed friction, because they feel the bottom earlier (Figure 2.4).
Generally, most of the wave energy dissipates by breaking and less by bed friction. Due to wave breaking, energy dissipates into vortices (bubbles and foam).
For the ebb tidal delta, most wave energy dissipation can be expected in the breaking zone; the outer edge of the ebb delta and at the adjacent shorelines (Figure 2.5). Furthermore, wave energy dissipates on the shallow part of the ebb delta by bed friction.

Nonlinear wave- wave interactions

In deep water, two pairs of wave components may interfere and lead to a resonance among the four (Figure 2.8). The four wave components are known as a quadruplet (Holthuijsen, 2007). By resonance, energy redistributes over the four wave components, which can be noticed in the energy spectrum (Figure 2.4). In shallow water, resonance can arise already between two wave components, known as triads, resulting in a difference (energy transfer to low frequency, Figure 2.4; Figure 2.8) and a sum component (energy transfer to high frequency, Figure 2.4, Figure 2.8). The sum component propagates in a direction intermediate of the two concerned wave component directions, in contrast to the difference component.

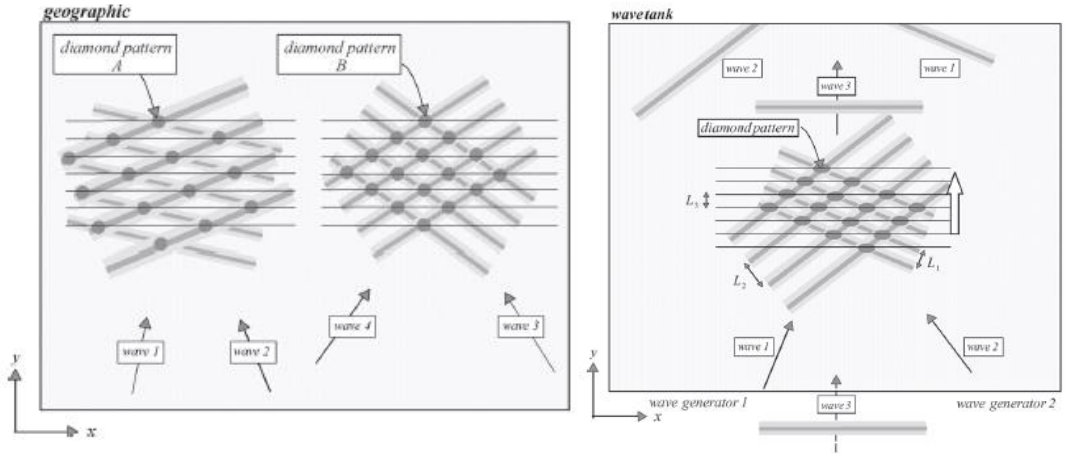

Figure 2.8. In deep water resonance arises between two pairs of wave components, each pair of which can be represented as a diamond pattern (left). By interference, wave energy redistributes over the four wave components. In shallow water, resonance arises already between two wave components (right), resulting in energy transfer to the sum and difference frequency (Holthuijsen, 2007).

2.2.2 Currents

Waves and tide drive currents in the near-shore region. Tide or wave dominance of the tidal inlet determines the shape of the tidal inlet and ebb delta. First the wave- and tide- driven currents will be discussed separately, then is described how waves and tide interact.

Wave- driven currents

Wave-driven currents arise as a result of radiation stresses. Those radiation stresses arise by wave forcing on a fluid volume. A net momentum on the fluid volume accelerates the volume (a current arises), according to the second law of Newton. Where the radiation stresses are a function of the wave energy, those stresses decrease shoreward when wave energy dissipates, especially in the breaking zone. A reduction of the radiation stresses is compensated by a shoreward rise in water level, known as set-up. Radiation stress is composed of cross-shore and alongshore components, because obliquely incident waves force a fluid volume under an angle. The resulting alongshore gradient in (radiation stress and) water level drives an alongshore current. Wave energy dissipation is necessary for a gradient in radiation stresses, so significant alongshore wave driven currents arise only shoreward of the breaker zone and when waves enter oblique. During storm conditions, the wave energy and the energy dissipation increase. Then, the water level gradient steepens and the alongshore current increases. The alongshore current amplifies (weakens) by a similar (opposite) directed wind or tidal forcing.

Bertin et al. (2009) observed in their numerical model wave refraction over the (wave-dominated Óbidos Lagoon (Portugal)) ebb delta and alongshore currents driven by radiation stresses. The net inlet-directed force (refraction) enhances by the net radiation stress directed into the inlet due to the higher set-up of the water level at the ebb delta and the adjacent coastlines than the water level in the inlet (Figure 2.9).

Tide-driven currents

This paragraph starts with a short introduction in tides, followed by a description of the long- and cross-shore tidal component and their interaction along a barrier island coast.

The twelve hour tidal cycle of rising and falling water level can be represented as a long wave with a length of half the earth diameter and a very long period of 12.25 hours. The wave crest passes at high tide and the wave trough passes at low tide. The tidal wave propagation velocity increases with the water depth. In shallow water or at low latitudes the tidal wave propagates slower than the earth rotates. In addition, the continents prevent the tidal wave to propagate through all oceans. Therefore, the tidal wave breaks up in smaller tidal wave

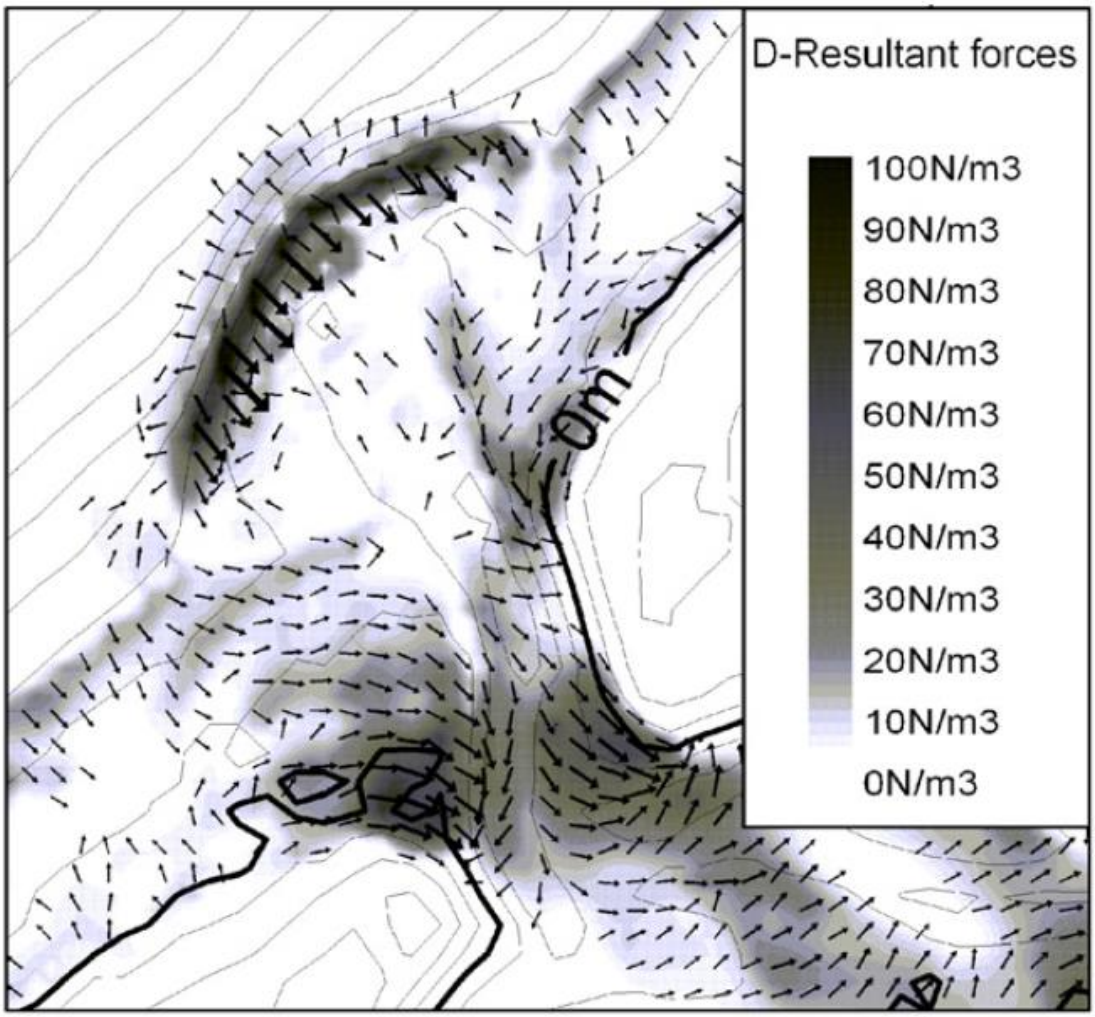

Figure 2.9. Resultant forces in the wave-dominated Óbidos Lagoon in Portugal, from the numerical model by Bertin et al. (2009). The inlet connecting the Óbidos Lagoon with the ocean is about 100m width. Wave refraction over the ebb tidal delta and radiation stresses next to the ebb tidal delta drive the net inlet-directed forces. The radiation stresses arise by the difference in set-up on the outer edge of the ebb tidal delta, the adjacent shorelines and in the inlet.

propagation systems, known as amphidromical systems. The tidal wave in an amphidromical system, also Kelvin wave, propagates in 12.25 hours (anticlockwise in the Northern Hemisphere and clockwise in the Southern Hemisphere) around the amphidromical point where the tidal elevation is zero. The tidal range increases further from the amphidromical point.

When a tidal wave propagates parallel to a barrier island coast, the water level shows a gradient increasing with the tidal range. This gradient in water level drives the longshore tidal current. The alongshore current is in clockwise (or up-drift) direction when the tidal crest just passes until passing of ebb (Figure 2.10, stage 1,4). The alongshore current is reversed (anti-clockwise) (or down-drift) after ebb and until flood (Figure 2.10, stage 2,3).

Where an inlet interrupts the shoreline, during a tidal cycle water flows in and out the tidal basin, which is the cross-shore tidal current. During flood the water spreads radially into the basin, whereas the outflow or ebb jet is strong confined in the ebb channel.

Sha and Van den Berg (1993) found the tidal cross- and alongshore currents in an inlet show a flow pattern of two or four distinct stages during the tidal cycle (Figure 2.10). Stage 1 and 3 only arise when the tidal range is large, driven by large water level gradients. Then, the maximum velocity of the alongshore current coincides with the highest or lowest water level in the basin. So, the water level fluctuates in and out the basin with a phase difference of a quarter of the tidal wave period (3 hours). Stage 2 and 4 arise when the alongshore tidal current increases and the water level in the basin is already increasing or decreasing respectively. In case of a smaller tidal range, the current pattern will only show stage 2 and 4. Then, the high and low tide in the basin correspond to a zero alongshore current (slack). So, the water level fluctuates at sea and in the basin similarly. Stage 2 and 4 show the maximum alongshore current and cross-shore when the basin water level is at mid-tide (Sha 1989a,b).

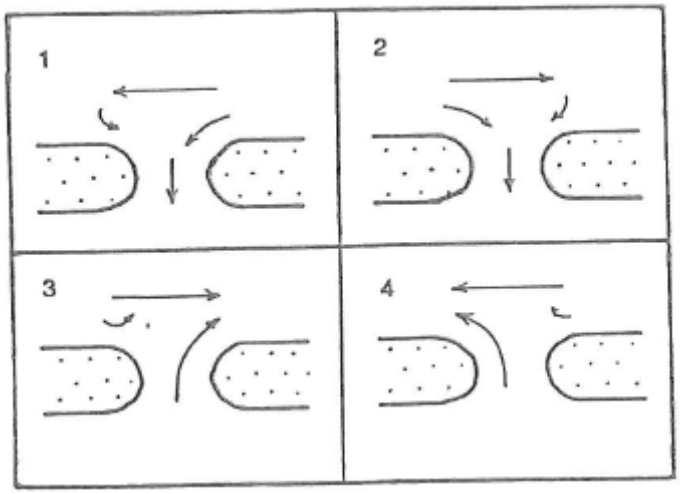

Figure 2.10. Sha and Van den Berg (1993) showed the interaction of the alongshore and cross-shore tidal flow nearby an inlet. Tidal inlets located in an area with a large tidal range show four stages of cross- and alongshore current interaction. When the tidal range is smaller, the alongshore water level gradient decreases and the maximum alongshore and cross-shore ebb (flood) tidal current are at the same moment (stage 4 and 2).

Sha (1989a) studied the sediment transport in the tidal inlet of barrier island Texel, The Netherlands. Therefore, he studied the currents over the ebb delta and in the inlet. He found the interaction of longshore and cross-shore tidal currents drive rotational circulations, varying during the tidal cycle (Sha, 1989a,b). The cross-shore and longshore current appeared to enhance each other at the up-drift site (clockwise direction) of the Texel inlet (Figure 2.11). During ebb the longshore water level gradient is downward to the up-drift side of the inlet. So, most of the ebb jet will flow toward the up-drift side, enhancing the offshore current

around the up-drift barrier head. The part of the ebb jet flowing toward the down-drift side of the inlet, will be opposed by the down-drift flowing alongshore tide driven current, possibly inducing rotational currents (Figure 2.11). During flood, the alongshore water level gradient is downward down-drift. The inflow through the inlet is enhanced around the up-drift barrier island head again. However, behind the ebb delta the flow will rotate, because the alongshore flow reverses to enter the tidal inlet (Figure 2.11). The multi-directional currents due to the circulations down-drift of the inlet were measured in the Texel inlet (Sha, 1989a). The current vector was simply two directional at the up-drift side (Sha, 1989a). The tidal prism and inlet size determines the significance of the cross-shore current on the alongshore current (Sha, 1989a). So, the stronger currents are dominantly up-drift located in tidal inlets (Figure 2.10, stage 2 and 4), inducing a preferable down-drift bending of the ebb channel (Sha and Van den Berg, 1993). Tidal inlets with large tidal ranges are an exception on this, where the currents bending around the inlet are alternating down-drift and up-drift (Figure 2.10, stage 1 to 4).

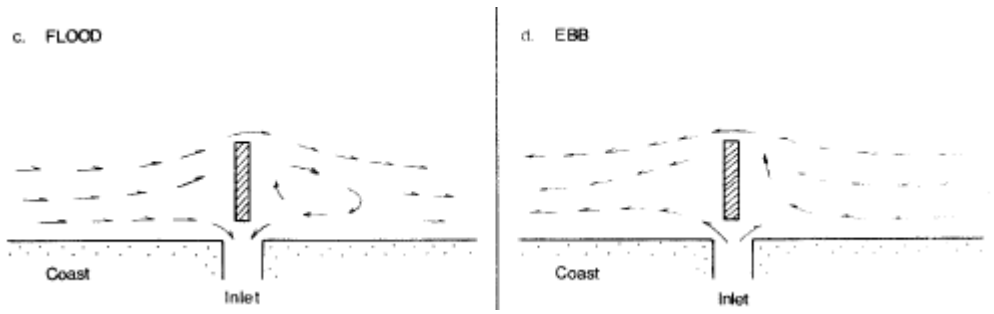

Figure 2.11. Rotational currents arise down-drift (anti-clockwise) of the ebb tidal delta by the interaction of the alongshore and cross-shore tide driven currents. Especially, around the up-drift barrier head the current strengthens (Sha, 1989b).

Interaction waves and tide

Sha (1989b) and Oertel (1977) mentioned the ebb delta configuration depends on dominance of wave or tidal processes along the barrier island coast. Sha (1989b) found in the German Bight, tide dominance increases by an increase in tidal range or tidal prism or a decrease in wave forcing. A tide- dominated tidal inlet (with small tidal range (Sha and Van den Berg, 1993) has strong currents around the (clockwise) up-drift barrier head (Sha, 1989b). Oertel (1977) developed a model, with tide- dominated ebb deltas further protruding into the sea than wave- dominated deltas. Large waves will counteract the cross-shore tidal in- and outflow and strengthen the alongshore current. So, wave- dominated ebb deltas protrude less far into the sea. Sha and Van den Berg (1993) combined the effects of (oblique incident) waves and tide in a descriptive model of ebb delta shape (Figure 2.12). Stage A to C represent a preferable up-drift located ebb channel, changing to down-drift when the effect of wave

forcing dominates the effects of the tidal currents. Stage D to F hold for the tidal inlets with large tidal ranges (Figure 2.10; with stages 1 to 4), which have a less asymmetric ebb channel shape and direction. The ebb channel shifts from up-drift to down-drift by an oblique wave forcing (Figure 2.12).

In addition to the effect of waves on currents and the ebb tidal delta configuration, the currents affect the waves. Especially in coastal zones with a complex bathymetry currents interact with waves, where currents are not perpendicular directed on the wave propagation direction.

According to the dispersion relation (equation 2), wave height increases or decreases when a current respectively opposes (ebb) or follows (flood) the waves. Moreover, wavelength decreases in presence of an opposing current. The wind speed may affect wave period in presence of a current counteractively, known as wave age effect. Waves grow more (increased wave height and period) (less, decreased wave height and period) since the wind speed is higher (lower) relative to the sea surface due to an opposed (following) current. The net effect of currents on waves depends on the dominant wave-current interaction mechanism; dispersion relation or the wave age effect.

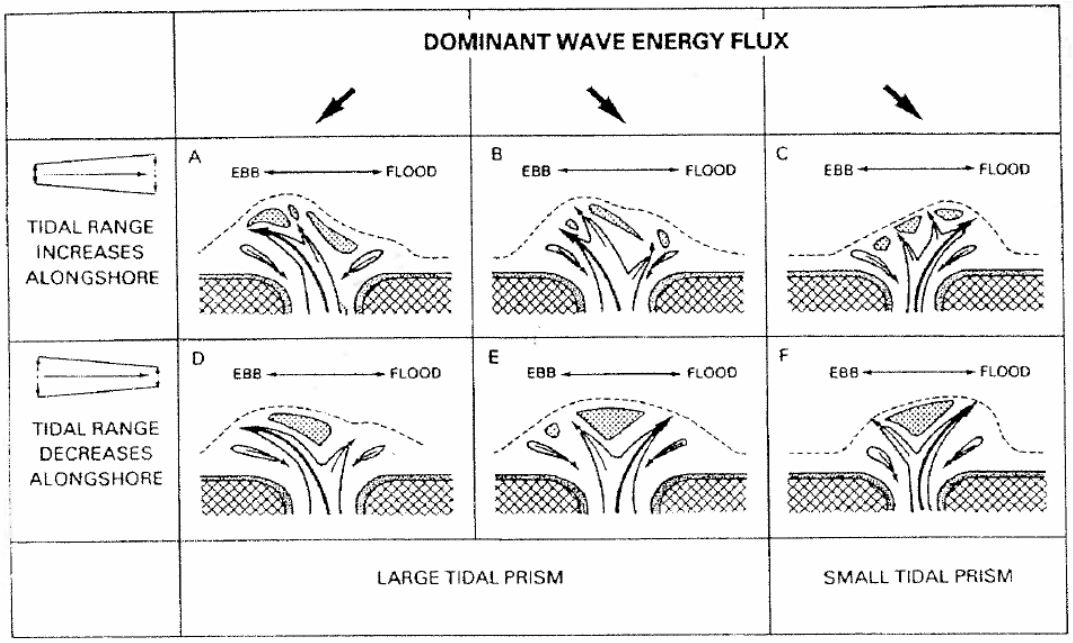

Figure2.12. The ebb delta configuration depends on the dominance and direction of waves and tide along a barrier coast (Sha and Van den Berg, 1993).

2.3 Marine X-band radar

Generally, current or wave data are collected by in-situ instruments. Over a larger area, spatially covered data of currents or waves can be collected using remote sensing devices. Examples of existing radar systems are the Dutch Shipping Radar (SHIRA) and the German Wave Monitoring System (WaMoS).

In Section 2.3.1 is described how the radar collects data, starting with a description of a typical marine radar system, followed by the imaging mechanism and corresponding limitations in measuring. Hydrodynamic parameters can be extracted (Section 2.3.2) from image spectra after filtering. Finally, this section concludes with the accuracy and validation (Section 2.3.3) of the radar inferred data.

2.3.1 Data collection

2.3.1.1 Radar system

Radar, or RAdio Detection And Ranging, is a remote sensing technique using microwaves (similar to radio waves). The technique is based on time and frequency (Doppler) differences between an emitted microwave and the returned microwave. An emitter sends a microwave pulse, the surrounding objects backscatter the pulse partially. The intensity of the reflected microwave pulse depends on the surface type, especially rough surfaces have a high reflectance (Section 2.3.1.2). The receiver measures the return time and the intensity of the reflection. The type of emitting microwave signal ranges from a wavelength between 1mm and 1m (Lillesand et al., 2008). Marine radars used for sea surface monitoring have a frequency in the X-band frequency field, with a wavelength between 2.4 and 3.75cm (Lillesand et al. 2008). The plane in which the emitter emits a sinuous microwave pulse differs with respect to the propagation direction (from end members horizontal and vertical), known as polarization. Generally, the emitter and receiver only measure the microwave signal for horizontal or vertical polarization. Hoekstra and Van der Vlugt (2000) compared polarisation orientation and concluded an improved sea surface image with less noise arises by vertical polarisation for both the emitter and the receiver (to measure wave period at the shore of Petten, The Netherlands). Valenzuela (1978) mentioned the radar return intensifies for vertical polarisation, due to backscatter characteristics found by Wright et al. (1966, in Valenzuela, 1978).

Generally, the antenna of a marine radar monitors a circular plane by rotating the antenna around a vertical axis and sending pulses (Figure 2.13). The marine radar sends a pulse over a certain beam width in a certain direction. After the returned backscatter signal is received, the radar antenna rotates and sends a pulse in a direction slightly deviating from the previous. Together those pulses cover a circular plane during one rotation. The variation in backscatter

intensity results in a singular image of sea clutter after one rotation (Figure 2.14). The antenna emits pulses under an angle with the horizontal plane, known as range. The azimuth is the horizontal direction in which the emitter emits the signal. The temporal resolution of marine radar equals the rotation time of the radar antenna of 2-3s, though ship radars have even a larger temporal resolution. The spatial range resolution (Figure 2.15) depends on the pulse length T (Range resolution=0.5Tc, c speed of light (Mattie and Harris, 1979 in Young et al., 1985)). The spatial azimuth resolution L depends on the range and the (azimuth) beam width $\Delta\theta$ (in radian) of the radar as $L=R\ \Delta\theta$, with range R (Young et al., 1985).

Figure 2.13. The marine radar sea surface monitoring system WAMOS II (left) (Hessner and Reichert, 2007) and SHIRA (right) (Hoekstra and Van der Vlugt, 1999).

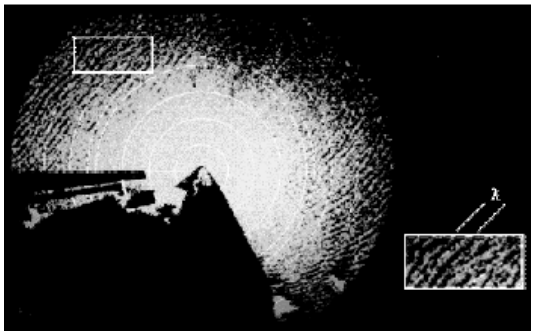

Figure 2.14. The WaMoS measured the sea clutter above after one rotation (Nieto Borge and Soares, 2000).

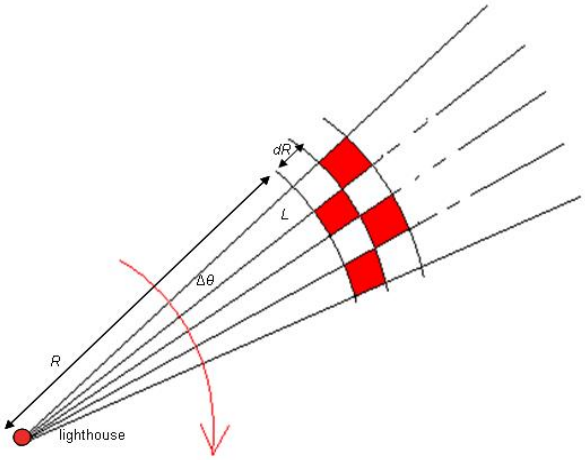

Figure 2.15. The spatial range and azimuth resolution of a circular radar image (Peters, 2010).

2.3.1.2 Radar imaging of the sea surface

The sea surface is monitored by measuring the intensity and return time of the backscattered microwave signal. When the microwave pulse is emitted, the pulse is backscattered after hitting a surface or object (Figure 2.16). Valenzuela (1978) studied the backscattered signal, however the radar return from the sea surface is still not fully understood (Valenzuela, 1978;Young et al., 1985). In addition to an increase of backscatter at rough surfaces, at oceans the return signal increases also by interaction of the microwaves with the sea surface (Figure 2.16). Basically, the microwave backscatters on the ripples and foam (sea clutter) (Figure 2.16) arising by local wind (Nieto Borge et al., 1999; Nieto Borge and Soares, 2000). Sea clutter increases with the wind velocity.

Young et al. (1985) mentioned resonant- Bragg scatter and specular scatter as the dominant scatter mechanisms in (microwave) radar imaging. Specular scatter is the 'normal' reflectance and present at very small (range) distance from the radar where the incidence angle (between radar pulse and the sea surface) is low (<20deg (Chowdhury, 2007; Young et al., 1985)). However, specular scatter is not significant for land-based marine radars, because at the nearest shoreline the sea surface scatters Bragg-resonance already, at such incidence angles. Interaction of small wavy patterns (foam and (wind) ripples) with wavelengths half (~1.5cm) (by Bragg-scatter criterion, Valenzuela, 1978) of the radar wave length (~3cm (X-band)) induces Bragg- resonance. The radar monitors those Bragg waves, which are located on top of the larger ocean waves.

The wave parameters of the larger ocean waves follow indirectly by studying the variations in Bragg backscatter signal of the small capillary waves. The spatial pattern of the small ripples and foam deform or modulate by the larger ocean waves (Hasselman et al., 1978; Valenzuela, 1978; Young et al., 1985; Nieto Borge et al., 1999). So, to find the wave characteristics of the

ocean waves, the modulation mechanisms of the small capillary waves by the large ocean waves should be known. Valenzuela (1978), Hessner and Reichert (2007) and Nieto Borge et al. (2000) mention the backscatter signal deforms by hydrodynamical and orbital modulation and at large (grazing) incidence angles by shadowing of small waves by larger waves or by the difference in local incidence angle at the wave surface, known as tilt (Figure 2.16). Furthermore, Nieto Borge and Soares (2000) mention the imaging of the backscatter signal depends on the range, the azimuth and the wind speed. The backscatter intensity decreases when the range increases. The backscatter intensity increases in the wind (or wave propagation) direction. The backscatter intensity increases at larger wind velocities. Generally, the small capillary waves are hydrodynamical modulated so the ripples are located on the (ocean) wave crests.

The backscatter signal is generated differently in the breaking zone, which is significant at the ebb delta. In the breaking zone, the radar backscatter mechanism changes from Bragg scatter to backscatter due to so-called sea spikes (Ruessink et al., 2002). The wave breaking induced backscatter is composed of both specular and non-specular scatter and has a substantial higher intensity.

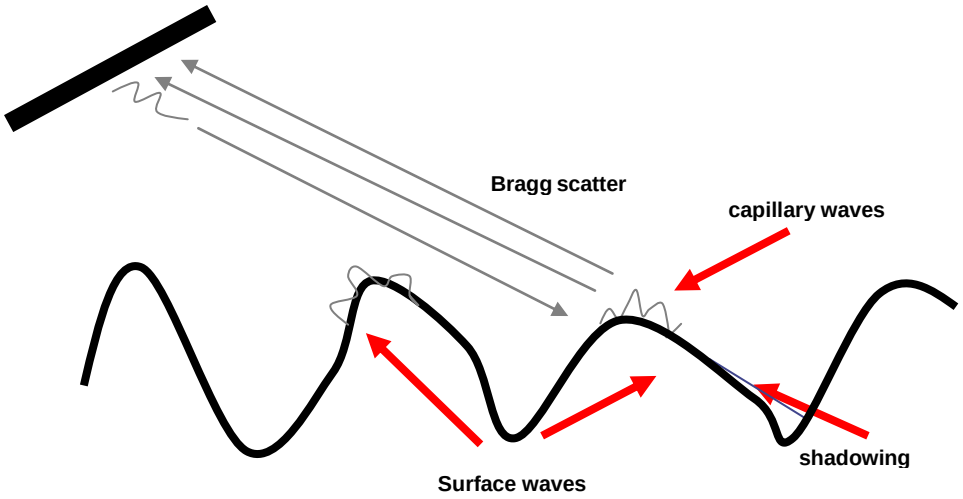

Figure 2.16. The marine radar emits pulses at 9.6GHz and receives the Bragg backscatter of the radar signal on the capillary waves on top of the ocean waves (Van Heesen and Kleijweg, 2010)

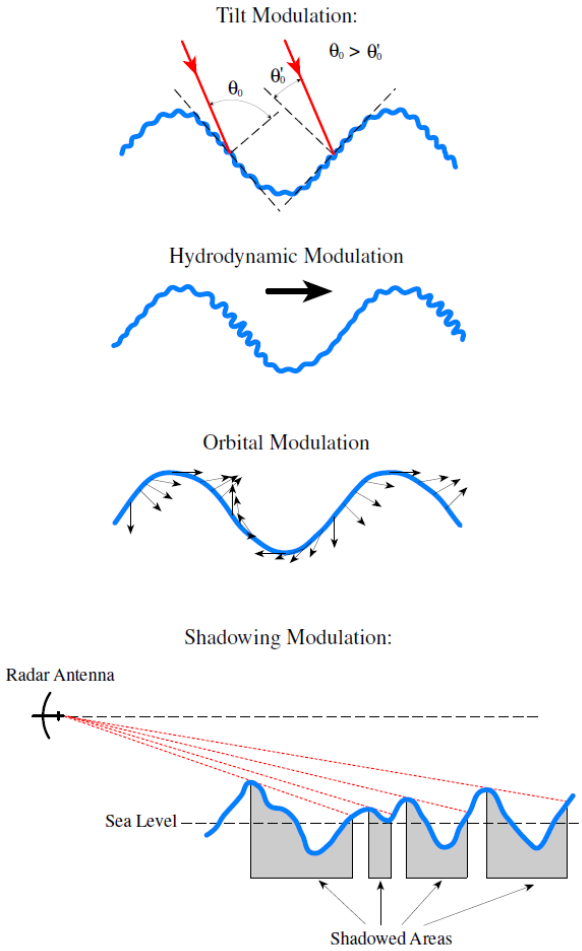

Figure 2.16. Radar imaged small ripples and foam on the sea surface are modulated by the four effects mentioned above; tilt, hydrodynamic, orbital and shadowing modulation (Nieto Borge, 2002). Those ripple modulation induces (Bragg) backscatter variations (in times and space) which represent the foam pattern and indirectly the ocean wave pattern. The radar return signal increases when the slope of the ocean wave tend to be normal on the incident radar microwave, known as tilt. Due to the hydrodynamic and orbital motion of the ocean waves, the ripples accumulate on the ocean wave crest. Large waves shadow small waves at large range from the radar.

2.3.1.3 Limitations

Each measurement technique has limitations, and so the marine X-band radar has. However, one of the advantages of radar above different remote sensing techniques is the monitoring with high frequency, whereby the temporal evolution of the sea can be observed. Radar measures also during the night or with light rain, clouds or haze (Lillesand et al., 2008). Wyatt et al. (2003) showed the WaMoS radar does not image well during heavy rain.

The hydrodynamic parameters wave length, wave direction, current speed and current direction and water depth can be extracted from the images. Unfortunately, wave height still

cannot be computed, as the image intensity in the image spectra is a measure for the backscatter of the sea surface instead of an energy level. Wave height can be estimated when the radar image spectra are converted to wave spectra by a Modulation Transfer Function (MTF) (Nieto Borge et al., 2004).

From the previous section; the sea surface image quality depends on distance from the radar, wind velocity (Nieto Borge et al., 1999; Nieto Borge and Soares, 2000) and wave propagation direction (Nieto Borge et al., 2000). When the distance from the radar increases, the return intensity decreases, shadowing (Section 2.3.1.2) increases and the incidence angle increases (tilt modulation). Radar return intensity is highest where the wave propagation direction is opposite to the radar view direction. Nieto Borge and Soares (2000) mention the specific wind speed lower and upper limit depend on the radar (antenna length and microwave intensity) and the angle of incidence. Generally, for sea surface imaging the wind speed has to be between a minimum of 3m/s (Reichert et al., 1998 in Bell 1999, also shown in Wyatt et al., 2003) and a maximum of 20m/s (Alkyon 2006). Sea clutter can no longer be monitored when the wind speed decreases below the minimum, since the sea surface imaging mechanism is based on the ripple pattern arising by local wind. During strong winds wave breaking over a too wide range distorts the image, whereby sea clutter cannot be distinguished anymore (Alkyon 2006, Wyatt et al., 2003; Swinkels, 2011). The wind speed limits can be related to limits in significant wave heights (Wyatt et al., 2003).

The sea surface can be distinguished within a range of 4.5km for the SHIRA (Hoekstra and Van de Vlugt, 1999) through 5.5km for WaMoS (Hessner and Reichert, 2007) to 7.5km for the SeaDarQ radar at Ameland (Swinkels, 2011; Gautier and Westhuysen, 2010) using an X-band marine radar. The temporal and spatial resolution depends on the technical adjustments of the radar. The radar rotates in 1.6-1.7s (SHIRA, Hoekstra and Van der Vlugt), 1.9s (WaMoS, Nieto Borge et al., 1999) and 2.85s (Ameland radar, Swinkels, 2011), which represents the radar temporal resolution. However, waves shorter than two times the sample (rotation) time might be underestimated by aliasing. The spatial resolution prescribes a minimum measurable wavelength at two times the cell size. The maximum wavelength equals the size of the computational cell, over which the wave characteristics are computed. The SHIRA radar (Hoekstra and Van der Vlugt, 1999) with a cell size of 3.75m and 128x128 pixels has a minimum wavelength of 7.5m (Hoekstra and Van der Vlugt, 1999), the corresponding maximum wavelength is 480m. The radar at Ameland (Swinkels, 2011; Gautier and Westhuysen, 2010) with a resolution of 7.5m and computational cells of 960m (128x128 pixels) can measure wavelengths between 15m and 960m.

2.3.2 Image processing

Generally, the methods developed to estimate wave parameters from sea clutter assume a stationary and rather homogenous wave field (Young et al., 1985; Nieto Borge et al., 1999, 2004; Nieto Borge and Soares, 2000). Senet et al. (2008) developed a new method, which can be used to compute the wave characteristics of individual waves. This method, known as Dispersive Surface Classificator (DISC) assumes a stationary but inhomogeneous wave field. Here, the most commonly applied method (SeaDarQ, SHIRA, WaMoS) will be explained, assuming stationarity and homogeneity of the waves within their computational cubes.
The radar sea clutter images, subdivided in time sequences of sub images are known as computational cubes (Section 2.3.2.1). The goniometric output of a Fourier Transform on the wavy patterns in the computational cube is filtered using the dispersion relation (Section 2.3.2.2). Then, current magnitude and direction, image spectra, wave characteristics and water depth can be computed (Section 2.3.2.3). Wave height can be estimated from converted (MTF) image spectra.

2.3.2.1 Image spectra

When continually rotating, a time sequence arises of sea clutter images in polar coordinates (azimuth and range). The image sequence in each direction is split into several (radial) computational cells with sides of a few hundred pixels. The computational cubes include a sequence of sea clutter images of consecutive time steps and can be represented by the Cartesian coordinates *x, y* and *t*, after conversion of the polar coordinates (by nearest neighbourhood interpolation) (Senet et al., 2008, Alkyon, 2006) (Figure 2.18).
The in gray-scale represented alternating high and low intensity backscatter in the image sequence shows a complex wave pattern. Wavelengths and frequency of the waves in this

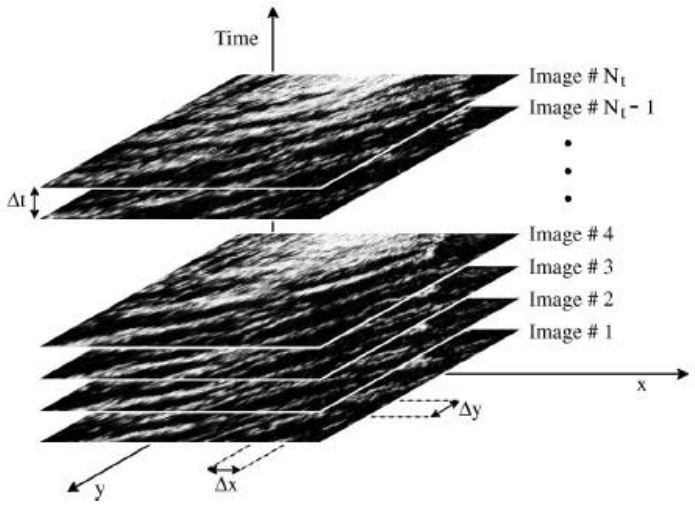

Figure 2.18. A time sequence of radar images arises after continually rotating of the radar. The circular images are split into several computational cubes and converted to Cartesian coordinates (x,y,t) (Nieto Borge et al., 2004).

image sequence can be extracted by a 3D Fourier transform (Young et al., 1985). The wave pattern $F(x,y,t)$ in the image can be represented as a superposition of several sine functions (j=0..N-1)

$$F(x,y,t) = \sum_{j=0}^{N-1} \eta(\xi_j) \sin\left(k_x x + k_y y - \omega t\right) \tag{4}$$

with wave number vector $\vec{k}$ (composed of a wave number in the x- and y-direction, respectively k_x and k_y) and frequency ω. Each sine j has an amplitude η, which depend on time and location $\xi(x,y,t)$ and represents the gray-scale of the image. Young et al. (1985) executed a 3D Fourier transform over the computational cubes. From this Fourier transform wavelengths k_x and k_y in respectively the x- and y- direction arise and corresponding frequency ω arises for the (computational) image. This set of wave numbers and frequency can be referred as unfiltered, uncorrected (including current) 3D image or variance (of backscatter intensity) spectrum $I(k_x,k_y,\omega)$.

2.3.2.2 Filtering of 3D image spectrum

The set of wave numbers and corresponding frequency can be plotted in 3D (Figure 2.19), with at the x- and y- axis the wave numbers in corresponding direction and at the z-axis the frequency. The 3D image spectrum should fit to the dispersion relation (eq. 2) exactly (Figure 2.19). However, the radar data deviate from the dispersion relation by distortions as radar reflections by ships or buoys (Alkyon, 2006) or by sea surface modulations due to radar imaging. Besides, a current in the wave field will shift the dispersion relation over the horizontal wave number plane. When waves interact with the bottom the dispersion relation may deform in the vertical (frequency) plane. So, first current and depth are estimated, for example by using a least-squares method (Hessner and Reichert, 2007). Then the resulting dispersion relation, including a current, is used as filter (Young et al., 1985; Nieto Borge et al., 2004) for the 3D image spectrum $I(k_x,k_y,\omega)$ to exclude the noise (buoys etc). Subsequently, the 3D spectrum is integrated to a 2D wavenumber spectrum to determine wave number and direction, after which frequency follows by interpolation on the 3D dispersion shell. Then the spectra are ready to use and wave characteristics can be derived (Section 2.3.2.3).

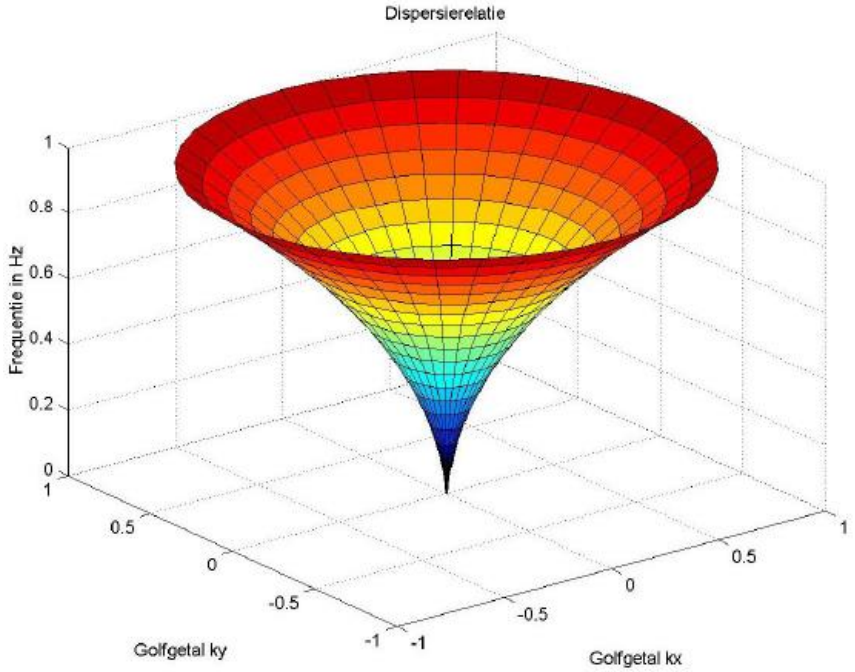

Figure 2.19. The set of wave numbers and frequencies are related to each other by the dispersion relation (ideally), with at the *x*- and *y*- axis the wave numbers in corresponding direction and at the z-axis the frequency ω. The presence of a current shifts the funnel-shape in the 3D domain (Hoekstra and Van der Vlugt, 2000).

2.3.2.3 Radar inferred characteristics

Currents

Current appears (from the previous section) as a residual of the radar image spectrum processing, since it is estimated as the shift in the wavenumber plane of the 3D image spectrum and it is removed to obtain a 'clear' image spectrum to derive wave field characteristics.

Bathymetry

Three methods are described how water depth can be extracted from radar images.

First, the radar processing company SeaDarQ mentioned water depth in shallow water to be a residual of the image spectra processing. As in shallow water the long waves deform by the bottom. So a non-linear fit on the low frequent part of the image spectrum may result in a water depth.

Second, Bell (1999) quantified the bathymetry in the near-shore zone from wave celerity and wave period using linear wave theory. He determined the wave celerity from wave movement in consecutive radar images using cross-correlation. The highest correlation coefficient between a certain (group of) pixel(s) and neighbours in the next image shows the wave

motion for this (group of) pixel(s). As above shows, the wave celerity analysis can be applied on both single and groups of pixels. The peak wave period can be computed from the frequency spectrum as abovementioned. In a bimodal wave field the peak of the longest period (swell) waves is used. Then the water depth follows from linear wave theory as (equation 1 in Bell, 1999)

$$h=\frac{L_0}{2\pi}\frac{c}{c_0}\tanh^{-1}\frac{c}{c_0} \tag{5}$$

with water depth h, (deep water) wave celerity (c_0) c and deep water wavelength L_0 as

$$L_0=\frac{gT^2}{2\pi}=c_0T \tag{6}$$

Bell (1999) neglects interaction of currents with waves, by the assumption of negligible currents in the near-shore zone because waves refracted already.
Third, Alkyon (2006) mentions a qualitative approach to estimate bathymetry and how it evolves over time by using time averages of single radar images. The time averages show the dominant waves and currents, since those deform by interaction with the bottom. Thus actually changes in water depth can be observed, because waves and currents change and deform on the bathymetry. This qualitative technique to deduce the bathymetry can be compared to optic remote sensing, such as video imaging (see also Ruessink et al.,2002).

Wave length, wave angle and wave period
Young et al. (1985) converted the 3D image spectrum to 2D and 1D spectra. First, the *x*-and *y*-component of the wave number can be combined in one vector, then the 3D image spectrum changes into (equation 22 in Young et al., 1985)

$$E(k,\ \theta,\ \omega)=E(k_x,k_y,\omega)\ |\vec{k}| \tag{7}$$

here $\vec{k}$ represents the wave number vector composed of an x- and y- component, under wave angle θ. Equation (6) integrated to the angular frequency and the wave angle

$$\mathrm{E}(\vec{k})=2\int_0^{\infty}\int_0^{2\pi}E(\vec{k},\ \theta,\ \omega)\mathrm{d}\theta\mathrm{d}\omega \tag{8}$$

results in a wave number spectrum, where the peak wavelength can be computed from. Young et al. (1985) obtained the frequency-directional spectra by

$$\mathrm{E}(f,\theta)=|\vec{k}|\frac{\mathrm{d}|\vec{k}|}{\mathrm{d}f}\int_0^{\infty}\mathrm{E}(k_x,k_y,\omega)\mathrm{d}\omega \qquad (9)$$

with the component in front of the integral as Jacobian. From the frequency-directional spectrum the wave angle corresponding to the peak frequency can be determined.
The peak frequency can be extracted from a frequency spectrum, integrating equation (8) over the directional field, following

$$\mathrm{E}(f)=\int_0^{2\pi}E(f,\theta)\mathrm{d}\theta \qquad (10)$$

Sea surface elevations from wave spectra

Wave height can be derived from sea surface elevations. The sea surface patterns monitored by the radar are approached by a Fourier Transform on the radar image (Section 2.3.2.1). The wave pattern in the computational cells can be decomposed in different sine functions with wave length, frequency and a certain amplitude. The superposition of the amplitudes should represent the sea surface elevations, wherefrom a statistical measure of the wave height can be derived. Unfortunately, the radar image inferred amplitudes represent just gray-scale intensity of the radar image instead of a real wave height. To derive real wave height factor a correction factor or function is needed.
Young et al. (1985) considered calibration of a normalized image spectrum of a computational cube with a normalized wave (from field data or numerical model (Nieto et al., 2004)) spectrum. Then, the ratio of the radar image spectrum and the in-situ wave spectrum represents a (Modulation) Transfer Function (Figure 2.20). Nieto et al (2004) determined the MTF theoretically and from field data. They show (the theoretical approach) the MTF compensates particularly for shadowing mechanisms at small radar view angles, earlier found in the determination of significant wave height by Wenzel (1990, in Nieto Borge et al., 2004). The not-normalized image spectrum multiplied by the MTF results in a wave energy spectrum, wherefrom significant wave height can be derived. In Nieto Borge et al. (2004) wave height derived by use of the MTF in an inversion scheme is explained more thoroughly. In Hessner and Reichert (2007) the inversion scheme method of Nieto et al. (2004) was used in combination with a Directional individual Wave Finding Algorithm (Reichert, 2006 in Hessner and Reichert, 2007) to estimate significant and maximum wave (or crest) height.

A different technique to estimate wave height, originally applied on spaceborne Synthetic Aperture Radar images (Alpers and Hasselman, 1982, in Nieto Borge et al., 1999, 2004) holds linearly relating the signal-to –noise ratio root to significant wave height (Figure 2.21) using wave buoy wave height as calibration (Nieto Borge et al., 1999).

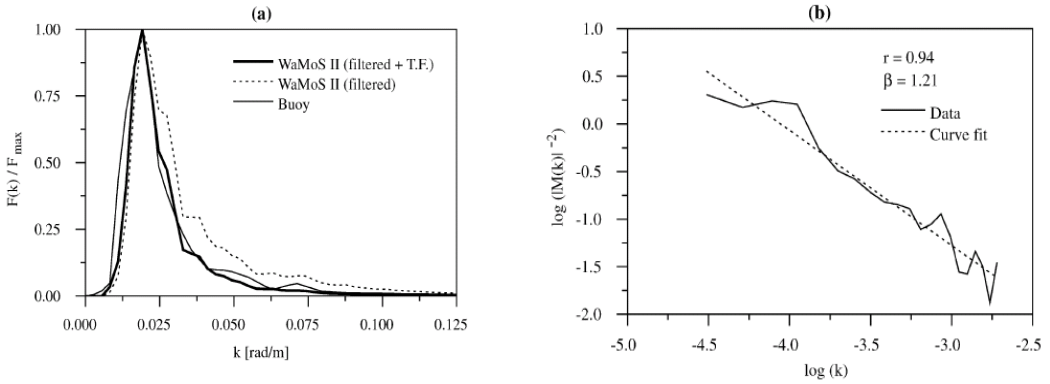

Figure 2.20 (Nieto Borge et al., 2004). Normalized buoy and radar 1D wavenumber spectra correspond clearly (a), an empirical based Modulation Transfer Function arises as the ratio of radar and buoy spectrum (b). The trend through the MTF in the log-log plot suggests the MTF is related to wavenumber as MTF~$k^{-1.2}$.

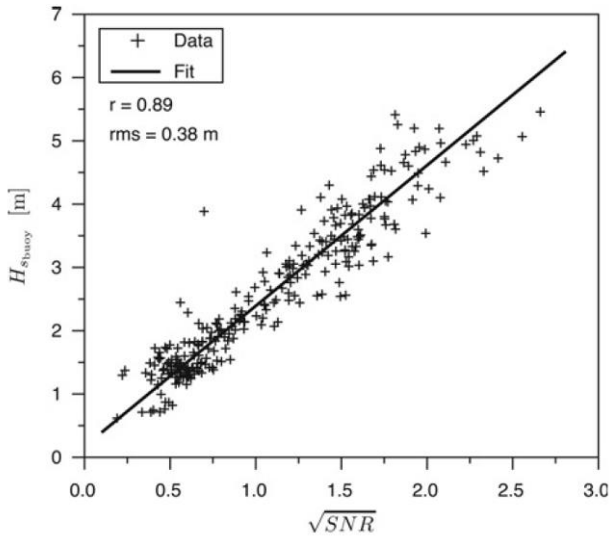

Figure 2.21 (Nieto Borge et al., 2008). Significant (buoy) wave height is related linearly to the root of the signal-to-noise ratio.

2.3.3 Accuracy

Accuracy of the imaging of the sea surface depends on data collection and data processing. The accuracy of data collection was discussed in Section 2.3.1.3 above. Here, the accuracy of the data processing is studied. First, the SeaDarQ radar data processing method is discussed, followed by the accuracy of the extracted hydrodynamic parameters. The latter is discussed by validation with field (Shemdin et al., 1978) or model data (Wyatt et al., 2003; Swinkels, 2011; Gautier and Westhuysen, 2010) of the different hydrodynamic parameters.

The 3D Fourier transform was performed on computational cells with sides of a few hundred pixels. So, this image processing technique assumes stationary and spatial homogenous wave field, current and water depth in the computational cell. However, a wave field is not homogenous in the near-shore by the significant effects of bathymetric variations on waves. Locally more accurate hydrodynamic parameters arise when the size of computational cells are reduced, however an accompanying effect is reduction of the resolution. Senet et al. (2008) found a method (Dispersive Surface Classificator) to obtain wave characteristics of individual waves, resulting in more accurate wave characteristics (with contrastingly an increase in the spatial resolution). Their method allows non-homogeneity of the wave field, because sea state is individually determined. Only small spatial variations in wave length, water depth and current are required, because linear wave theory is used (Senet et al., 2008). To illustrate the limits of the image processing based on large computational cubes, Swinkels (2011) found a not highly accurate radar inferred water depth in highly variable areas (for example nearby channels), because the derived water depth shows an average of the computational cell. Moreover, image spectra quality reduces since the dispersion shell is more difficult to fit on the imaged data due to the high bottom variability.

A current (exactly) perpendicular to the wave propagation direction cannot be measured, because the relation between wave number and frequency is not shifted (Hoekstra and Van der Vlugt, 1999).
Swinkels (2011) found current (and water depth) cannot be estimated during very low energetic conditions, because neither dispersion shells fit through the 3D set of wave numbers and frequency nor a non-linear fit can be found to extract current and water depth. In contrast, wave number and frequency is independent of the energetic conditions (except the requirement of sea clutter) and can be computed, though the image spectra quality reduces when current or depth is not extracted.
Bell (1999), Flampouris et al. (2008) and Swinkels (2011) mention that water depth is overestimated in shallow water, because of the influence of non-linear effects on the waves. The applied linear wave theory to estimate water depth overestimates the wave celerity in the near-shore. Hoekstra and Van der Vlugt (1999) found underestimations in deep water, because in deep water the waves are not affected by the bottom (too deep water or too low energy of low frequency waves). Grilli (1998 in Bell, 1999) obtained more accurate bathymetric estimates by using higher-order wave theory instead of the linear wave theory. The higher-order wave theory attempts to include the non-linear wave behaviour in the estimation of the wave celerity for the bathymetry. However, in higher-order wave theory, too, estimates are required for wave height and wave asymmetry.

Wyatt et al. (2003) compared field, model (WAM) and radar (WaMoS) measurements during the EuroROSE campaign in a swell-dominated wave field in Spain and a storm-dominated wave field in Norway. Wyatt et al. (2003) found wave energy is underestimated for short period waves (f>0.15-0.2Hz).
Nieto Borge and Soares (2000) related wave buoy data to radar data. However, they need to use an interpolation method to extract the directional spectrum from the wave buoy, wherein the present bimodal wave field (wind sea and swell) was lost. In contrast, the radar shows the bimodal wave field and thus performs better.

2.4 Ameland Inlet

This thesis focuses on wave characteristics monitored by the radar on the lighthouse of Ameland, monitoring the Ameland Inlet and ebb tidal delta. The first paragraph describes the wave and tidal climate at the Ameland Inlet, followed by findings from earlier studies (Gautier and Westhuysen, 2010; Swinkels, 2011) on radar images compared to numerical model results of this study site.

Figure 2.22 shows the morphological units of the Ameland Inlet, located between the barrier islands Terschelling and Ameland. The inlet system shows asymmetry with a westward (up-drift) directed main channel and an eastward located tidal basin with respect to the tidal inlet. The inlet, known as Borndiep (Figure 2.22), with a width of 4km (Dissanayake et al., 2009) and a maximum depth of 28m (Sha, 1989b) connects the North Sea with the Wadden Sea. The Borndiep changes into the ebb-dominated Akkepollegat and ends onto a shoal. The shoal is part of the asymmetric ebb tidal delta protruding 6.0km into sea (Sha, 1989b). The Bornrif, connected to the northwest edge of Ameland belongs also to the ebb tidal delta. Along the head of Terschelling the up-drift directed (ebb –dominated) Westgat is connected to the narrow Boschgat into the basin.
The semidiurnal tide is propagating alongshore with a speed of 15m/s (Dissanayake et al., 2009), from west to east. The mean tidal range is 2.0m (Sha, 1989b). The waves enter from the northwest dominantly and have a significant wave height of approximately 1.1m, during storms offshore wave heights can reach 7-8m. The eastward littoral drift is estimated as 1.0 10^6 m^3/yr from the western coast of Terschelling by Steetzel (1995, in Dissanayake et al., 2009). The tidal prism is 430 10^6 m^3 (Sha, 1989b).

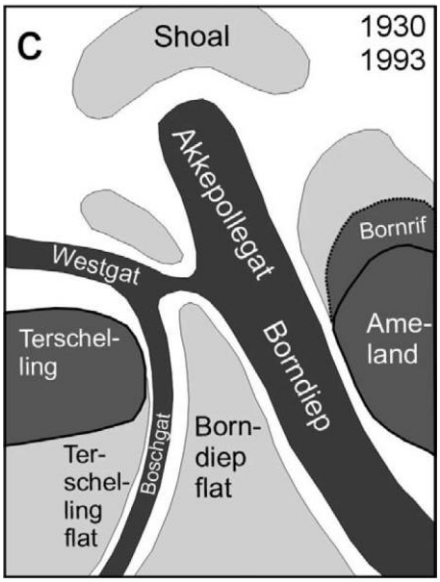

Figure 2.22. The nomenclature of the Ameland Inlet (Cheung et al., 2007)

The general current patterns, corresponding to the current models of Sha (1989b, Figure 2.11) and Sha and van den Berg (1993, Figure 2.10), can be illustrated by the modelled currents in Figure 2.23, showing one tidal cycle during a storm (Swinkels, 2011). During ebb, the water flows out of the tidal basin radially over the ebb delta, the offshore main current is westwards. During flow reversal the offshore current is still westerly directed and the basin empties still through the ebb channel. Waves drive the south-easterly directed current over the ebb

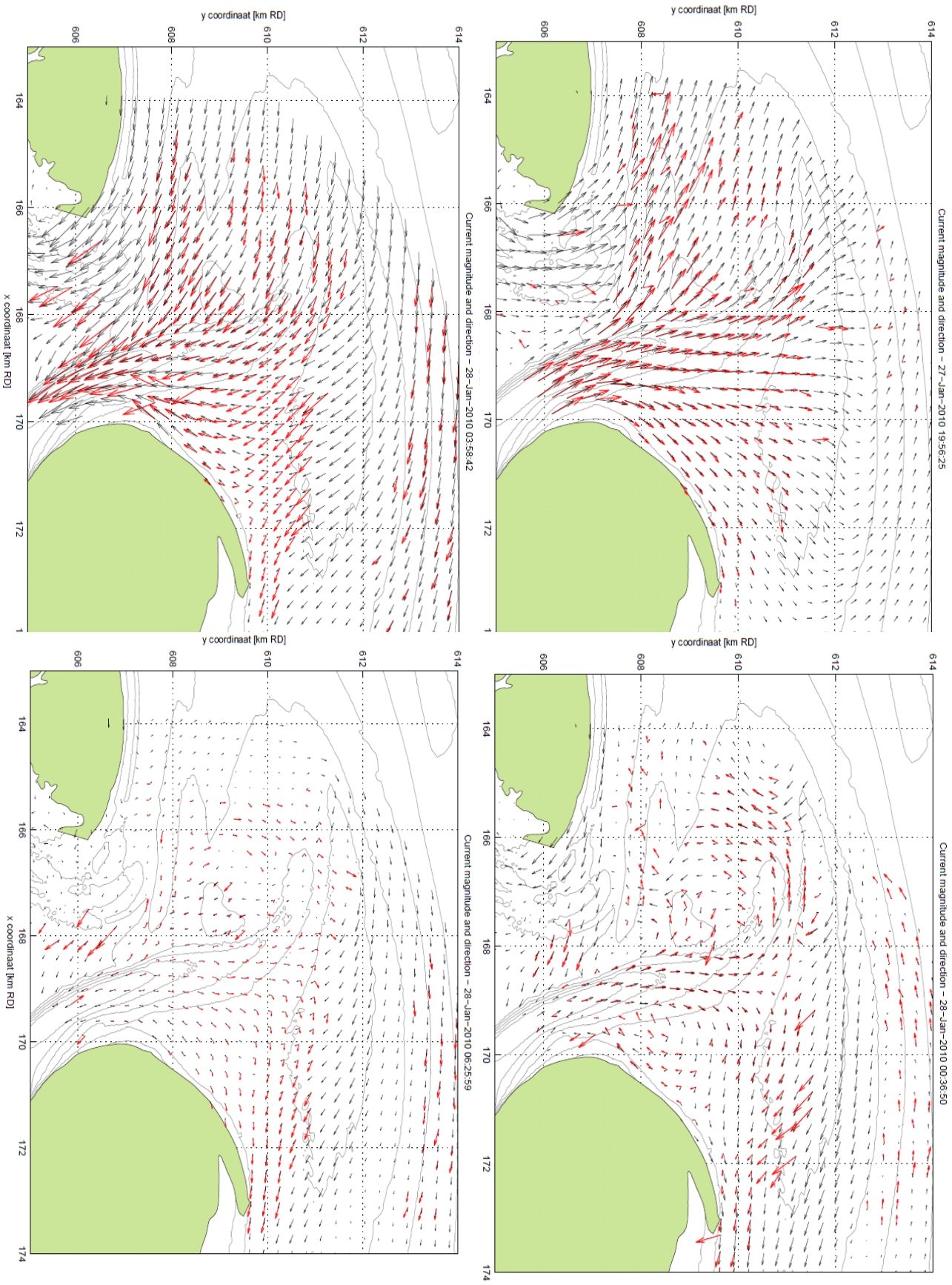

Figure 2.23. Swinkels (2011) compared radar inferred currents (red) to modelled (black) currents (in Delft3D), clockwise for mid-ebb, ebb slack, mid-flood and flood slack.

shoal and along the Ameland North Sea coast. Besides, a rotational current (eddy) arises northwest of the head of Ameland, by interaction of the differently directed currents. During flood, the southward and eastward current split at the head of Ameland is more pronounced than during the preceding tidal stage (ebb slack). The rotational current disappears by the strong cross-shore flow into the basin. The off-shore current is directed eastwards. At flood slack, water flows through the eastern channels of the inlet out the basin. In the western channels still water flows in and the offshore current is still eastwardly directed.
Swinkels (2011) validated the D3D model of the Ameland Inlet using currents extracted from the marine X-band radar. Although currents found from the radar images show lower spatial coverage than the D3D model, still general current patterns can be observed (red arrows, Figure 2.23). Swinkels (2011) observed three major differences between model and radar. First, the unrealistically large current magnitudes at the edge of the ebb shoal can be explained by distorted radar observations due to a steep slope in the computational cubes or due to wave breaking. Second, a small lag in time of the modelled currents initiates differences in radar inferred and modelled current. Thirdly, radar current magnitudes are slightly overestimated, because the model and radar output are respectively a depth-averaged and surface current. After sensitivity runs of the numerical model, the current magnitude and direction correspond quite well to the radar observations (Table 2a). The sensitivity runs include a locally optimized bathymetry, inclusion of local wind, 3D model, inclusion of eddies and a spatially (and temporally) varying bed roughness. Especially, the Van Rijn (2007) spatial varying bed roughness improved the modelled currents.

Simulation	R0-def	R1-bth	R2-wnd	R3-hls	R4-3d	R5a-rgh	R5b-rgh	R5c-rgh	R5d-rgh
Velocities									
Corr.coefficient (-)	0.77	0.78	0.77	0.77	0.70	0.83	0.83	0.82	0.75
Bias (m/s)	-0.09	-0.09	-0.09	-0.09	-0.06	-0.03	-0.02	-0.05	-0.04
RMSE (m/s)	0.23	0.23	0.23	0.23	0.25	0.19	0.19	0.20	0.24
Scatter Index (%)	36.4	36.1	36.9	36.4	42.7	32.3	32.8	32.7	39.9
Symmetric slope (-)	0.84	0.84	0.84	0.84	0.91	0.95	0.96	0.92	0.94
Directions									
Corr.coefficient (-)	0.65	0.66	0.63	0.65	0.53	0.79	0.78	0.78	0.59
RMSE (°)	39.4	38.9	40.6	39.4	48.2	30.2	30.7	30.9	45.1
Scatter Index (%)	9.0	8.6	9.4	9.0	9.5	9.8	9.6	9.8	8.9

Table 2a (Swinkels, 2011). The statistics are shown for the five sensitivity runs in D3D, as default R0, with partially updated bathymetry R1, local uniform wind R2, inclusion of the sub module HLES to improve eddy formation R3, 3D modelled R4 and with spatial varying roughness (Van Rijn, 2007) R5. The latter gave the best results.

Swinkels (2011) compared radar inferred water depth to measured bathymetry (Figure 2.24) and concluded the water depth from radar imaging is under- and overestimated in respectively deep and shallow water. This was also stated by Bell (1999) and Flampouris et al. (2008) and can be attributed to a water depth too large for the waves to feel the bottom, and to an

overestimated wave celerity by linear wave theory in shallow water. Moreover, the abrupt changes from shoals to deep channels make the dispersion relation hard to fit through the large computational cubes. Swinkels (2011) excluded water depths below 2m and above 30m to compensate for the over- and underestimations respectively. Swinkels (2011) concluded the obtained bathymetric estimations are appropriate for qualitative purpose, but not for quantitative purposes.

The wave propagation over the ebb tidal delta and into the inlet differs from ebb to flood, due to respectively an opposing and a following current. The northwest incident waves refract onto the ebb shoal, onto the tidal flats in the basin and partly out of the channels (Figure 2.25). The wave length is large in the channels and decreases on the tidal flats. Waves shoal, break and decrease in height (also by bottom friction) on the ebb shoal. Gautier and Westhuysen (2010) simulated wave propagation in the Ameland Inlet in SWAN and compared model results to radar inferred dominant wave period, wavelength, wave direction and to image spectra. Dominant (radar) wave characteristics were provided instead of the in SWAN used peak wave characteristics. The dominant was determined as the wave characteristic corresponding to the maximum energy in 3D wavenumber-frequency (k_x, k_y, f) space, while the peak was determined as the wave characteristic corresponding to the maximum energy in a 1D spectra. Gautier and Westhuysen (2010) transformed the SWAN peak wave length and direction to dominant length and direction, so model and radar wave parameters can be compared properly. To estimate the significant wave height a spatial image spectra field was provided for one measurement (1.6min), during flood.

A first estimate of the significant wave height was obtained using a very rough frequency-independent modulation transfer function, as MTF=1/3000. Though, the transferred radar spectrum and the buoy spectrum are nearly identical (Figure 2.26), wave height estimated for the spatial image spectra field proves unsatisfactory when comparing to a modelled wave height field (Figure 2.27).

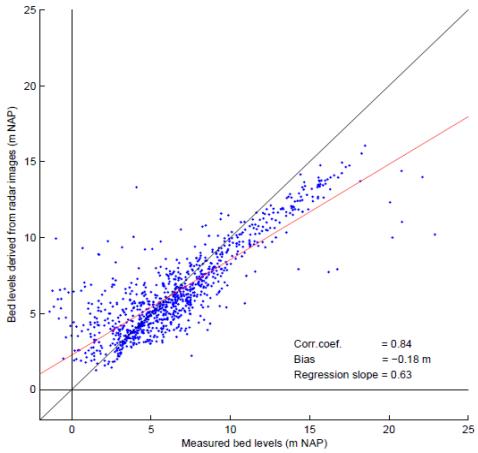

Figure 2.24 (Swinkels, 2011). Measured against radar inferred bed level show over- and underestimations in respectively shallow and deeper water.

SWAN shows better results than the radar (Figure 2.26), when compared to wave buoys. They recommend improved data filtering (on frequencies and currents) to optimize the results.

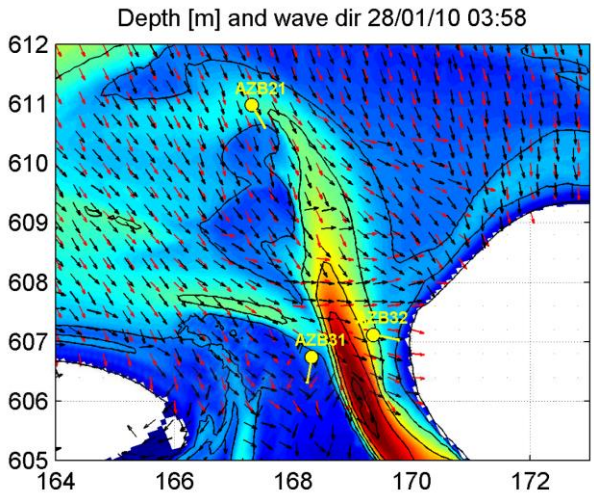

Figure 2.25. Waves refract on the shoals and cross the ebb channel, at 28 January 03:58 (mid-flood) (Gautier and Westhuysen, 2010). The modelled, radar inferred and buoy inferred wave directions are indicated in respectively red, black and yellow arrows.

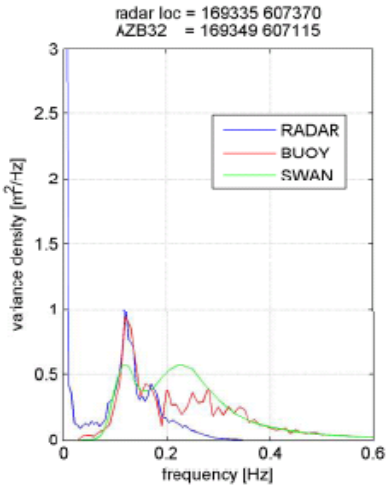

Figure 2.26 (Gautier and Westhuysen, 2010). The radar spectrum is converted to a wave spectrum by multiplying the image spectrum with 1/3000, assumed as very rough MTF. The radar energy peak corresponds to the buoy peak quite well, though energy at low (high) frequencies is over- (under) estimated.

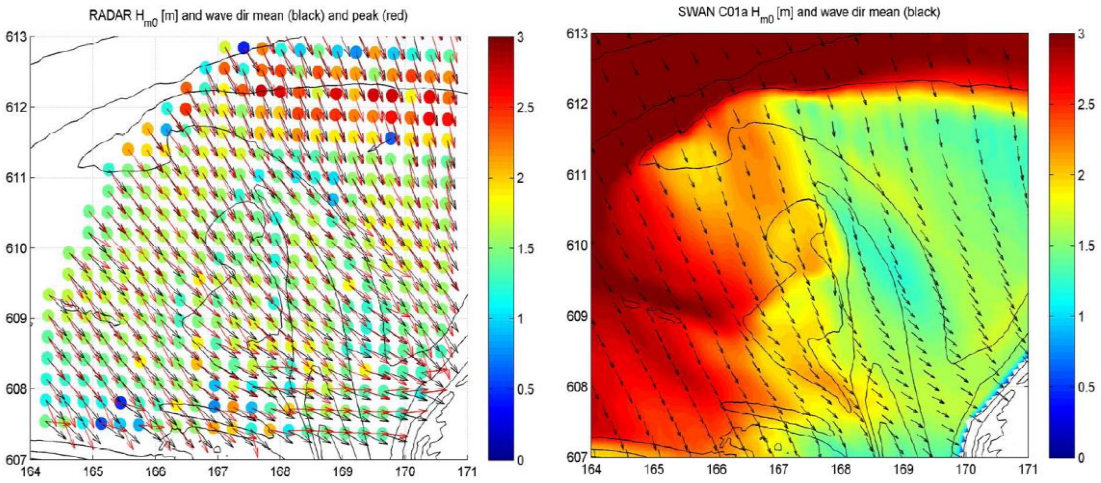

Figure 2.27 (Gautier and Westhuysen, 2010). Wave height estimated from transferred radar image spectra (left) does not give satisfying results, when comparing to modelled wave height (right).

3. Objective, hypotheses and research questions

Marine radar images are used to monitor at open sea or in the coastal zone and radar images are used for comparison to in-situ measurements or numerical model results. Due to the large temporal and spatial resolution of radar imaging, radar data are useful for calibration or validation of numerical models. However, the quality of radar derived wave characteristics is unknown, especially in complex bathymetries in the coastal zone, leading to the following main objective, hypotheses and research questions.

Objective

The objective of this thesis is to find the wave field quality of radar images, based on respectively radar-based quality estimators (1) or numerical-based quality predictors (2).

Radar-based quality estimators (1) prepare image data for time series analysis and eventually model validation. Numerical-based quality predictors (2) can *predict* radar wave field quality, using a numerical model. The predicted wave field quality can show whether a (X-band) radar is the right (future) instrument to monitor waves in a coastal area and if so the wave field quality predictability helps to choose the optimal location of the system.

The approach is to determine the temporal and spatial wave field quality variability in marine X-band radar images from the Ameland Inlet for two storms in 2010.

Hypotheses

The following hypotheses are put forward.

1. The marine X-band radar (at the head of Ameland) can monitor the sea surface (wave period, wavelength and wave angle), during storms over a gradually varying bathymetry.
2. The quality of radar wave field can be found by using radar-based quality estimators or numerical based quality predictors, which estimate or predict quality reduction factors. Quality reduction factors can be based on two methods; evaluating the data filter used to remove wave field outliers and comparison of radar and SWAN wave fields, assuming a perfect model.
3. Wave height can be estimated from radar wave spectra, which follow from radar image spectra transferred by an empirical based Modulation Transfer Function.
   The empirical Modulation Transfer Function is composed of the ratio of 1D frequency buoy and radar image spectra and is frequency dependent.

Research questions

The hypotheses are tested by answering the questions below in the following sections. The most important questions are answered in the Conclusions. The main question follows from the objective and reads

1 Can radar inferred wave field quality be predicted?

The following questions are sub questions, which help to answer the main question and can be answered from bottom to top (here).

Hypothetically, quality decrease might be related to certain temporal or spatially varying processes, where the wave field quality predictor could be based on and therefore

2 Which are quality reduction factors for radar inferred wave fields?

To answer question 2, the temporal and spatial variations in radar derived wave field will be studied first, which may indicate quality reduction factors. However reference material or ground-truth is needed, to determine which temporal and spatial variations represent low wave field quality. For lack of densely spatial covered ground-truth data, two methods will be used to indicate when and where wave field quality decreases. The first method will be based on the available radar data, while the second method will be based on radar measurements compared to a wave model. The questions to study

3 Method 1: When and where were radar inferred wave fields filtered thoroughly in the temporal and spatial extensive radar data set?

4 Method 2: When and where show wave fields or spectra large differences in the radar-SWAN comparison?

Before those methods can be applied the radar and SWAN data has to be processed and a filter for the radar data has to be developed. First the questions preceding to method 1 are explained and read as

5 How can the radar inferred wave field be filtered? And what do the wave fields look like after filtering?

First, temporal and spatial variations usual in radar inferred wave field should be studied, before a proper filter can be developed which removes the radar wave field outliers showing unusual behaviour, therefore

6 How do radar inferred wave period, wave length, wave angle and image spectra change from the radar measurements offshore boundary, over the ebb tidal delta and into the ebb channel, during a storm?

7 Where and when do the radar derived wave fields show outliers over the Ameland ebb delta study area?

To study method 2, SWAN and radar wave period, wavelength, wave direction, spectra and wave height should be comparable. Unfortunately, wave height cannot be provided directly from radar image spectra, but could be estimated by applying a Modulation Transfer Function on the image spectra, so

8 What is the empirical based Modulation Transfer Function?

9 What does the radar image spectra derived wave height look like?

For comparison the SWAN wave output has to be converted to wave characteristics similar to the radar derived wave characteristics;

10 What do the SWAN dominant wave fields look like?

Furthermore, this method assumes SWAN predicts the wave field characteristics for comparison perfectly. When this assumption holds, SWAN output should correspond to ground-truth buoy measurements exactly, which seems to be unrealistic. Therefore SWAN will be compared to buoy measurements and evaluated in a sensitivity analysis, raising the question

11 Which hydrodynamic processes are under- or overestimated in SWAN?

4 Dataset

Wave data were derived from wave buoys and from the wind wave model SWAN to evaluate the radar wave field quality. Additionally, information from wind and water level stations was used. This chapter treats the measured data, collected by in-situ instruments and the radar. Tables can be found in the back of this report.

4.1 In-situ measurements

Several ground-truth measurements are available nearby the Ameland Inlet. The choice of a number of wave buoys and wind stations used in this study is motivated below. After, the time series of measurements are described, collected during the period of radar monitoring of the storms in January and October 2010.

Twelve (directional) Waverider buoys are located in and nearby the Ameland Inlet and in the back barrier basin (Figure 4.1). Particularly four wave buoys (AZB 21, AZB 22 (no directional buoy), AZB 31 and AZB 32) were used in this study, located in the Ameland Inlet within the radar range (Table 4a). The locations of the buoys in January 2010 were slightly different from those in October 2010, because in the meantime the buoys were removed for maintenance and were replaced afterwards. Except wave data from AZB11 and AZB12, the SWAN model used wave information from the offshore directional Waverider buoy Eierlandse Gat (ELD) and Schiermonnikoog Noord (SON) (Figure 5.2). The buoys gave wave energy density and directional spreading every 10 minutes of measuring per frequency bin (J/m^2Hz), known as 1.5D spectrum. Several measures for wave height and wave period (or frequency) can be derived from the frequency-energy wave spectrum. Especially buoy derived 1D frequency energy density spectra were used in this study; as ground-truth in the sensitivity analysis of SWAN and to develop a Modulation Transfer Function to estimate wave height from radar image spectra.

Water levels were measured south of Ameland at Nes (nearest to Ameland Inlet) and at the station Terschelling Noordzee every 10 minutes during the storm in January 2010 as well as the storm in October 2010.

During both storms ten minutes averages of wind speed and direction (converted to +10mNAP wind) were available at three (Fast recorder) wind stations in the North Sea: Terschelling Noordzee, Wierumergronden and Huibertgat. For January 2010, wind was measured additionally at the Wadden Sea stations Hoorn and southwest Terschelling and at Lauwersoog. Wind data were lacking partially for the Terschelling Noordzee and Wierumergronden station during, respectively, the October storm and the January storm. The wind direction from the Huibertgat station was the only available directional data for the

January storm, because wind direction missed for the wind station at Hoorn and Lauwersoog and the (new) Terschelling Noordzee and Wierumergronden wind stations were not tuned yet (in January 2010, Rijkswaterstaat DID in Gautier and Westhuysen, 2010). Therefore, wind speed was used from the closest Wierumergronden station, while wind direction was used from the Huibertgat station during both January and October storm.

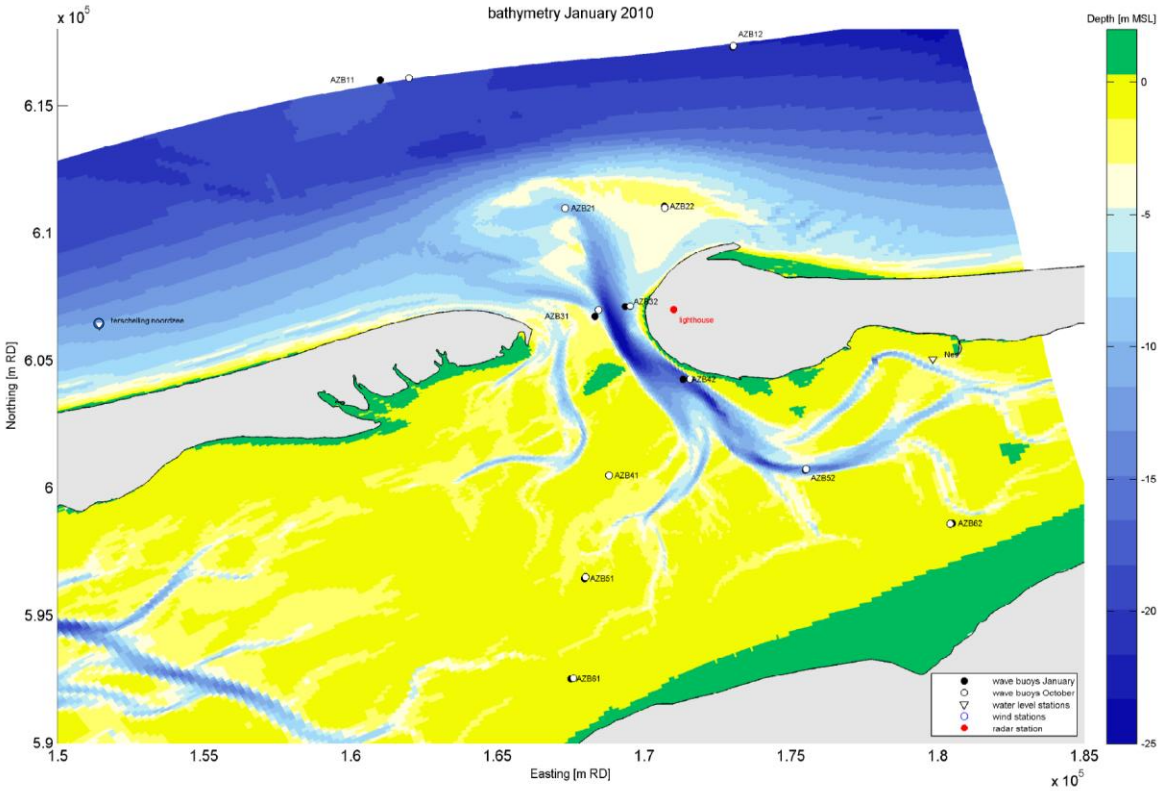

Figure 4.1. Bathymetry of the Ameland inlet in January 2010 and measurement locations.

Figure 4.2 shows the time series of wind and wave height at the twelve buoy locations around the Ameland Inlet and the water level at Nes. Especially the outermost buoys AZB 11 and AZB 12 showed the storm signal clearly. In January, the storm strengthened and the wind turned more northerly with the strongest conditions during the flooding tide from 28 January 00:00 UTC (Coordinated Universal Time) onwards. Offshore wave heights reached 3.5m and wind speed was around 12m/s (Figure 4.2). In October, the storm was heavier and lasted longer (Figure 4.2). The storm peaked two times, on 20 and 24 October, by north northwestern winds of respectively 15 and 20m/s and off-shore wave heights of 4 and 5m. During 21 October, the wind speed remained quite high (15m/s), though the waves lowered to 3m with two smaller storm peaks. The wind weakened to 11m/s and turned to the south-west during 22 and 23 October and then the wave height fell below 2m.

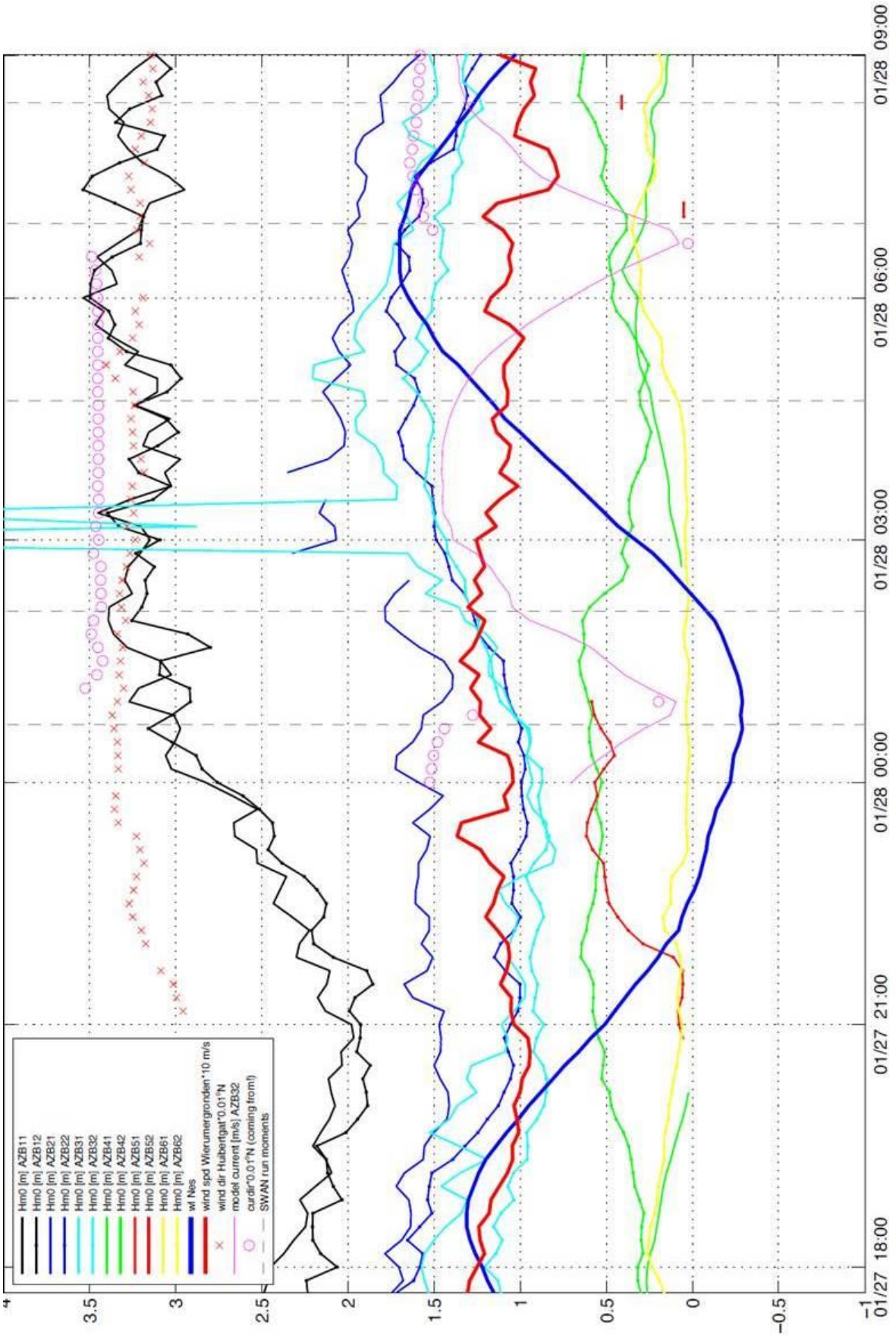

Figure 4.2a. Time series of water level, wave height, wind speed and wind direction in January 2010.

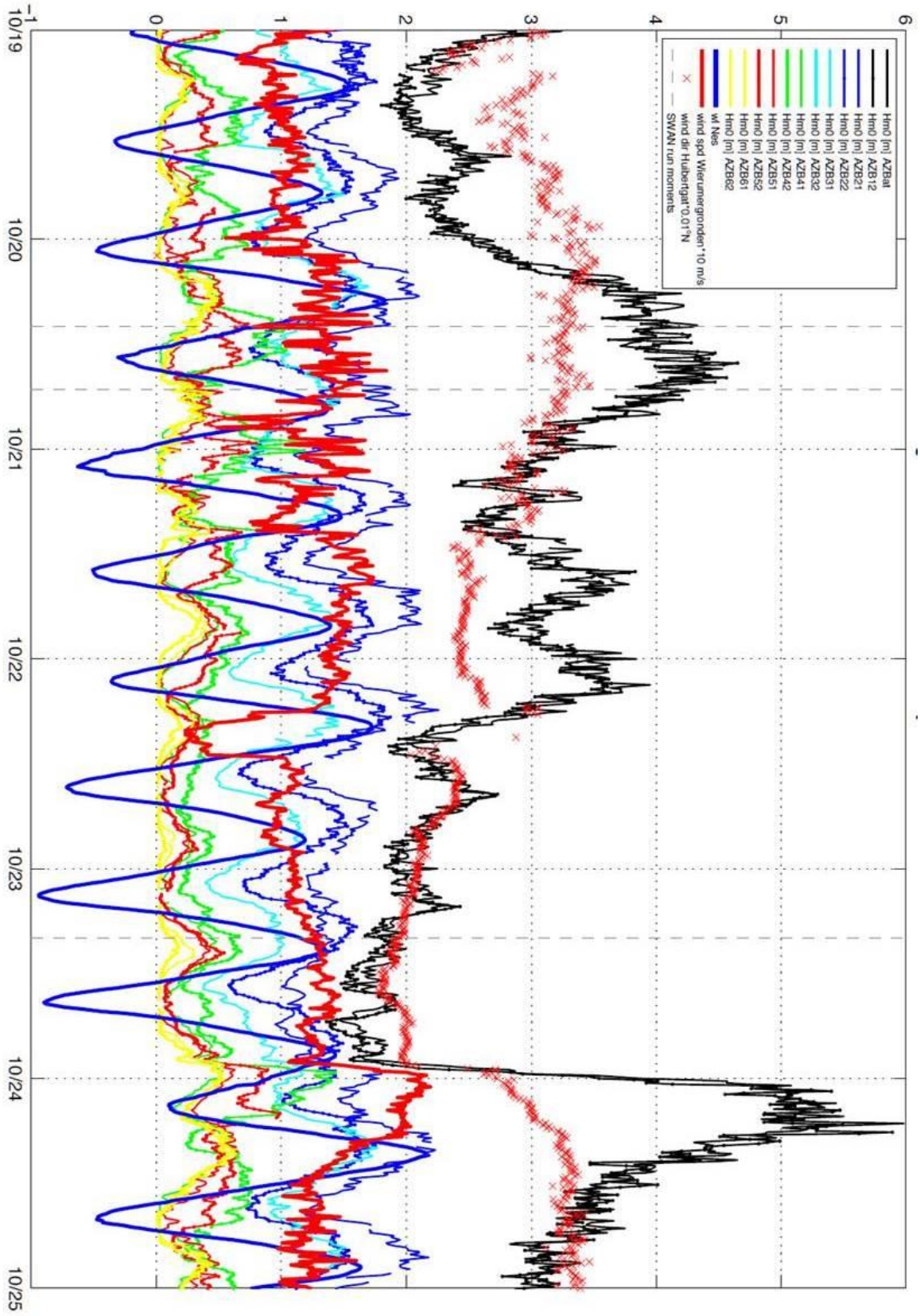

Figure 4.2b. Time series of water level, wave height, wind speed and wind direction in October 2010.

4.2 Radar measurements

This section explains the preprocessing from near-shore radar image sequences into the provided image spectra and their derivative wave characteristics as spatial maps, performed by radar processing company Nortek using the SeaDarQ software package.

Set-up radar system

Waves, currents and water depth in the Ameland Inlet were monitored by the marine X-band radar scanner on top (58m, Table 4b) of the Ameland lighthouse (53°26.951'N, 5°37.546'E) (Figure 4.3) during two storms: from 27 January 18h until 28 January 2010 10h and from 18 October 23h till 24 October 2010 09h. The radar rotates around a vertical axis, records the sea surface within a radius of 7.5km and produces a circular image of each rotation with a radius of 1000 pixels. The radar (with 18ft Terma antenna) rotates in ~2.85s and sends pulses of 50ns in horizontal polarization, with a wavelength of 3cm and a frequency of 9.6GHz. During 1.5min of recording, 32 circular images were obtained with a temporal resolution of 2.85s, used as sub dataset to derive wave characteristics, currents characteristics and water depth at the concerned sample moment. The range resolution of one pixel in the radar image was 7.5m, since the pixel range resolution is related to the pulse length ($0.5 \cdot 50 * 10^9 \cdot 3 * 10^8$) (Section 2.3.1.1). The maximum azimuthal pixel resolution was 54m, since this resolution is related to the radar range and to the horizontal antenna beam width (here 0.41degrees at 3dB) (Section 2.3.1.1).

Figure 4.3. Radar on top of Ameland lighthouse (Wikipedia).

Pre-processing

The north eastern half of the circular images was used to derive wave and current characteristics and water depth. In the upper part of the circle the radar was able to notice waves because: sufficient wave energy is present for wave imaging, waves propagate opposite to the radar view direction and waves show dispersive (linear) behaviour. First, Nortek converted the time series of 32 circular images with wavy patterns of sea clutter (Section 2.3.2.1) to unfiltered and uncorrected image spectra $I(k_x,k_y,\omega)$ at 946 output points (Figure

4.4) by a 3D Fourier Transform over computational cubes of 960m (128pixels) x 960m x 32. Fourier Transforms on the computational sets overlapped spatially, as the Fourier Transforms with the 960x960m computational cubes were performed on a grid with a 300m cell size. The sampling and processing time was 13 minutes to provide image spectra and derive and save spatial maps of wavelength, wave period, wave angle, current magnitude, current direction and water depth at 946 output points. So, the temporal resolution of the wave characteristics is 13min. Current and bathymetry deformed the image spectrum particularly in the high and low frequency part respectively. Therefore, a non-linear fit on either the high or low frequent part of the image spectrum was used to obtain the current and depth. A dispersion shell fitted through the 3D data cloud of wave numbers and frequencies removed irregularities from the image spectra, e.g. arising by buoys or ships. Subsequently, wave characteristics were extracted.

Besides the abovementioned spatial maps of wave and current characteristics and water depth, 2D frequency-direction image spectra are available for the northwest quarter of the radar view area at 28 January 2010 02:11 UTC and time series of image spectra are available at the four inlet buoy locations for both the storm in January and the storm in October. The temporal resolution of the spectra time series is around 4min, since the processing time was less for the four buoy locations than for a spatial field of 946 points. Also spatial resolutions differ for the several radar-derived wave characteristics and image spectra; both temporal and spatial resolutions are given in Table 4c. The sample locations of the January and October image spectra time series were slightly different, because the buoys were taken and placed back at slightly different locations (Table 4a) after maintenance works in the summer of 2010.

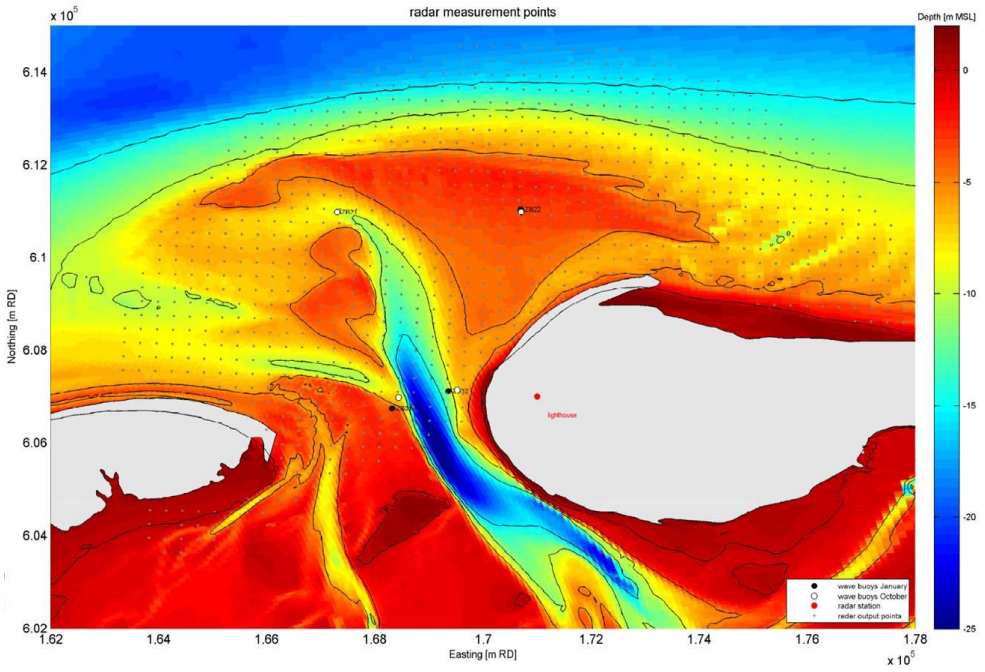

Figure 4.4. Radar output locations in the Ameland Inlet.

As example of the raw radar data provided by Nortek Figure 4.5 shows the dominant wave period and the corresponding spatial variability in wave period at ebb slack (28 January 00:18:53 UTC). The period increases to about 20s at the outer edge of the ebb tidal delta and above the shoal western of the ebb tidal channel. Similarly large wave periods appear at the eastern edge of the radar view area and south of the y-coordinate 607000m. From now on those high values will be referred to as outliers. Except the outlier pattern in a single wave period (or wavelength) field, their temporal and spatial variability can be studied (Appendix A1).

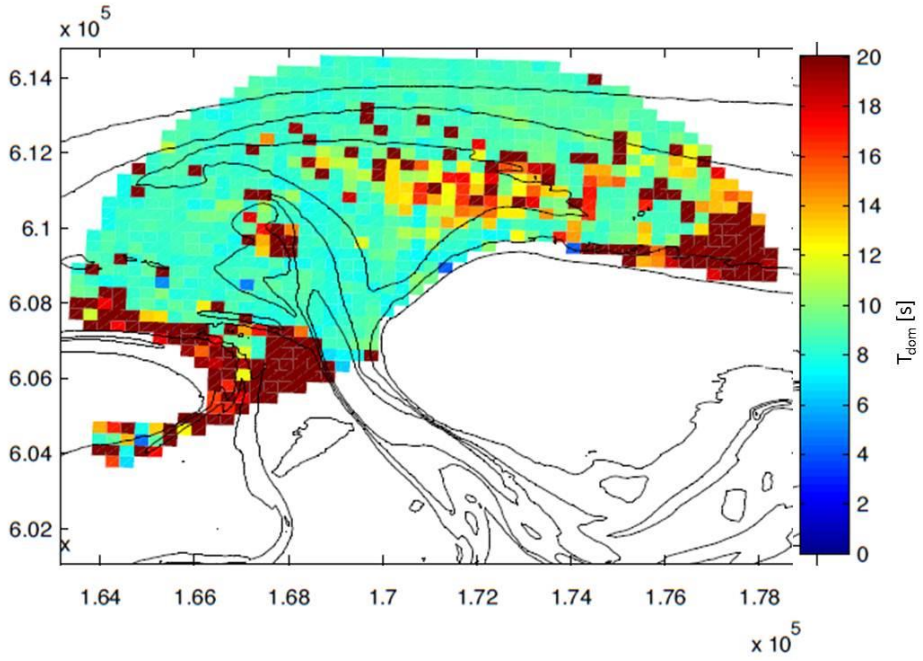

Figure 4.5. Radar inferred dominant wave period at ebb slack, 28 January 00:18:53 UTC.

Measurement limitations

The spatial and temporal resolutions of the radar imaging prescribe a range within which waves can be monitored by the radar. Here, wavelengths can be measured between 15m (2 x pixel size) and 960m (length computational cell) and only wave periods above 3s were monitored. Image energy of waves with a period between 3s and 6s might be underestimated, because wave periods which are multiples of 2 times the sampling interval can accidentally be noticed as an alias of the concerned wave period. Its corresponding frequency is known as Nyquist frequency. Image energy with a period above and around the Nyquist frequency might be slightly overestimated, where the aliases are found. However aliasing may be negligible here, since the alias frequency can be recognized in a 3D spectrum. Thus, the alias frequency can be brought back to its original frequency, except for waves on the Nyquist frequency exactly or for waves propagating in the exactly opposite direction of another wave.

5 Approach and methodology

The main objective of this study is to estimate or predict wave field quality in radar images. Figure 5.1 shows an overview of the overall approach and methodology.

Radar wave field quality is approached by six different radar-based quality estimators or numerical-based quality predictors (2), which show when and where the (individual) quality reduction factors (3) dominate. To find which factors or physical phenomena reduced the radar wave field quality, two methods (4, 5) were developed and used to indicate how the radar wave field quality varied temporally and spatially. The results of the two methods combined gave an acceptable estimate of the spatial and temporal quality variability, wherefrom quality reduction factors were interpreted. The first study (4, 5) only focuses on the quality variability. The variability is explained and linked to physical phenomena when interpreting the quality reduction factors.

The first method evaluates both radar data (spatial and time-trend) filters (6) for each wave characteristic. The percentage of removed outliers at each grid cell indicates zones of lower quality. The percentage of removed outliers for each radar image shows how the wave field quality varied with time.

The second method gives zones of under- or overestimated wave characteristics in SWAN-radar difference plots. Those zones may point to either lower radar or SWAN wave field quality. An extra test to find whether under- or overestimations are presumably SWAN or radar induced, is comparison to the concerned filtered radar wave characteristic of Method 1.

The by Nortek provided radar data (limited amount of 1D frequency and 2D frequency-direction image spectra and spatial maps of wave period, wavelength and wave direction) and the need of using SWAN in Method 2 required preliminary analysis for both radar and SWAN data, indicated by the blue background (Figure 5.1). Method 1 asked for developing a filter (6) which removes outliers. Method 2 asked for SWAN inferred wave characteristics similar to and on the same grid as the available radar data (7). A Modulation Transfer Function (MTF) needed to be developed (8) to convert radar image spectra to energy density spectra to find a radar derived wave height (9). In addition to compare SWAN and radar derived wave period, wavelength and wave direction also wave height can be compared (Method 2).

The processing of the radar data with the filter and the MTF design is described below, followed by the set-up and subsequent processing steps of SWAN (Section 5.2). The two developed methods are applied and interpreted in Section 6.

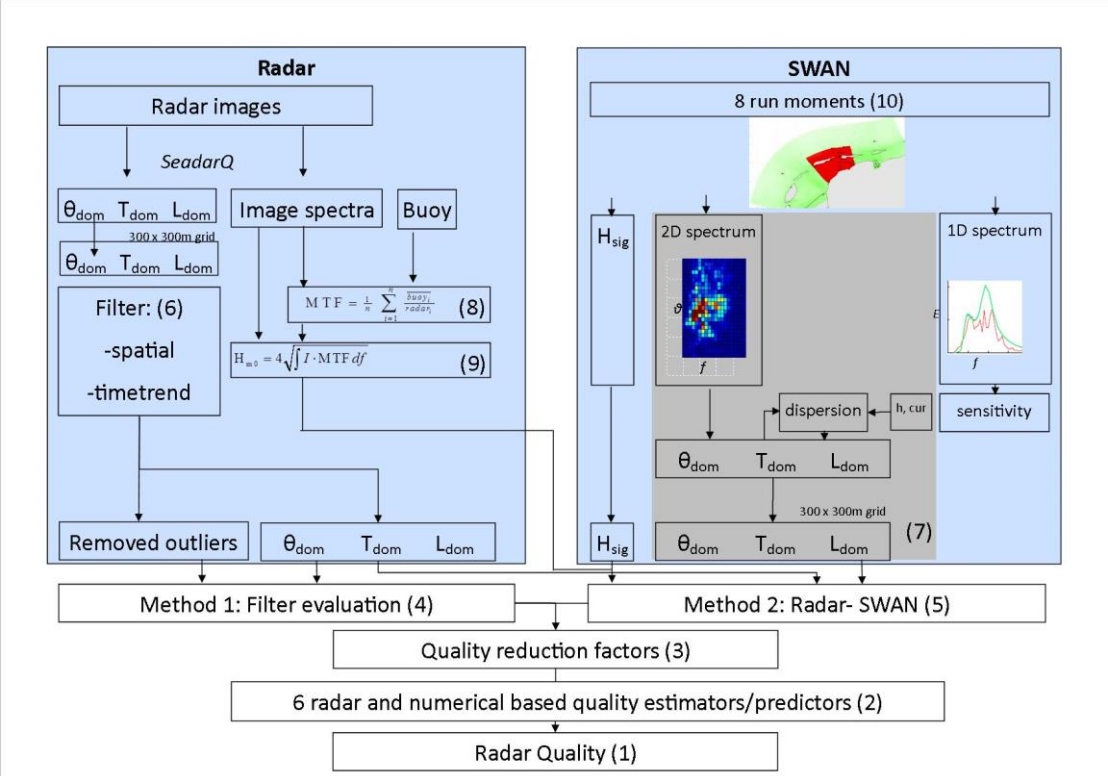

Figure 5.1. Overall approach to obtain quality of wave data inferred from radar images.

5.1 Radar

Grid interpolation

Nortek preprocessed the radar images and provided for this study the wave characteristics wave period, wavelength and wave direction at 946 (x,y) locations with almost regular 300m spacing. The (x,y) radar data points had to be interpolated to a regular grid (Figure 4.4) with an exact 300m x 300m cell size, for proper comparison to the SWAN wave data. In this thesis, all spatial radar data are presented on this regular grid.

Filter design

As was mentioned in Section 4.2, the radar data contained outliers (Figure 4.5). A preliminary analysis in the temporal and spatial variations of outliers (Appendix A1) helped to develop a filter to remove outliers. Outliers were removed by a combination of two filters; a spatially based and a time-trend based filter. Filter criteria were determined for each wave characteristic individually.

The spatial filter removed the values that differed more from the median of all values at a certain moment than the (trial- and- error based) spatial filter criterion of 3s or 35m for respectively the wave period or wavelength. Such a spatial filter does not perform well for the vector wave direction. Instead, wave directions were removed outside the ((usual) coming from) directional range of 225 to 30 degrees.

The time-trend filter removed values that are out of the exceedance boundary around a linear trend over a certain time span. The exceedance boundary was drawn by two times the standard deviation, fixed at 2.5s and 3s and 20m and 25m for the standard deviation of respectively wave period and wavelength. The standard deviation was fixed in case of either high or low standard deviations to keep the filter effectively. The wave direction time-trend criterion is 3 times the standard deviation and fixed at 25 and 30 degrees for respectively a lower or higher standard deviation. A criterion of three instead of two times the standard deviation was used to not tighten the filter too much, due to the low standard deviations of the better quality wave direction compared to wave period and wavelength.
Qualitative analysis showed filter results improved when the wave field characteristics were time-trend filtered over smaller time spans, instead of filtering over the entire length of either the January or October time series. Wave period varied particularly with the amount of (off-shore) wave energy (Appendix A1), so their time spans were based on wave forcing at buoys AZB 11 and AZB 12. In contrast, wavelength and wave direction varied particularly with the current direction (Appendix A1) and therefore their time spans were over tidal periods.

Besides wave field characteristics several image spectra of the image spectra time series were removed for consistency. Image spectra were removed, when and where the spatial and time-trend filter removed the wave period. The filtered wave period was used as indicator for good quality spectra, since the 1D frequency- image spectra are inversely related to the wave period and the filters perform well for the wave period.
Image spectra of their spatial dataset at 28 January 2010 02:11 UTC were removed easily at the same grid points removed by the wave period filters. Unfortunately, for the time series of image spectra neither the measurement locations nor the measurement moments do correspond exactly to the radar grid points or moments (of the integrated parameters). The time series of the frequency-directional image spectra was provided at the buoy locations, which were located in between the spatial radar grid points (Figure 4.4). The image spectra were provided with a smaller time resolution (~4min) than the wave field characteristics (~12min). Therefore, image spectra were excluded when the wave period was an outlier at one of the neighbouring four grid points, since the poor wave information at this grid point might contaminate the image spectra (computed over cells of 960mx960m generally). Image spectra were removed also which were collected at a sample moment within 12minutes of the sample moment of an wave period outlier, though the image spectra quality is not known actually for the image spectra sampled in between the wave characteristic sample moments.

Modulation Transfer Function

The not directly supplied radar wave height may follow from a radar wave spectrum. The radar image spectrum represents the backscatter intensity on (the ripples and foam at) the sea surface and thus does not represent wave energy (Figure A9). Radar image spectra were converted to wave spectra, using a Modulation Transfer Function (Section 2.3.2.3). Except the sea surface roughness, the intensity of the backscatter signal depends on tilt, shadowing, range, azimuth and breaking (Section 2.3.1). Analyzing the radar image spectra, described in Appendix A1, helped to design an MTF. Four MTF's follow for the four inlet buoys (AZB 21, AZB 22, AZB 31 and AZB 32) as the ratio of buoy and filtered radar spectra of 27 and 28 January 2010, resulting in a frequency dependent factor:

$$\mathrm{MTF}(\mathrm{f}) = \frac{\mathrm{E}(\mathrm{f})}{\mathrm{I}(\mathrm{f})},$$

with E(f) the wave spectrum measured by a wave buoy and I(f) the radar image spectrum. Only the January spectra were used to determine a MTF, because wave spectra were lacking for AZB 32 during the October storm. The different MTF's could not be compared properly when the MTF's would be based on both the January and the October storm for only three of the four buoy locations. This would hinder to choose fairly one of the four MTF's to apply generally on the image spectra to estimate wave height.
First, the buoy spectra were interpolated on the radar frequency axis to allow division. Thus, the MTF arises along the radar frequency axis with a lower cut-off at the minimum buoy frequency of 0.03Hz and a higher cut-off at the maximum radar frequency of 0.346Hz. Second, both buoy and filtered radar spectra were averaged over 30min, to remove the temporal variance of the buoy and the radar spectra (Appendix A1) and to correct for the different sample time (10 vs. 4min). Without filtering the 30min averages would be based on three (10min) buoy spectra and seven (4min) radar spectra. Filter performance is studied in Appendix A2. Third, the ratio of each 30min buoy and radar average lead to several MTF's for the four buoy locations. A final MTF followed from averaging all 30min- based MTF's for each buoy location. The four MTF's are discussed in Appendix A3, one MTF was selected which will be applied on all image spectra.

Wave height

The radar wave energy m_0 followed from integrating the estimated wave spectrum, which was provided from the product of image spectrum $I(f)$ and the selected MTF

$$m_0 = \int_{0.05}^{0.3} I(f) \bullet MTF(f) df$$

Then the significant wave height H_{m0} (m) followed from

$H_{m0}=4(m_0)^{0.5}$

Note that the buoy wave height H_{m0} is based on a frequency range of 0.03-0.5 Hz, different from the radar frequency range of 0.05-0.3 Hz.

5.2 SWAN

The shallow water (including currents) numerical wave model SWAN (Simulating Waves Nearshore (Booij et al., 1999; Ris et al., 1999)) computed wave spectra. Method 2 compares the output of SWAN to radar derived spectra and wave characteristics. Prior to the radar-SWAN comparison, SWAN output was put onto the radar grid and the sensitivity of SWAN was tested.

Model theory

SWAN was used in third-generation mode, wherein (compared to first and secondary generation mode) wind generation, whitecapping, quadruplet wave-wave interaction and bottom dissipation processes are represented. In addition, SWAN incorporates two additional terms for triad wave-wave interactions and depth-induced wave breaking. SWAN is based on the action density balance in an Eulerian approach, where the wave spectra deform over a spatial grid by sources and sinks.

Here, SWAN version 40.81 was used in stationary mode to model waves in the Ameland Inlet.

Moments of SWAN runs

Eight moments were selected (Table 5a, Figure 5.1 (10)) during the radar monitoring period to run SWAN, since SWAN was used in stationary mode. Since originally one of the objectives was to optimize the SWAN model of the Ameland Inlet by using the radar images, SWAN run moments were selected when the radar images show hardly any outliers and radar wave characteristics were hardly filtered out. Additional selection criteria were stationary wind and wave conditions and a variety of conditions (current direction, water level, wind speed, wind direction) for the (eight) run moments.

Five run moments were selected at 28 January (Figure 4.2), the stormiest day of 27 and 28

January. The run moments were subsequently during low tide, weak flood, mid-flood, high tide and mid-ebb (Table 5a). Three moments in October were selected to include different wave and wind conditions (Figure 4.2). The October runs were during mid-ebb and mid-flood on the stormy 20 October and with a southwestern wind during high tide on 23 October (Table 5a).

Model set-up and input

Input of the SWAN model of the Ameland Inlet were two computational grids, bathymetry, wave boundary conditions, wind, water level and currents, which are outlined below.

A fine (G2) computational grid of the Ameland Inlet was nested in a coarser (G1) grid, covering the Wadden Sea and a small part of the North Sea (Figure 5.2), to reduce computational time. Both grids were curvilinear, so here the coordinate arrays curved around the barrier islands creating the densest grid in the areas of interest (tidal inlets). Cell sizes of the grids are summarized in Table 5b. SWAN computed in nautical convention with 36 directional bins, each of 10 degrees and a logarithmic frequency axis between 0.03 and 1.5Hz for the G1 grid and between 0.03 and 2.5Hz for the G2 grid.

The bathymetry corresponding to the G1 grid consisted mainly of Rijkswaterstaat Vaklodingen from 2007-2008 and LIDAR (Light Detection And Ranging) (laser) altimetry measurements of 2007-2008 (Figure 4.4). The bathymetry of earlier studies (Deltares, 2010) with some new bathymetric data from 2009 was used for the G2 model of January 2010. Partially, bathymetry was re-measured during March-September 2010, resulting in an updated bathymetry for the October 2010 model.

The coarse G1 model used 1.5D frequency wave spectra as wave boundary conditions, including wave energy, mean direction and directional spreading over the frequency axis. Those followed from the off-shore wave buoys ELD and SON (Figure 5.2). West of the ELD and east of the SON buoy the grid boundary used respectively the ELD and SON wave spectrum, these spectra were interpolated for the grid boundary in between. The SWAN computed wave spectra (G1) corresponded better to the buoy observations (AZB 11, AZB 12) at the G2 northern grid boundary when the ELD and SON wave energy was multiplied by 1.21, following Gautier and Westhuysen (2010). A multiplication factor can be expected, since the ELD and SON wave buoys were located in the G1 grid and not on the G1 grid boundary.

2D wave spectra from the G1 model at five locations along the G2 grid boundary (Figure 5.2)

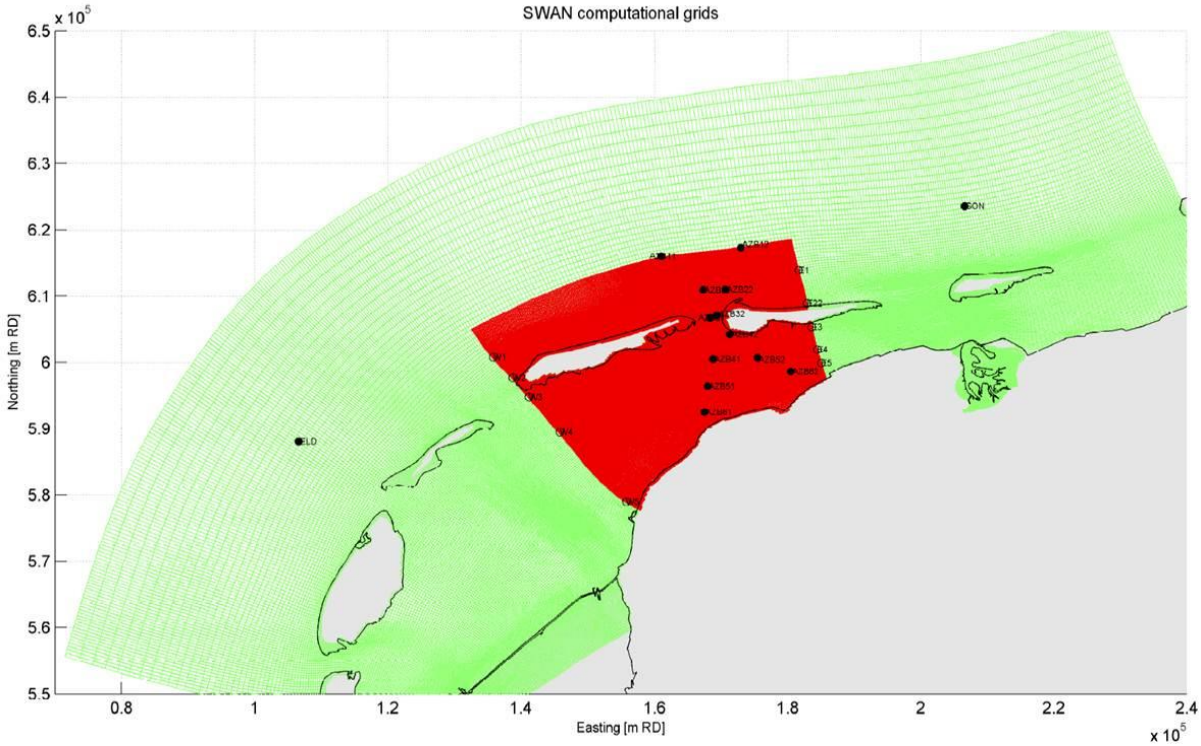

Figure 5.2. The finer G2 (red) grid is nested in the coarser Gw (green) grid. Wave boundary conditions were derived from the buoys ELD and SON for the G1 grid and AZB11 and AZB12 for the G2 grid.

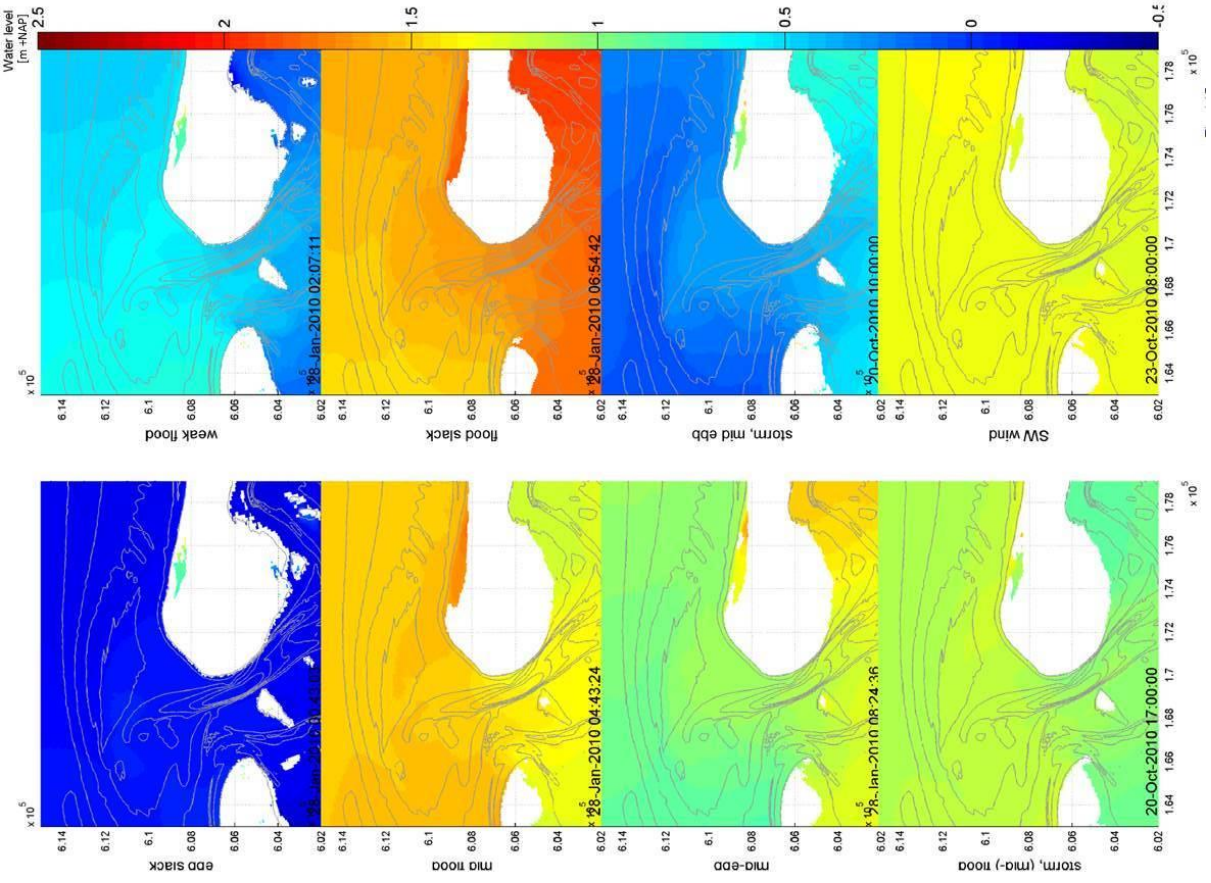

Figure 5.3. SWAN used water level fields from the Wadden Sea Delft3D model as input in the G2 model.

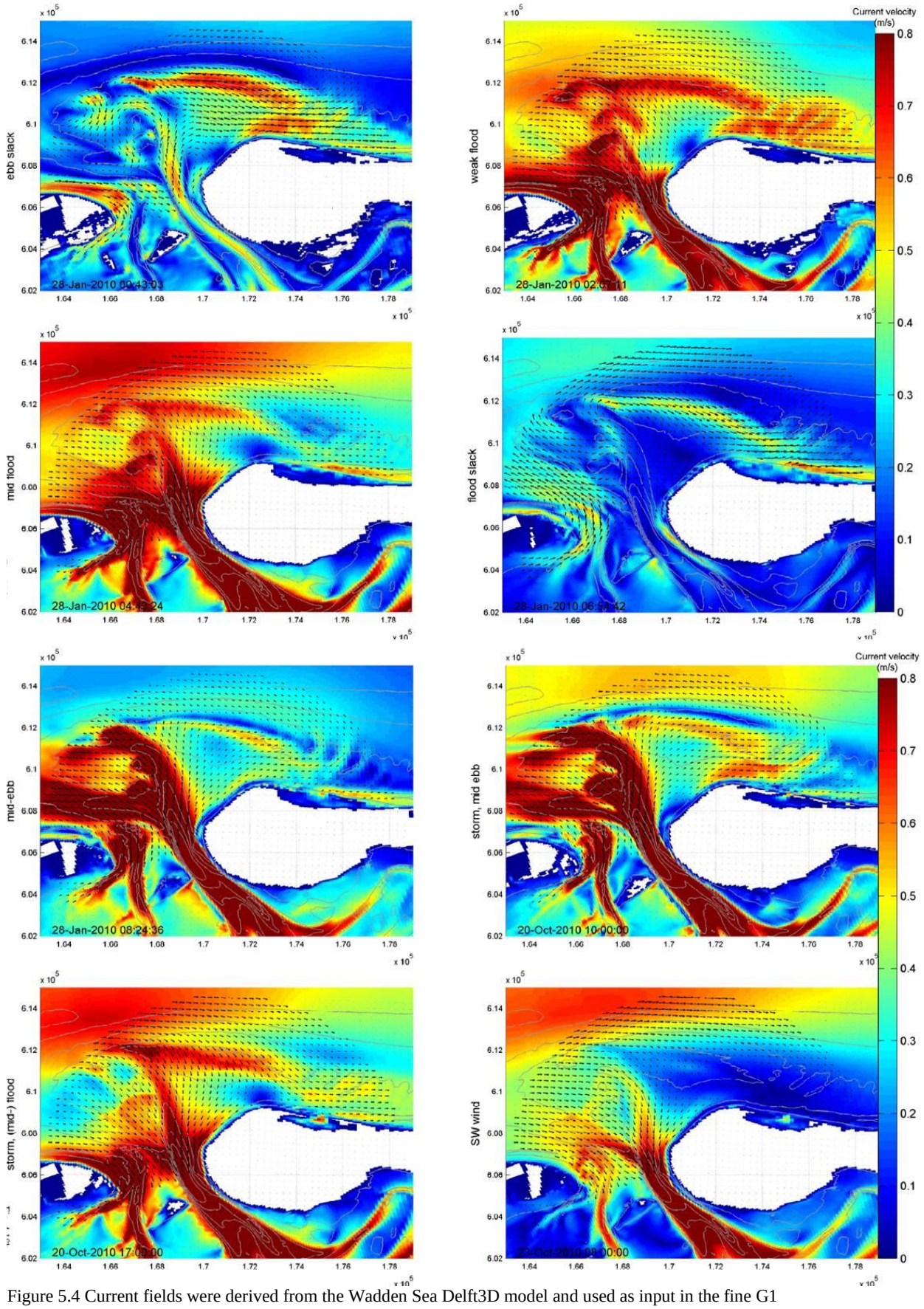

Figure 5.4 Current fields were derived from the Wadden Sea Delft3D model and used as input in the fine G1 model.

were used as western and eastern wave boundary of the fine G2 grid. The wave conditions of the northern (G2) grid boundary followed from interpolation of the wave buoy spectra of AZB 11 and AZB 21, located on the northern G2 grid boundary. The wave spectra of the AZB 11 and AZB 21 were interpolated similarly to the ELD and SON spectra along the G1 boundary.

A constant value for the wind speed and direction (U_{10}) was used, because better results were provided by using a constant value for the wind instead of a spatial varying (HIRLAM) wind field (Gautier and Westhuysen, 2010). The wiggling signal of wind speed and wind direction from respectively the Wierumergronden and Huibertgat station was smoothed slightly before values at the SWAN run moments were extracted. Wind directions were used from Huibertgat, because only here (tuned) directional data were available for the January storm. The water level at Nes (Ameland) was used as input in the G1 coarse model. However, the G2 model computed with a water level field at the selected SWAN run moment (Figure 5.3), with the G2 grid size, derived from the Wadden Sea Delft3D model. Moreover, the G2 SWAN model used current fields at the selected SWAN run moment (Figure 5.4), also derived from the Delft3D model.

Model output

SWAN gave as output several wave characteristics on both grids (e.g. significant wave height H_s), 2D frequency-direction spectra on the fine (G2) grid and both 1D frequency and 2D frequency-direction spectra at the twelve buoy locations.

SWAN dominant wave characteristics

Dominant wavelength, wave period and wave direction were derived from the SWAN 2D frequency-direction spectra to be able to compare to radar inferred dominant wave field data. The dominant wave characteristics cannot be obtained directly from SWAN as output. The maximum energy in the 2D frequency-direction spectra yielded dominant wave period and dominant direction at the fine grid. The dominant wavelength followed from the dispersion relation (eq (2), including currents), using the dominant wave period and the water depth. SWAN provided output at (several) point(s) located in the study area. The spatial distribution of output locations depend on their predefined type in the SWAN script (individual points, along a curve/array or on a computational grid). Each radar spectrum and derived wave field characteristic represent a time-sequence (1.5min) of a spatial cell with sides of 960m (on a (overlapping) 300m grid), since FFT was performed on such time sequences. The SWAN dominant wave characteristics, available over the fine (G2) computational grid, were averaged over spatial cells with sides of 960m around the radar grid points. Resulting, the spatial resolution of the original SWAN wave field (G2 grid) reduced to 300m and the SWAN

wave characteristic field on the radar grid smoothed, since minima and maxima averaged out over the spatial computational cells.

Model settings

The applied SWAN settings in this study followed the settings recommended in the Wadden Sea SWAN calibration study of Gautier and Arab (2010):

- Wind input and whitecapping by the Van der Westhuysen (2007) formulation: rate of whitecapping dissipation c_{ds2}=5 10^{-5}, *br*=0.00175, p_0=4, *powfsh*=1.0
- Quadruplet interactions by the Discrete Interaction Approximation (DIA) of Hasselman et al. (1985): *iquad*=2, λ=0.25, proportionality coefficient cnl_4=3 10^7
- Bottom friction by Hasselman et al. (1973): friction coefficient $c_{f,jon}$ of 0.038 m^2s^{-3}
- Depth-induced breaking by Van der Westhuysen (2009, 2010): α=0.96, *pown*=2.5, *bref*=-1.3963, *shfac*=500
- Triad wave-wave interactions by Eldeberky (1996): proportionality coefficient α_{EB}=0.10, maximal frequency *cutfr*=2.5

For sufficient convergence of the output results, SWAN iterated till the relative local significant wave height changed less than 0.01% between two iterations in 99.5% of the wet grid points, with a maximum number of iterations of 80. The maximum number of iterations was 120 for the fine G2 grid with a similar relative local significant wave height change, but in 101% of the wet grid points. So SWAN always iterated 120 times for the fine G2 grid. Next to a certain significant wave height change threshold the curvature of the iteration curve should be below a curvature criterion of 0.001 to reach sufficient convergence of SWAN's output.

Sensitivity analysis

SWAN was validated using in-situ measurements within the radar view area (wave buoy AZB 21, AZB 22, AZB 31 and AZB 32), because results have to be optimal only within the radar view range for this study. Validation was based on the best fit of 1D frequency SWAN to 1D wave buoy spectra. The 1.5D spectra from the wave buoys limited to a 1D instead of 2D validation of the SWAN spectra. The best fit followed from one of the various 1D frequency (SWAN) spectra resulting from a sensitivity analysis in SWAN, including four series of each five runs at the selected moments in January with different model settings: default, without triad wave-wave interactions, without a current and without wind. The high frequent energy at the channel buoy locations (AZB 21, AZB 32) was overestimated with default settings, which

motivated to select settings affecting the wave energy distribution (over the frequency axis). The effects of the several model settings were studied and the settings were selected which gave the best fit of the SWAN spectra to the in-situ spectra.
Subsequently the radar quality could be evaluated by comparison to the ground-truth validated SWAN model. In future, radar images may validate model results. However, radar image quality and reliability should be known first.

Results from the sensitivity analysis and the motivation to select the model settings above as default is given in Appendix A4.

6 Radar quality

6.1 Zones and conditions of poor quality: filter evaluation

The percentage of removed outliers at each grid cell or for each radar image is a measure for radar quality, for which a low percentage indicates good quality. Poor quality zones follow from the percentages per grid cell, $Q_{spatial}$ [%]. Poor quality conditions can be deduced from the percentages per radar image, Q_{time} [%]. Filter performance follows from Appendix A2.

Zones of low quality

The northern edge of the ebb delta, the western shoal, south of the y-coordinate 607000m and the eastern part of the radar view area show a high percentage of removed wave period, Q_T [%] (Figure 6.1).
The high Q_T in the ebb channel may be attributed to the incorrectly removed low wave period clusters in the channel during a southwestern wind and storm conditions (Appendix A2, Figure A6). Quality of wavelength is low in the same zones as for wave period: the northeastern edge of the ebb delta, the western shoal and the eastern and southern part of the radar view area. Overall quality seems to be higher because the wavelength outliers were not always removed successfully (Appendix A2): Q_L does not represent the wavelength quality well (Figure 6.1).
Wave direction has a lower percentage of removed outliers, Q_ϑ ,than wave period and wavelength. Q_ϑ is high in the southern and eastern part of the radar view area, in the eastern channel of the ebb delta ([172000, 610000]) and northern of the north-ebb delta 5m-depth contour (more northern than for wave period and wavelength). The large percentage of possibly incorrectly removed wave angle in the eastern channel in October compared to January may be explained by the larger variability in boundary and weather conditions during the longer time series.

Wavelength and wave period outliers are expected to be in corresponding zones (and conditions), since they are related via the dispersion relation. Wave direction outliers are not necessarily expected in the same zone because wave direction is not directly related to wave period and wavelength.

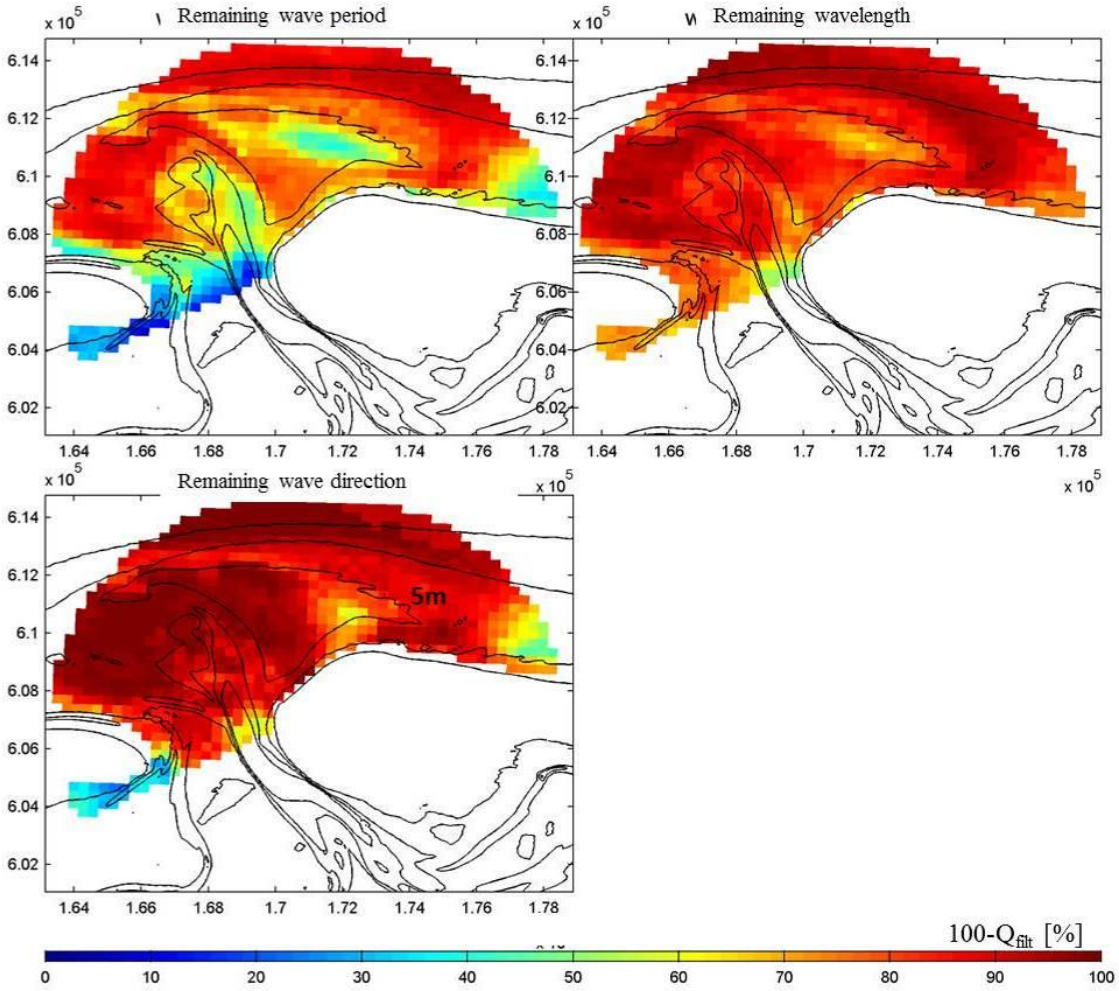

Figure 6.1. Percentage of remaining samples per grid cell after filtering for each wave characteristic in October.

Conditions of low quality

The October time series with percentages of removed outliers (Figure 6.2) shows a clear time dependency, with a periodic signal in Q_T, Q_L and Q_ϑ. Most of the filtered out values were removed by the spatial filter (Figure 6.2), particularly wave period.

The periodic signal is related to the tidal signal: the quality decreased during ebb current and increased during flood current (Figure 6.2 top). Q_T varied between 20% during mid-flood to 40% during mid-ebb. Figure 6.2 (top) shows an increase in Q_T during the storm at 20 October, which can be explained by the incorrectly removed low wave period clusters in the channel (Appendix A2). No high Q_T was observed during a southwestern wind (22 and 23 October), when wave period shows hardly any outliers except the low wave period in the channel.

Q_L is low during the storm at 20, 21 and 24 October (Figure 6.2 middle), because not all outliers were removed successfully. Again Q_L turned out to be not representing the wavelength quality well, as was concluded before for its spatial varying quality. The wavelength during the January storm was filtered better. Then, the quality increased during flood current and storm conditions.

Q_ϑ shows a similar tide related periodic signal as Q_T and Q_L, though the overall percentage Q_ϑ is lower. Q_T, Q_L and Q_ϑ decreased during storm in January (28 January 03:00), while in October only Q_ϑ did (19 October 18:00-20 October 24:00, 24 October).

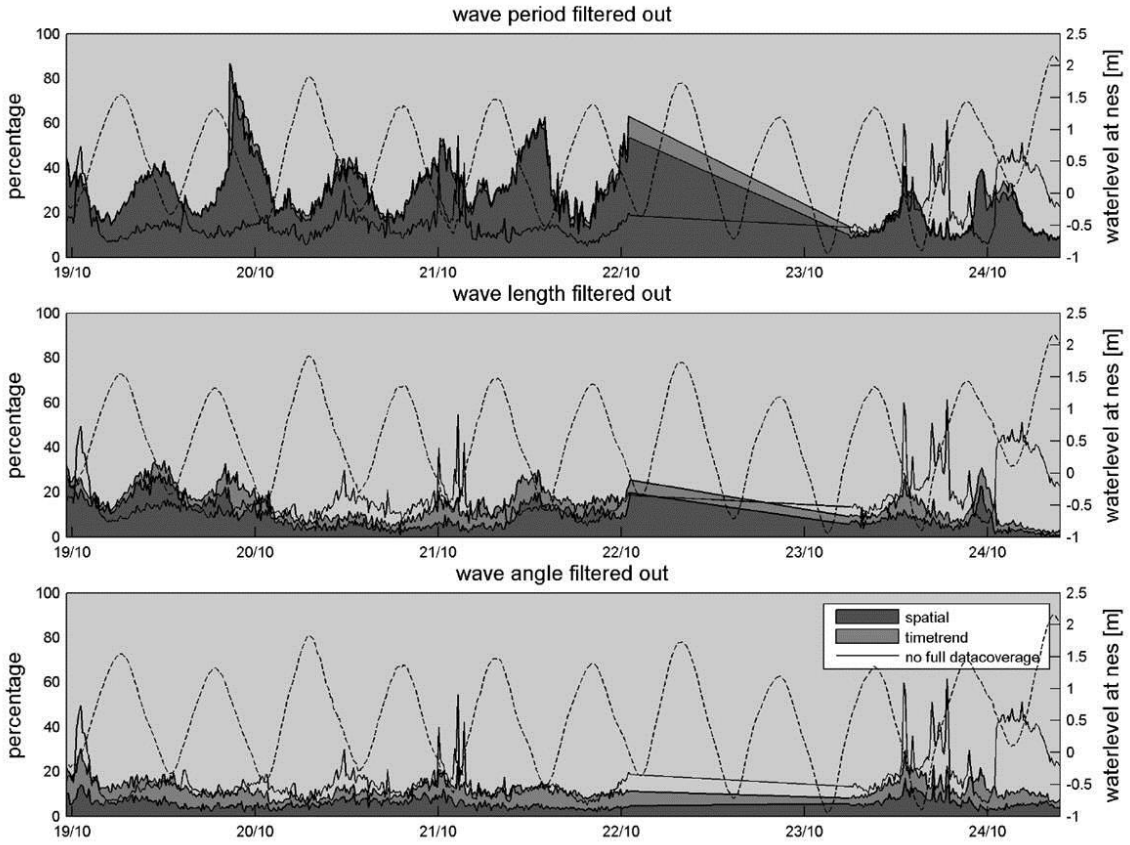

Figure 6.2. The percentage of removed outliers by the spatial (dark grey) or time-trend (grey) filter per image from 19 to 24 October for wave period (top), wavelength (middle) and wave direction (bottom). The water level (dashed line) and the percentage per image when no current and depth was found (solid line) help to identify low quality conditions.

6.2 Zones and conditions of low quality: SWAN-radar comparison

Wave period

Figure 6.3.k-o shows overall agreement of SWAN and radar inferred wave period; both radar and SWAN dominant wave period grow during storms.

Dominant radar wave period was higher than SWAN wave period (red) in the following zones: the Terschelling shoreline, the eastern part of the radar image, the western shoal, the northern edge of the ebb tidal delta and the ebb channel. Overall the radar-SWAN wave period differences reduced during rising tide. Most of the zones with large wave period differences correspond to the zones from which outliers were removed (Figure 6.3.p-t).

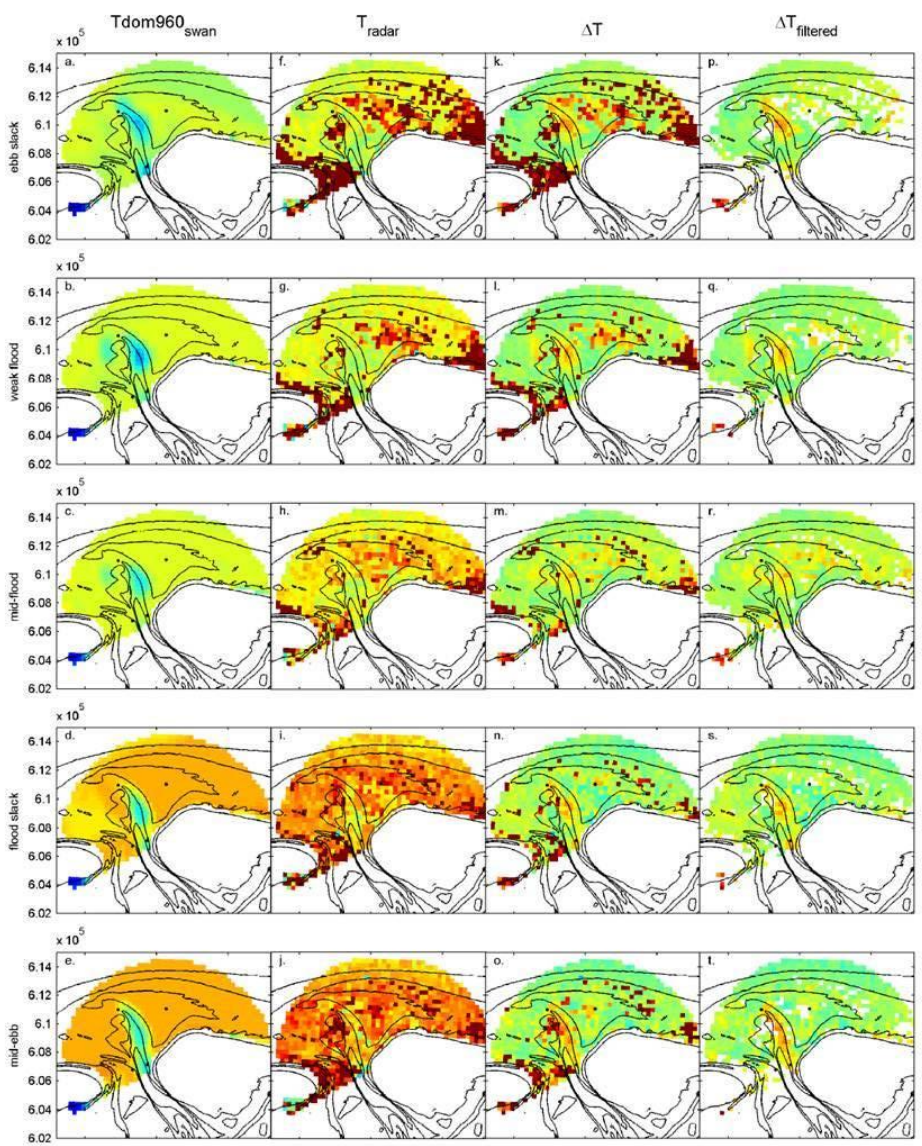

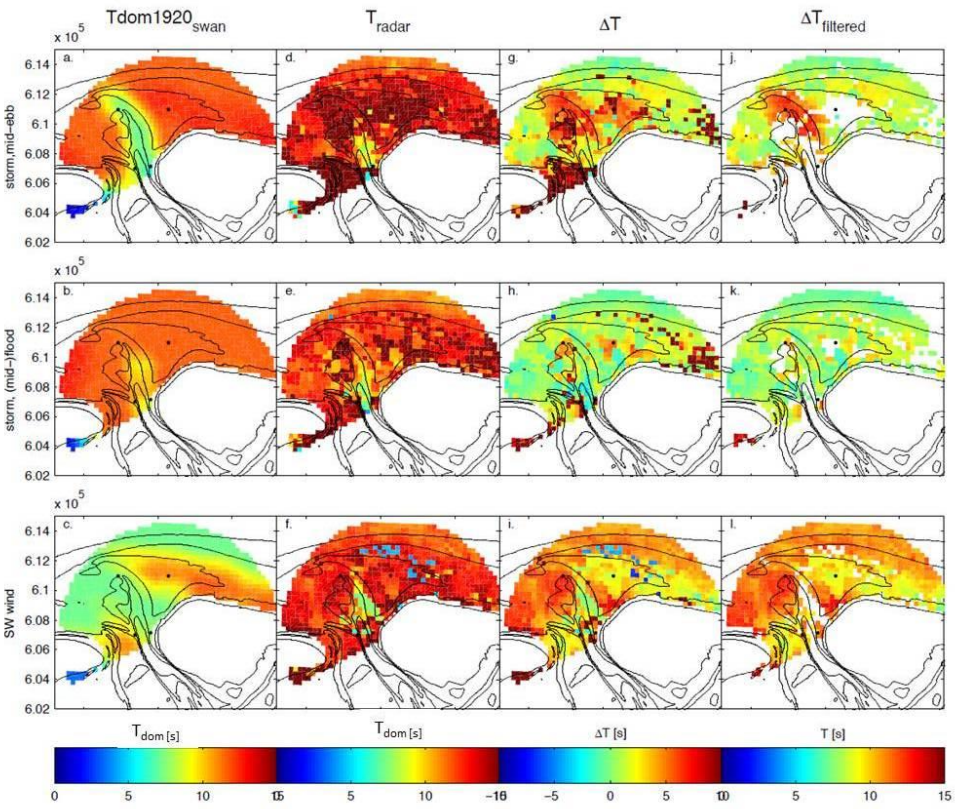

Figure 6.3 (left). SWAN (a-e) compared to radar (f-j) wave period with $\Delta T=T_{rad}-T_{SWAN}$ (k-o) at 28 January. Figure 6.4 (top). SWAN (a-c) compared to radar (d-f) wave period period with $\Delta T=T_{rad}-T_{SWAN}$ (g-i) in October.

The two methods filter evaluation and radar-SWAN comparison agree (6.3p-t, 6.4j-l), showed by plotting the filter results on top of the radar SWAN comparison.

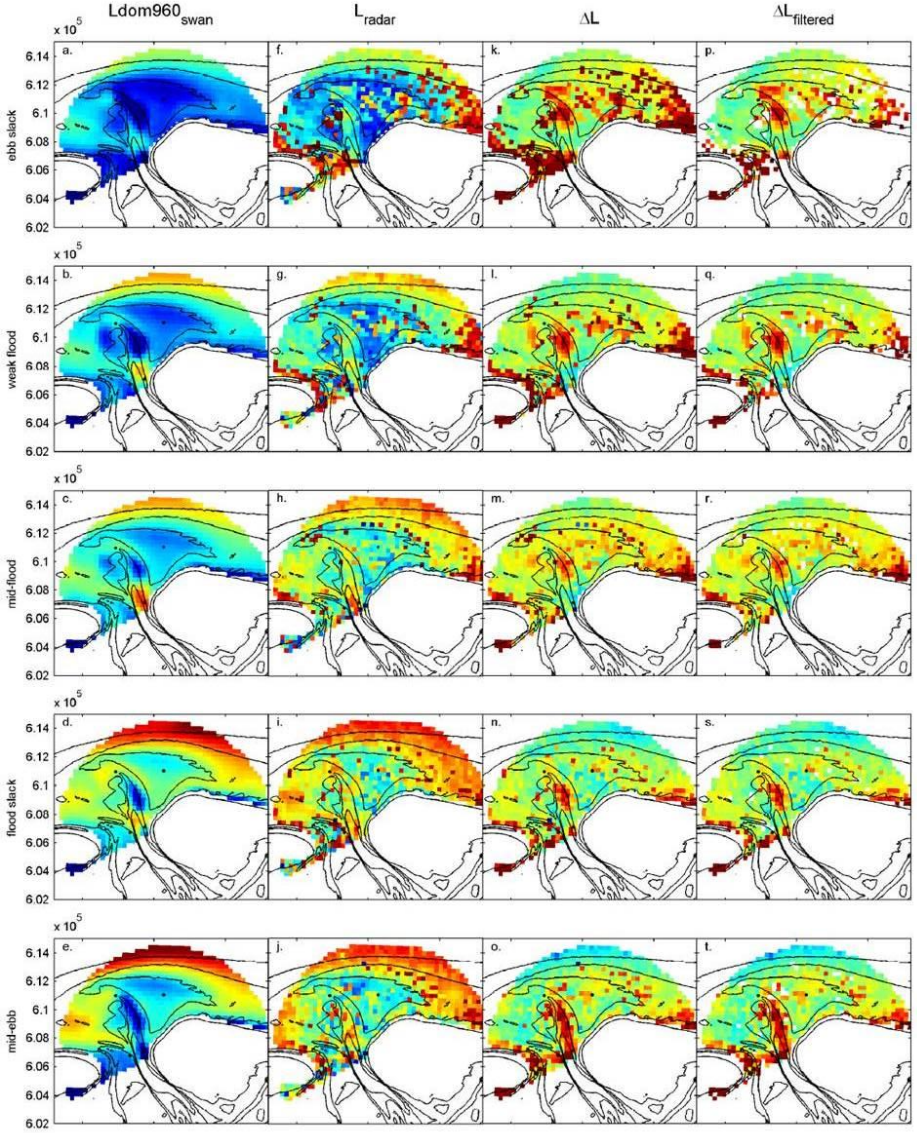

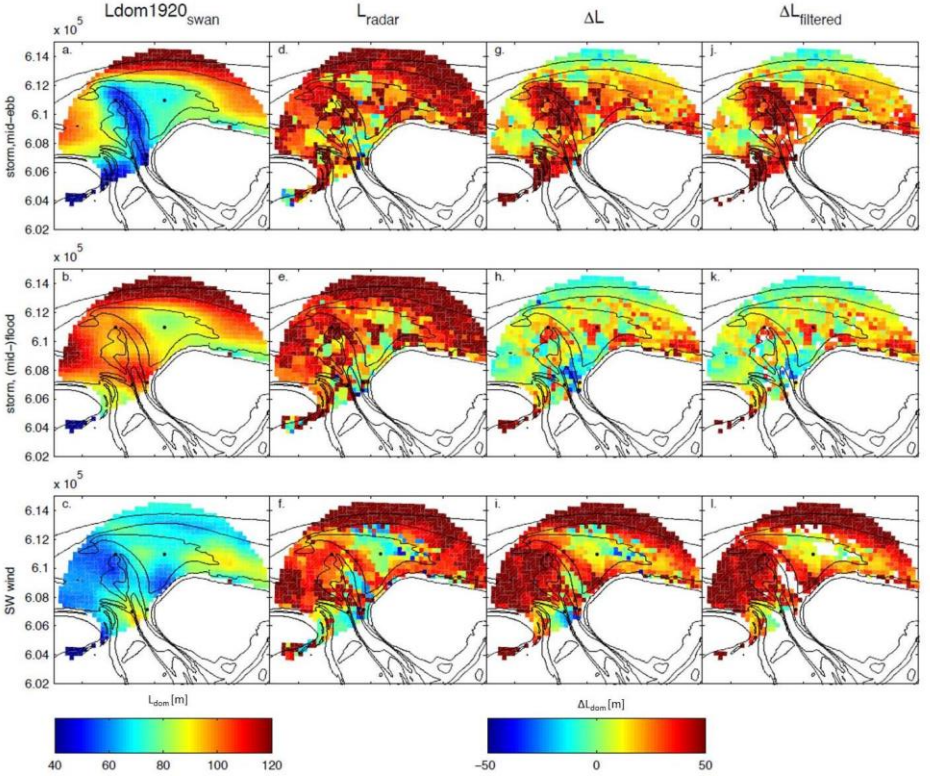

Figure 6.5 (left). SWAN (a-e) compared to radar (f-j) wavelength with $\Delta L=L_{rad}-L_{SWAN}$ (k-o) at 28 January.
Figure 6.6 (top). SWAN (a-c) compared to radar (d-f) wavelength with $\Delta L=L_{rad}-L_{SWAN}$ (g-i) in October.

The two methods filter evaluation and radar-SWAN comparison agree (6.5p-t, 6.6j-l), showed by plotting the filter results on top of the radar SWAN comparison.

Filter results do not correspond to the SWAN-radar comparison in the ebb channel: no outliers were removed but SWAN wave period was much lower than the radar wave period, especially during high energetic conditions. During low energetic conditions and in absence of a strong current waves from the northwest crossed the channel at y=608000m, explaining the higher period (and wavelength). The unconformity of low wave period can be explained by the radar as well as by SWAN. The radar did measure a decrease in wave period in the ebb channel during high energetic conditions and during a SW wind (Figure 6.3.i-j, Figure 6.4d-f), but radar wave period was still higher than predicted by SWAN. SWAN's bimodal energy spectrum regarding to the unimodal radar image spectrum might be the cause of the wave period difference; slightly different distributed energy in the bimodal spectrum can easily change the dominant wave period with a few seconds (Figure A9, e.g. spectrum at AZB32 during flood slack).
Not many wave periods were removed by the filters during a southwestern wind, though SWAN and radar wave period were quite different which may be either radar or SWAN induced.

Wavelength

Figure 6.5.k-o shows radar and SWAN wavelength agree and disagree in the same zones and during the same conditions as was found for the wave period. The red colors in Figure 6.5.p-t show the data filters and SWAN-radar comparison do not give the same low quality zones, which can be explained by the lower performance of the radar wavelength filter. Radar and SWAN wavelength differed much in October (Figure 6.6), which could be attributed to the poor quality of the wavelength itself in this month.

Wave direction

Most of the zones of low quality found in the wave period and wavelength radar-SWAN comparison were also found for wave direction, with two exceptions: the southeast part and the northern edge of the ebb delta.
Large differences between SWAN and radar wave direction arose (1) at the southeast part of the ebb tidal delta, (2) in the ebb channel and (3) more scattered along the Terschelling shoreline, at the eastern part of the radar view area and northern of the ebb tidal delta (Figure 6.7, Figure 6.8). Observed large differences for wave period and wavelength at the northern boundary of the ebb delta were hardly present for wave direction.

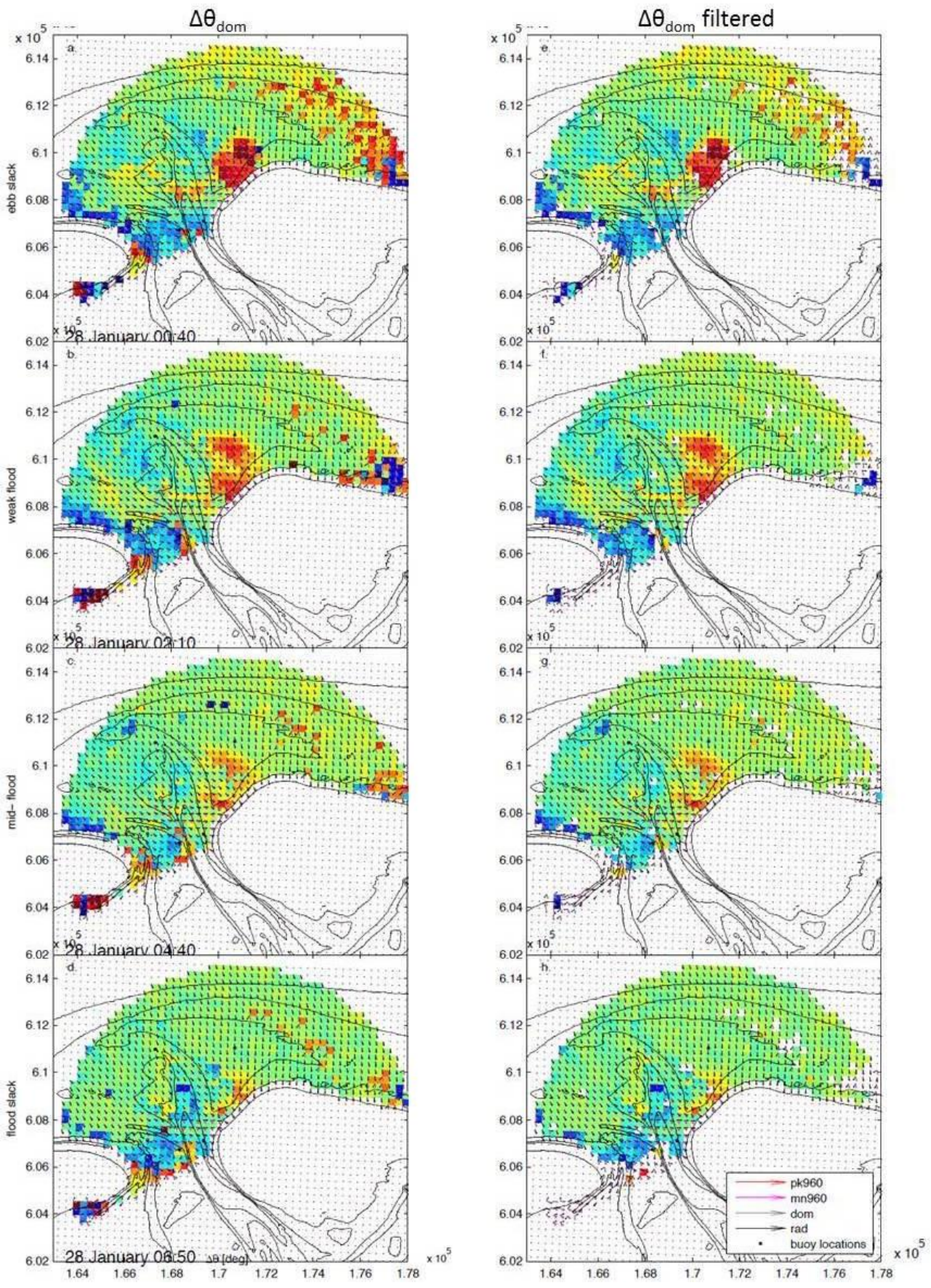
Δθdom
Δθdom filtered
ebb slack
weak flood
mid– flood
flood slack
28 January 00:40
28 January 02:10
28 January 04:40
28 January 06:50
pk960
mn960
dom
rad
buoy locations

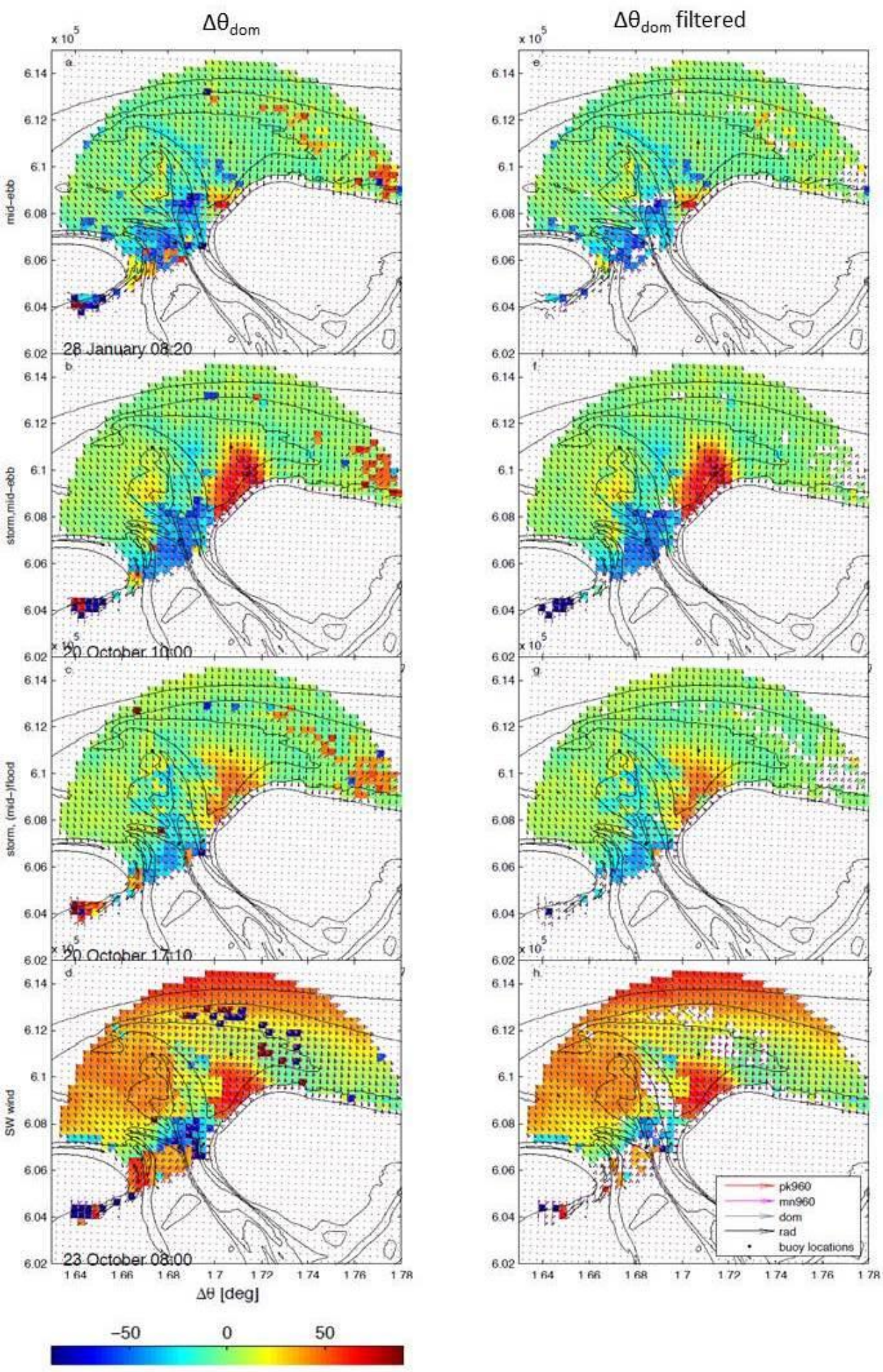
$\Delta\theta_{dom}$
$\Delta\theta_{dom}$ filtered
mid–ebb
storm,mid–ebb
storm, (mid–)flood
SW wind
28 January 08:20
20 October 10:00
20 October 17:10
23 October 08:00
pk960
mn960
dom
rad
buoy locations
Δθ [deg]
−50
0
50

Figure 6.7 (pp.73), Figure 6.8 (left). The difference between radar (black arrow) and SWAN dominant (grey arrow) wave direction ($\Delta\theta=\theta_{rad}-\theta_{SWAN}$) shows where radar wave direction might have a low quality. The 'dominant' as measure may contribute to the large directional differences. A peak (red arrow) direction will less easily deviate tens of degrees when energy was distributed slightly different in the bidirectional SWAN spectrum. Filter evaluation and radar-SWAN comparison (e-h) agree for the scattered outliers in the northern and eastern part of the image.

1. The large directional difference at the south-east part of the ebb delta could be caused by the radar which could not notice narrowly binned (south) easterly propagating waves (in a dominant magnitude) predicted by SWAN and the radar overrated the energy in the view direction. But on the other hand, the wave energy of the westerly incident waves may be overestimated by SWAN.

The more eastern directed waves (predicted by SWAN) on the southeast part of the ebb delta can be ascribed to the bidirectional wave field predicted by SWAN (Figure 6.9). Northerly incident waves, westerly incident waves crossing the ebb channel and northwesterly incident waves refracting on the (tidal) current met and interacted at this part of the ebb delta. The rate and extent of the radar-SWAN difference varied with time, since the SWAN bi-directionality is related to energy of the wave field and the tide. The radar-SWAN difference and SWAN's bi-directionality was smallest during strong tide combined with calm wave conditions; northwesterly incident waves were hindered to cross the ebb channel.

In case of bi-directionality or bimodality (for wave period) a 'dominant' measure may give results easily deviating (up to 80 degrees), a peak measure will be more adequate to study wave direction. A multi-directional field including a small wave group with narrowly binned energy has a 'dominant' in the direction of the small wave group, though most of the energy of the wave spectrum may be in a different (peak) direction. A peak (SWAN) direction deviated less with the dominant radar direction, since the peak represented the direction at the peak frequency in a 1D spectrum instead of a 2D spectrum.

2. A large directional difference arose where the radar inferred waves appeared to cross-over the ebb channel generally, while the by SWAN predicted waves followed the ebb channel during a stormy mid-ebb (Figure 6.8.a-b). Possibly the waves refracted into the channel due to the ebb current. During the storms waves refracted less on depth, since the waves entered more northerly and thus propagated rather parallel to the (channel) depth contours. The directional difference in the channel can also be explained again by the bimodal wave field and radar view direction. Waves following the channel cannot be seen by the radar (around y=607000m) when they were (nearly) normal to the radar view direction.

3. Large directional differences northern of the ebb delta, around Terschelling and the eastern part of the radar view area can be attributed to the radar, since this zone corresponds to the zone where (most of) the grid cells were removed by the filters (Figure 6.7.e-h, Figure

6.8.e-h).

To conclude the SWAN- radar wave direction comparison, the SWAN and radar wave direction (but also wave period and wavelength) did not agree during a southwest wind when swell waves may be expected (Figure 6.8d). SWAN may not be able to predict (a mix of wind) and swell waves accurately, since SWAN was originally developed as wind wave model. The large difference can also be attributed to the radar, which may not be able to see the low waves.

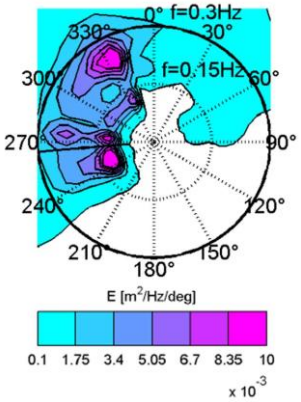

Figure 6.9. SWAN predicted a bi-frequency spectra in the ebb channel ([~169000,~609000]) at weak flood on 28 January 02:11:09. (coming from) Energy distributed over different directions in the ebb channel and on the ebb delta shoal because different directed wave groups met here, but also due to refraction.

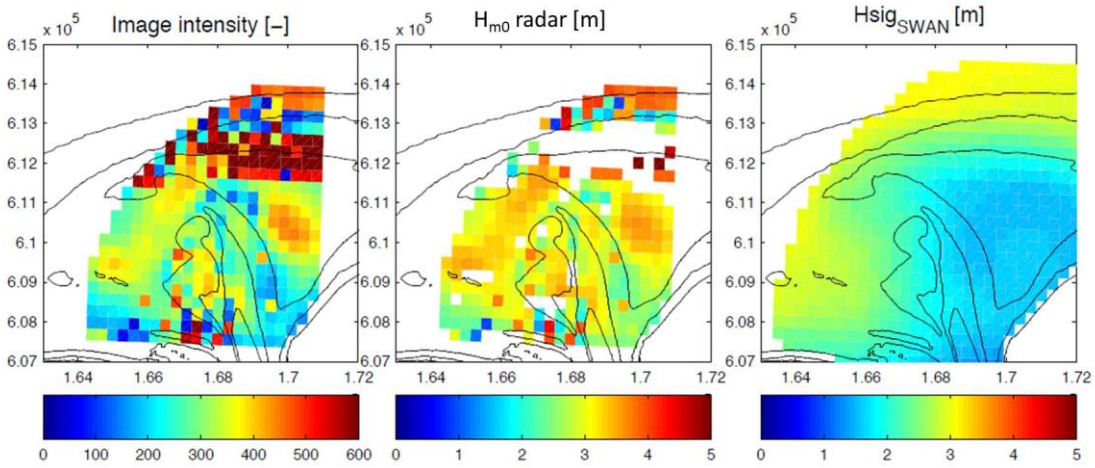

Figure 6.10. Wave height at weak flood on 28 January 02:11:09. Radar wave height was derived from radar image spectra using a MTF. Image intensity integrated over the frequency (left) decreased shoreward and is extraordinary high around the northern edge of the ebb delta. Radar inferred wave height (middle) does not correspond well to SWAN significant wave height (right).

Wave height

The radar wave height is overestimated by inaccuracies in MTF, though the locations for comparison are also not optimal (Table 6a). MTF 32 gave the best wave height estimates of the four MTF's, illustrated by the correlation between radar and buoy wave height (Figure A10, Table 6a). However, the cloudiness of the scatter plots indicates the method applied here to find wave height from radar spectra does not give very satisfactory results.
A spatial field of radar inferred wave height with 0.5-1.5m higher waves than SWAN (Figure 6.10) proves the inaccuracy of the MTF as well. The overestimation by the MTF may be an effect of low image energy nearby the shore for which this MTF (AZB32) compensates in particular. The radar wave height found on the ebb shoal ~3.5m was rather high, probably because the radar has difficulties in measuring waves lower 1m.
Appendix A5 compares the 1D (converted) radar and SWAN spectra at the four buoy locations in January to explain the differences in radar and SWAN wave height.

Concluding, the SWAN-radar comparison of wave period, wavelength and wave direction suggested when and where the radar quality was low, radar derived wave height is still too inaccurate to draw on.

6.3 Quality reduction factors

In grid cells with limited wave field quality the image spectrum, from which wave characteristics are obtained, is a poor representation of the actual waves in the computational cube. The two methods filter evaluation and SWAN-radar comparison indicated when and where quality is limited. The qualitatively determined zones are assumed to be related mainly to three quality reduction factors; wave breaking, bottom slope and radar view domain. The tidal stage act on top of all three quality reduction factors.
The zones of limited quality were at the northern edge of the ebb delta, at the western shoal, the south east part of the ebb delta, the east part of the radar view area, along the Terschelling shoreline and in the southern part of the ebb channel.
The spatial extent of the low quality zones increased during low water levels, during storms and during maximum (ebb) tidal currents. The wave field quality during a southwestern wind varied less with the tide than the quality varied during other wave and wind conditions.

Wave breaking

The zones of limited quality on the northern edge of the ebb delta, on the western shoal and along the Terschelling shoreline can be attributed to wave breaking. These low quality zones extended at low tide and during storms.

Wave breaking affects the quality of the image spectra in three ways.

First the radar return signal increases since the backscatter mechanism changes from Bragg scatter on the wind ripples to specular scatter on the white foam. This only affects the wave heights derived from image spectra, because the image intensity maximum is used only to find the corresponding dominant wave characteristics.

Second the image intensity peak shifts to lower frequencies, which effect can be noticed as a high wave period.

Third waves behave non-linear after breaking. The image processing method, based on wave linearity, uses the dispersion relation. Obviously the dispersion shell fitted through the data cloud of non-linear waves does not give reliable wave characteristics.

The wave period and wavelength quality seems to be quite good during low energetic conditions and with a southwestern wind (combined with an ebb tidal current). Those long waves hardly break, so the current and depth might be extracted more accurately from the return signal.

Steep bathymetry

Grid cells with low wave field quality along the sides of the ebb channel and the shoals might arise by their steep bottom slopes.

To find wave information the depth and current estimate were subtracted from the image spectra and a dispersion shell was fitted through the data cloud. Steep bottom slopes may induce poor image spectra, especially in shallow water. In such areas the waves depend strongly on the bathymetry. A single depth and current estimate for the large computational cubes is not found or is not representative for the variable bottom: no single dispersion shell fits through the data cloud of the monitored wave pattern. Quality of wave information at grid cells with high spatial variability is low due to the not (entirely) removed depth effects by the poor depth fit.

Radar view direction

The lower radar wave field quality in the ebb channel, at the eastern part of the radar view area and at the southwest ebb delta may be caused by the limited view domain in which the radar is able to measure waves. This low quality zones extend during a strong ebb tidal current by the wave-current interaction. Sea clutter can hardly be measured when waves

propagate (nearly) normal to the direction in which the radar sends the electromagnetic pulse, especially at far ranges where the azimuthal pixel size increases to 54m. In case of normal propagating waves the wave group seen by the radar as dominant is often in the radar view direction, in which direction backscatter might be overestimated.
Tidal currents interact with the waves and modify their direction. In the ebb channel, south of y=607000m and in the eastern part during maximum ebb current, the wave propagation changes into a direction (nearly) normal to the radar view direction which cannot be monitored by the radar anymore.
At the southwest part of the ebb delta during ebb slack and mid-ebb currents might (*1) bend the southward propagating waves to southeastward propagating waves, which wave direction is hard to monitor by the radar. During low energetic conditions and a southwestern wind radar wave field quality might (*2) be limited. First the lower waves are hard to monitor by the radar. Second, the effect of the ebb current might be more pronounced on the low waves, bending the waves in different directions. Third, the southwestern wind may blow the waves in a more eastern direction, which complicates monitoring in the northern and eastern part of the radar view area.
(*1) Note, the large directional (SWAN-radar) difference at the southeast part of the ebb delta can also be attributed to SWAN as; (1) a dominant direction can deviate easily when energy is distributed only slightly different in a multi-directional (SWAN) wave field or (2) refraction is under- or overestimated.
(*2) Large directional (SWAN-radar) differences during the low energetic conditions and the southwestern wind may also be SWAN induced in case swell was present. Swell or a mixture of swell and wind waves is hard to predict by SWAN, which was developed originally as wind wave model.

6.4 Quality predicted

The quality reduction factors wave breaking, steep bottom slopes and radar view domain are estimated or predicted to find zones of low wave data quality. Radar wave field quality can be asked for in two different ways. First the quality of a coastal area can be *estimated*, imaged by an already placed marine (X-band) radar (radar image based quality). The quality estimate serves as a certain measure of wave data reliability and the image data can be made ready-to-use, eventually as validation data for numerical models. Second the quality of radar images of a coastal area can be *predicted*, which may be imaged by a marine (X-band) radar in future (though a numerical model has to exist; numerical based quality). With this, the optimal location of a radar system can be found beforehand and a predicted poor radar wave data quality may motivate to use a different imaging or measure technique. So, the coastal area is

monitored most accurately and the imaging system is used optimally. Below six methods follow to either estimate (radar-based) or predict (numerical based) the radar wave field quality based on the quality reduction factors: wave breaking, steep bottom slope and radar view width (1) and (2), wave breaking (3) and (4), radar view width (5) and steep bottom slope (6). Method 1, 2 and 3 can only be used when a radar system is already available, so radar image based quality. The fourth and fifth method could be applied when no radar system is available yet, though a numerical model has to exist (numerical based quality). The sixth method can be used when bathymetric information is known. Figure 6.12 shows the dominant wave period at ebb slack (28 January 00:43:03) with five quality predictions (method 3 not shown) of the image.

1. Wave characteristics were still derived from image spectra when no current or depth was found, but their quality will be limited. The status of the radar image shows for each grid cell and sample moment whether current and water depth were extracted from the image spectra during the image pre-processing by Nortek. Wave breaking, steep bottom slopes and a limited radar view can complicate current and depth extraction. Therefore the radar status image might be a good estimator of wave field quality (Figure 6.12).
   To proof the radar status image gives indeed an estimate of wave field quality a time and space analysis of the percentage of good status was done. Figure 6.11 shows a low percentage of good status in the breaking zone and at the eastern part of the radar view area. Over time the percentage of good status decreased during ebb and increased during flood. During the heavy storm at 24 October, the status percentage lowered further.
   A disadvantage of the radar status image method is over qualification of the wave data. The quality of the water depth and current estimate varies, but the radar image status only indicates *if* water depth and current was extracted. Image spectra with poorly extracted water depth and current would not provide high quality wave characteristics.
   Concluding, the radar status image can serve as a raw estimator since it suggests poor wave field quality in the quality reduction zones.

2. The spatial and time trend filter can estimate radar wave field quality, though the filters might have to be retuned in new study areas.
   Note the output of the data filters (in combination with SWAN-radar comparison) was used to find the quality reduction factors, using the filters to predict radar wave field quality appears to be circular reasoning. However the filters can be relied on as a wave quality estimator, when used for individual radar images.

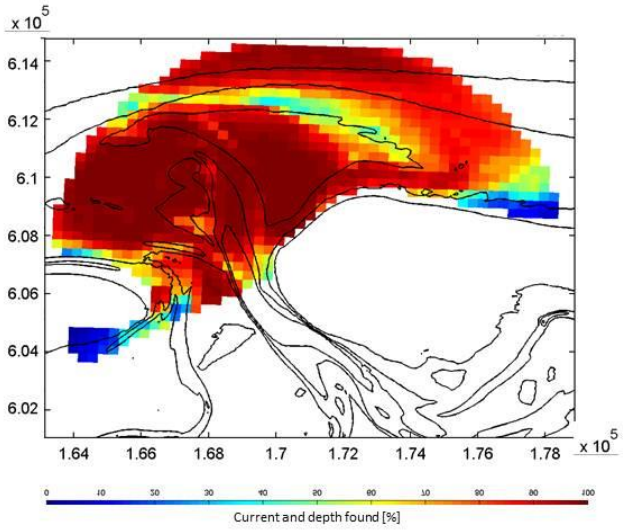

Figure 6.11. The percentage of the October images when current and depth were found. A high percentage can be referred to as good 'status'.

3. White zones of wave breaking could be found by averaging radar snap-shot images over several minutes, similar to the time-exposure Argus video images. Unfortunately this cannot be shown, because radar snap-shot images are not available.

4. SWAN can be used to predict zones of wave breaking. The relative wave height $H_{rel} = \frac{H_{sig}}{d}$ and the breaker fraction Q_b (defined by Battjes and Jansen in SWAN tech. documentation) are model output parameters which can be used to predict wave breaking. Here the relative wave height is chosen. A threshold value above which poor radar wave field quality can be expected follows from relating the relative wave height to removed outliers (Q_{filt}). The average of H_{rel} at the five SWAN runs of January is 0.32 at the grid cells with removed wave period outliers (T_{filt}). A slightly higher relative wave height threshold of 0.4 is used as wave field quality predictor, since outliers do not only arise due to the quality reduction factor wave breaking.
   This 'Ameland' H_{rel} threshold could be used in similar coastal areas to predict low radar wave field quality due to wave breaking. A similarly derived relative wave height threshold in different study areas should yield more confidence and a wider applicability of the 'Ameland' threshold values.

5. Wave field quality can be predicted by the absolute difference angle $\Delta\vartheta$ between radar view direction ϑ_{view} and the (modelled) wave propagation direction ϑ_{dom}. A plot of the difference angle $\Delta\vartheta$ suggests the radar can monitor waves which are up to 60 degrees differently directed from the radar view direction. This value can be calibrated by relating

the difference angle $\Delta\vartheta$ to the number of (wave period) outliers T_{filt}.

6. Limited quality due to steep bottom slopes can be predicted when the bathymetry is known. A slope map derived from the bottom elevation map, indicates the trouble zones with steep slopes and thereby the low quality zones.

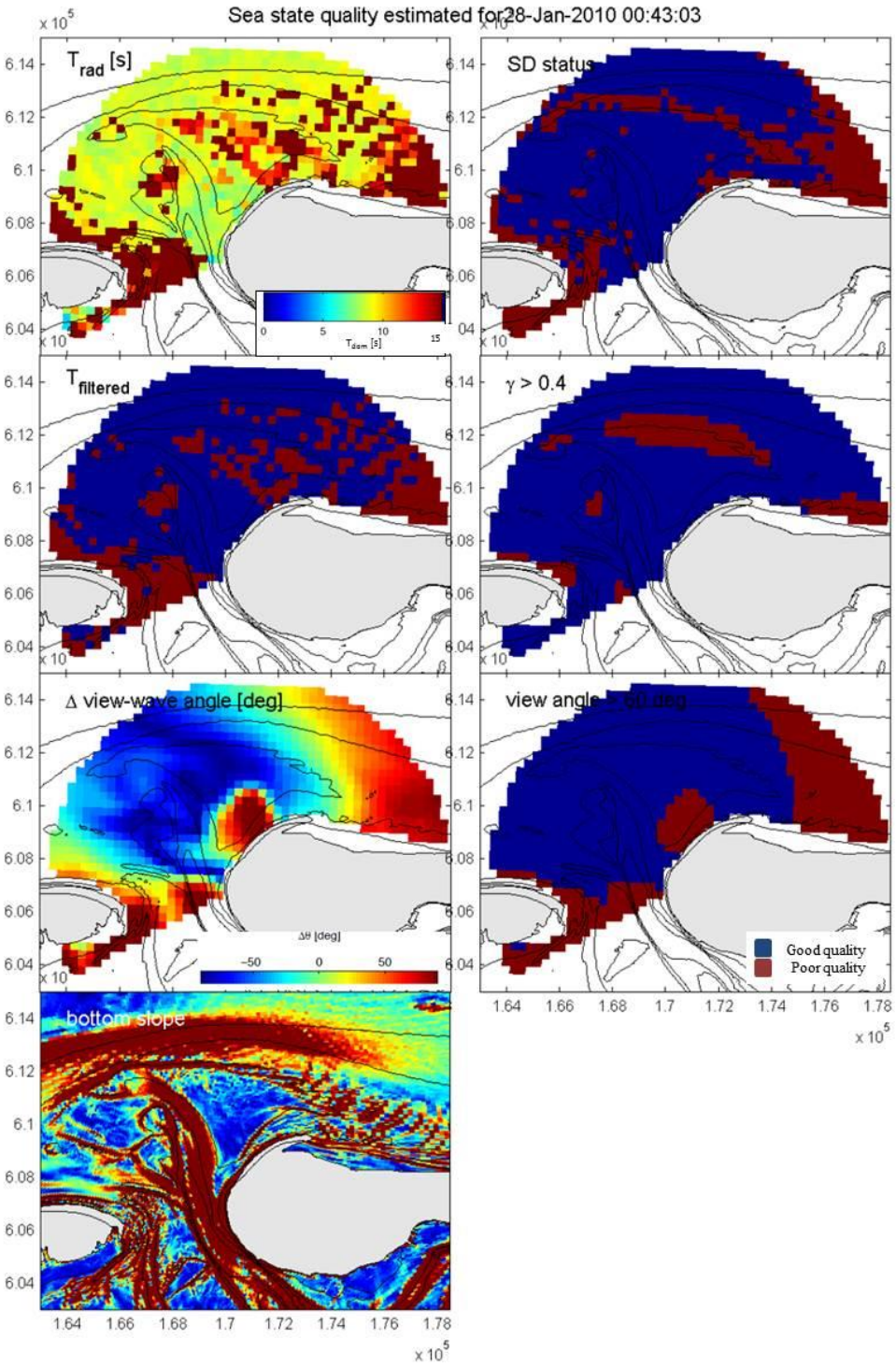

Figure 6.12. Quality of the dominant wave period image at ebb slack at 28 January is given by estimating or predicting: good status, outliers by filtering, threshold (H/h=0.4) in relative wave height (wave breaking), radar view angle with respect to wave direction (threshold 60°) and bottom slope.

7. Discussion

Low frequent energy penetration

Deltares indicated wave propagation in SWAN should be improved, which aim is part of the objective to improve the simulation models used to derive the Hydraulic Loads for primary sea or flood defense safety prediction in the SBW-HR framework ('Strength and Loading of Water Defences- Hydraulic Loads') 2011-2016. So far, low frequent energy penetration into the Wadden Sea is a lack in the SWAN model of the Ameland Inlet (Gautier and Arab, 2011). Low frequent energy penetration was improved by bottom friction dissipation reduction as well as (artificial) refraction reduction (Van Dongeren et al., 2009). Gautier and Arab (2011) studied the effects of diffraction in the Ameland Inlet using SWAN and the diffraction model PHAROS and proved diffraction was of minor importance at this study site. They observed waves refract out of the channel and focus on to the shoals in both the SWAN and PHAROS model.

The lack of low frequent energy penetration into the Wadden Sea was also observed in this study as the mismatch of the SWAN and buoy energy peaks in the wave spectra in the ebb channel (Figure A11). The sensitivity analysis in Appendix A4 inspired to study the effect of Triads. SWAN overestimated the high frequent peak (at the channel buoys AZB 21 and AZB 32) when using default settings, while this peak was removed entirely when excluding Triad wave-wave interactions (Figure A11). The buoys measured a moderate high frequent peak. To obtain a similar peak in SWAN's spectra the effect of Triad input was evaluated by varying the proportionality coefficient α_{EB}. Unfortunately, varying this parameter did not result in a better fit of the 1D SWAN spectra to the buoy spectra (Figure 7.1).

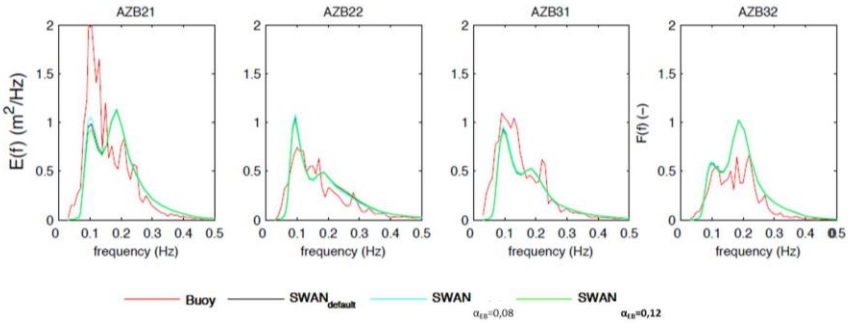

Figure 7.1. Varying the proportionality coefficient α_{EB} from 0.1 (default, black) to 0.08 (cyan) or 0.12 (green) did not result in a better fit to the buoy spectrum (red).

Similar overestimations of the high frequent peak were observed by a hindcast from 1982 of the Haringvliet and from 1995 of the Norderneyer Seegat (Ris et al., 1999, Figure 7.2). They found equally wind and triad wave-wave interactions might have transferred too much energy to these high frequencies.

Moreover, Booij et al. (1999) varied the proportionality coefficient (α_{EB}=0.125, α_{EB}=0.25 and α_{EB}=0.5) and concluded the coefficient can tune the low frequent peak, but has no effect on the high frequent peak. They suggested the second peak in the spectrum has reached an equilibrium in the Lumped Triad Approximation (LTA) for wave-wave interactions. Perhaps, the LTA (Eldeberky, 1996 in Booij et al., 1999), to estimate Triads, is too much schematized to predict wave interference correctly in this complex bathymetry. The LTA predicts interference of waves in shallow water, resulting in energy transfer to higher frequencies. However in deeper water (such as the ebb channel), energy is not transferred back to lower frequencies by the LTA.

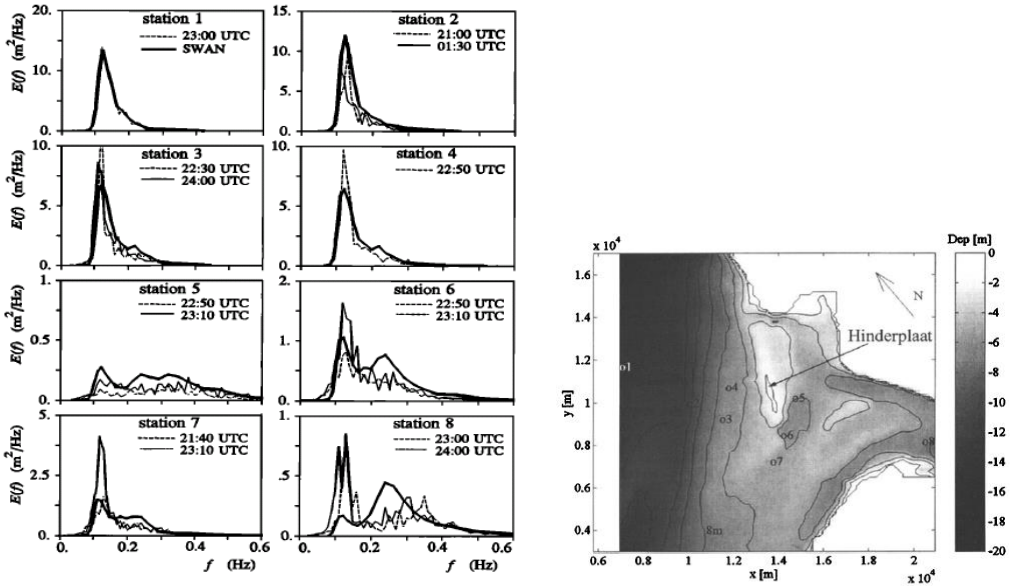

Figure 7.2 (Ris et al., 1999).1D observed and computed spectra (left) for the eight buoy locations in the Haringvliet (right) for 14 October 1982

Wave height and MTF

The wave heights derived from radar image spectra using an MTF were not satisfying when comparing radar to buoy or SWAN wave height (Figure 6.10, Table 6a). The MTF and wave height are evaluated below, followed by an alternative to estimate wave height.

The wave period filter used as indicator for poor quality image spectra in the image spectra time series was not optimal.

- The locations of spectra acquisition did not correspond exactly to the wave period sample locations and the temporal resolution of the image spectra time series was three times smaller than for the wave period time series.
- Only image spectra were removed when the corresponding wave period was an outlier. So, spectra were removed when the spectral peak shifted over the frequency axis and the peak did no longer represent waves. Image spectra should be removed also when their

peak showed *intensities* that do not represent waves. For example spectra should be removed when the image intensity was overestimated due to a roughened sea surface by strong currents.

The MTF should correct the image spectra for different image intensity. The image intensity and its distribution over the frequency axis might differ per location (over the range (range, shadowing and tilt) or the azimuth) and over time (storm intensity, wind direction, current direction or water level). Here the MTF is a strong simplification: spatial variations were neglected, temporal variations (165, 65 and 136 grey lines in A8) were leveled out by averaging the individual 30minutes MTFs over the several conditions. The MTF does depend on frequency, correcting for each frequency the under- or overestimated image intensity.

Instead of using the raw average of all 30minutes MTFs a trend line through the average can also be chosen as MTF, since here the MTF was already simplified thoroughly. Nieto Borge et al. (2004) found an MTF as the ratio of 1D wave number spectra, finally they used the trend (-1.2) through their wave number dependent MTF ($k^{-1.2}$) to transfer image spectra in wave spectra.

To derive wave height using the MTF, again accurate filtering of the spectra is important. The power shape of the MTF converts image spectra with peaks at low- frequencies to reliable image spectra with peaks in the mid-frequencies. For example, this can be noticed for spectra at AZB 31 (Figure A9). Probably the raw image spectrum with the low frequent peak did not represent waves and is thus converted incorrectly by the MTF to a reliable wave spectrum.

Since the image spectra modulate temporally or spatially under variable conditions, a proper MTF should depend on those conditions.

Wave height can also be approached differently. Nieto Borge et al. (2004) mentioned wave roughness or the quantity of image intensity is not directly related to wave height. Swell waves can reach large heights, though wind speed, wind ripples and thus image intensity will not be abundant. Nieto Borge et al. (2004) used the signal-to-noise-ratio (SNR) to estimate wave height. The square of this ratio is linearly related to wave height, found by Alpers and Hasselman (1982, in Nieto Borge et al., 2004) who estimated wave height in spaceborne Synthetic Aperture Radar images. The signal (S) is the measured energy in the spectrum due to waves. The noise (N) is the remaining background energy, including wind related speckle (Nieto Borge et al., 2008). Calibration coefficients for the SNR are needed to determine an accurate wave height. The difficulty of this method is to distinguish noise and signal clearly for extracting wave heights successfully.

Quality reduction factors

Next to the predicted quality reduction factors wave breaking, steep bottom slopes and a limited radar view angle, also heavy rain, a current perpendicular to wave propagation, unidirectional waves and strong currents reduce the radar wave field quality reasonably. Those factors can be predicted also.

1 Heavy rain roughens the sea surface whereby the intensity of the backscatter increases and wave patterns get difficult to distinguish. During rain storms Wyatt et al. (2003) observed inaccuracies in WaMoS measurements. In our data set, heavy rain may explain the lower radar quality (especially wave period and wavelength) at 20 and 24 October since heavy storms are often involved with rain storms. Although the radar system requires a minimal wind speed for monitoring wind ripples, too heavy weather might give incorrect spectra or incorrect wave field parameters due to rain storms distorting the radar images.

   Low quality radar images due to rain storms can be estimated either after or prior to radar monitoring. After monitoring the radar image grid points should be excluded where the standard deviation of the corresponding radar computational cube is high due to rain storm distortion. Prior to monitoring, success of the radar can be predicted using weather forecasts. When the image processing techniques are developed further, grid points or entire wave fields distorted by heavy rain storms might be removed beforehand.

2 Waves and currents are hard to monitor when the current is perpendicular directed to the wave propagation direction. Then the waves do not deform by the current, so a dispersion shell fitted through the data points will contain no current deformation. Thus, the iteratively determined current and depth estimate by a non-linear fit on the data points will be inaccurate. The wave spectrum will be contaminated by current and depth information as consequence, since those were only poorly extracted.

3 Nearly unidirectional waves or waves with little directional spreading are hard to monitor by a radar system. No dispersion shell can be fitted through the data points, since those data points are closely distributed in the directional wave number domain. Current or water depth cannot be extracted, resulting in poor estimates of the wave field. Zones of unidirectional waves may be predicted by mapping shallow water or by estimating wave breaking, because most of the waves refract to one direction in shallow water and the rough breaking zone may return high backscatter dominating the radar image in the direction of the breaking waves.

4 Strong currents roughen the sea surface and intensify the backscatter signal. The radar overestimates image intensity, while current, depth, wave period, wavelength and wave direction can still be extracted accurately. Wave height derived from image spectra could be overestimated in zones with strong currents.

The MTF is based on spectra at channel buoy AZB 32, exposed to currents, and thus the MTF should automatically neutralize the overestimated image intensity in the channel. However, the filter selected spectra during slack tide in particular. Concluding, the MTF may be only slightly too low, since it is based on spectra imaged in the ebb channel though based on slack tide spectra in particular. Wave height in absence of currents might be underestimated by the MTF, while wave height still might be overestimated in zones with strong currents. Unfortunately, the spatial field of wave height (Figure 6.10) does not show these outlined over- or underestimations very clearly.

Quality predictor

Low radar wave field quality due to steep bottom slopes, non-linear waves and unidirectional waves is caused by poor depth or current extractions. Therefore, a first indication of a poor radar inferred wave field estimate can follow from a map of current multiplied to depth. The quality reduction factors radar view angle and heavy rain storms may be partially predicted by the current-depth map, since those quality reduction factors hinder to derive good characteristics from the radar images at all (wave field, current, depth).

Quality predictor for currents

Besides improving the quality predictor for waves, the quality of the extracted current and depth is asked for. Inversely, poor depth and current quality result in low wave field quality. Most of the poor wave field quality predicted zones and moments seem to apply also for currents, when the quality reduction factors are evaluated whereon the quality predictions are based.

- Non-linearity of waves due to wave breaking results in computational cubes of sea clutter images whereon the dispersion does not fit. The non-linear fit to extract current and depth yields deviating results.
- A single depth and current estimate is not representative for computational cubes with steep bottom slopes.
- Outside the limited radar view angle sea clutter cannot be monitored optimally. Neither wave characteristics nor current (nor depth) will be a good estimate when the imaged sea clutter is not representative.
- The abovementioned quality reduction factors heavy rain, unidirectional waves or a perpendicular current can be applied as current quality predictor similarly. The simple depth-current map quality indicator can be applied for those three quality reduction factors.

8. Conclusions

Corresponding zones and conditions of low radar quality followed from (1) evaluating the wave field outlier filters and (2) comparing SWAN and radar wave characteristics. Radar wave quality was low at the (edges of the) shoals, along the shoreline and in the southern (y<608000m) and eastern (x>174000) part of the radar image. These zones extended during ebb current and were smallest during mid-flood. Wave field quality increased during storms when the rough sea surface is easier to monitor by the radar. Low quality during severe storms can be explained by heavy rain, distorting the radar image and hindering to find wave characteristics of good quality.

Radar wave field quality can be estimated (after monitoring) or predicted (before monitoring) by the three quality reduction factors wave breaking, steep bottom slopes and limited radar view angle.

- Low quality at the northern edge of the ebb delta, at the western shoal and along the Terschelling shoreline can be attributed to wave breaking. The radar image intensity increased suddenly by a change of backscatter mechanism due to the white foam of wave breaking. Wave height derived from image intensity spectra got overrated. Also non-linearity of the waves in the breaking zone frustrated the data processing method, based on wave linearity, resulting in outliers of the wave characteristics.
- Low quality at the edges of the shoals and along the ebb channel can be explained by steep bottom slopes. A single current or depth estimate from a computational cell of 960x960m is not representative for steep bottom slopes. Subsequently derived wave field characteristics are not accurate. The reduction factor is more significant during a low water level when more waves interact with the bottom.
- (nearly) Normal incident waves cannot be seen by the radar, reflected by the low quality in the southern and eastern part of the radar image especially. During ebb current these low quality zones extend. Due to wave-current interaction wave direction changes and more waves appear to propagate normal to the radar view direction.

A limited radar view angle seems to be the most important quality reduction factor (Figure 6.12).

Six methods, based on the three quality reduction factors, were developed to estimate or predict radar wave field quality. The best of the six quality predictors computes the difference between modelled wave direction and radar view direction. Zones where wave direction is ±60 degrees different from the radar view direction are allocated as low quality.

Wave height derived from image spectra was overestimated because the image spectra filter was insufficient and the MTF was based on poor radar spectra from a channel buoy.

When being confident with the radar quality predictor(s), low wave field quality may be predicted and the qualitatively good wave field characteristics may validate model results.

Methodological research questions

The research steps (question 5-11, Section 3) on which the research and the main conclusion are based are answered below.

5 *How can the radar inferred wave field be filtered? And what do the wave fields look like after filtering?*

The radar wave field characteristics were successfully filtered for outliers using subsequently a spatial based filter and a linear time-trend based filter.

The spatial filter removed wave periods and wavelengths at grid points which differed more than 3s or 35m from the median of the corresponding wave period or wavelength (spatial) field. (coming from) Wave direction between 30 and 225 degrees were removed, since wave direction varied too much to apply a spatial median filter.

The time-trend filter removed wave periods, wavelengths or wave angles which deviated more than respectively 2, 2 or 3 times the standard deviation from the linear trend over time at each grid point. The trends over time were determined over smaller time spans, based on: tidal period for the wavelength and wave direction and off-shore wave forcing for the wave period time series. Whether the off-shore wave forcing or the tidal period was used as time span indicator was based on the strongest dependency of the wave period, wavelength or wave direction signal. The standard deviations as filter criteria were fixed on 2.5 and 3s, 20 and 25m and 25 and 30 degrees to keep the filter effectively.

Image spectra were removed when also wave period was filtered out at that moment and grid point.

Filtered wave field characteristics have a lower standard deviation since their outliers were removed.

6 *How do radar inferred wave period, wave length, wave angle and image spectra change from the radar measurements offshore boundary, over the ebb tidal delta and into the ebb channel, during a storm?*

Waves refracted onto the shoals and shortened in length, wave period increased slightly in the channel. Western incident waves crossed the channel and partially bent into the inlet or onto the southwestern tip of the ebb delta. Waves changed in direction at the eastern point of the ebb delta, where they interacted with the tidal current. Wavelength grew during high tide and decreased during low tide. Wave period and image intensity increased during storms.

7 *Where and when do the radar derived wave fields show outliers over the Ameland ebb delta study area?*

Outliers were noticed at the northern edge of the ebb delta, around the shoreline of Terschelling, in the southern ebb channel and in the eastern part of the radar view area. The amount of outliers increased during lowering tide or heavy storms.

8 What is the empirical based Modulation Transfer Function?

Four MTFs followed from averaging several ratios of 30min averages of the buoy spectra and filtered image spectra in January, determined for the four inlet buoy locations separately. The MTF at location AZB 32, based on 136 30min buoy-radar spectra ratios, was selected as the most appropriate MTF to apply generally to convert the image spectra to wave spectra. This MTF was selected because this transfer function is based on sufficient 30min spectra ratios and its increase to inconvenient high values at low and high frequencies is limited. To exclude the inconvenient high values in the MTF, the MTF was cut off at 0.05Hz and 0.3Hz. The trend line through MTF 32 suggests the relation $f^{1.3}$.

9 What does the radar image spectra derived wave height look like?

The wave height extracted from the transferred radar image spectra, was generally overestimated and shows little correspondence to buoy or SWAN wave height. The overestimation can be explained by inaccuracies in MTF, though the locations for comparison to buoy wave height are also not optimal.

10 What do the SWAN dominant wave fields look like?

SWAN wave period, wave length and wave direction are similar to the corresponding filtered radar wave characteristics. Differently SWAN predicted a low wave period in the ebb channel, waves following the ebb channel and waves entering from the west on the southwest tip of the ebb tidal delta. The bimodal SWAN spectra might explain the different SWAN and radar dominant wave field in the ebb channel and on the southwest tip of the ebb delta.

11 Which hydrodynamic processes are under- or overestimated in SWAN?

The sensitivity of SWAN was tested for five runs in January by excluding wind, currents and triad wave-wave interactions. The main objective was to find a better fit of the overestimated high frequency peak in the SWAN spectra on the moderate high frequency peak in the (channel) buoy spectra and thereby to improve the corresponding wave period decrease in the ebb channel. The overestimated second harmonic could be attributed to triads since the peak was removed when triads were excluded, in contrast to SWAN runs without wind or currents. The triad effects could not be smoothed by varying the triad proportionality coefficient. Therefore, SWAN was run with default settings for SWAN-radar comparison, since excluding triads seems not realistic.

Recommendations

Radar data need to be collected under more various storm conditions to get familiar with the capacity of the radar as wave monitoring instrument. For example there is no certainty about the radar quality during wind from the southwest. SWAN contradicts radar inferred wave period, wavelength and wave direction. Radar inferred wave period contradicts radar wave direction also regarding the zones of outliers.
The additional quality reduction factors in Section 7 need to be tested.
The new quality predictor need to be tested, which is based on current multiplied with depth (Section 7).

The MTF can be improved or recomputed when time series of in-situ wave spectra would be available at locations without strong currents, outside breaking zones, with no high variable bottom and within an appropriate radar view angle.
The MTF and radar inferred wave height will improve when the image spectra filter is designed as the wave period and wavelength filter. Image spectra should be removed when they are outside a boundary around the average image spectrum, which boundary needs to be based on standard deviations of the image spectra.

Peak radar wave characteristics are preferred above dominant radar wave characteristics. In bimodal spectra the ‘dominant’ is more sensitive to small differences in the energy distribution over the frequency axis of the spectrum. Moreover the ‘peak’ is a common statistic when studying waves.

The buoy spectrum indicates that a process in the ebb channel amplifies the high frequent peak in the bimodal energy spectrum. Processes affecting the energy distribution need to be studied more thoroughly.

Appendices

A1 Preliminary analysis of radar wave characteristics and image spectra

Wave period

Average wave period was rather uniform over the radar view area, except the outliers in wave period around the northern edge of the ebb delta, at the western shoal, east of x=176000m and south of y= 608000m. The high time-averages (Figure A1) in the zones mentioned above, suggest outliers arose around the same zones every sample moment. The longer October storm with more diverse weather conditions (compared to January) gave a higher variability in wave period, which is reflected by a higher standard deviation. Wave period was ~10s in January and a few seconds higher in October. Wave period is related to wave forcing with higher (lower) wave periods found during storms (calm weather). The tidal signal in the wave period average (Figure A2) suggests the number of outliers increased (decreased) during lowering (rising) tide, since wave period itself is not strongly related to tide.

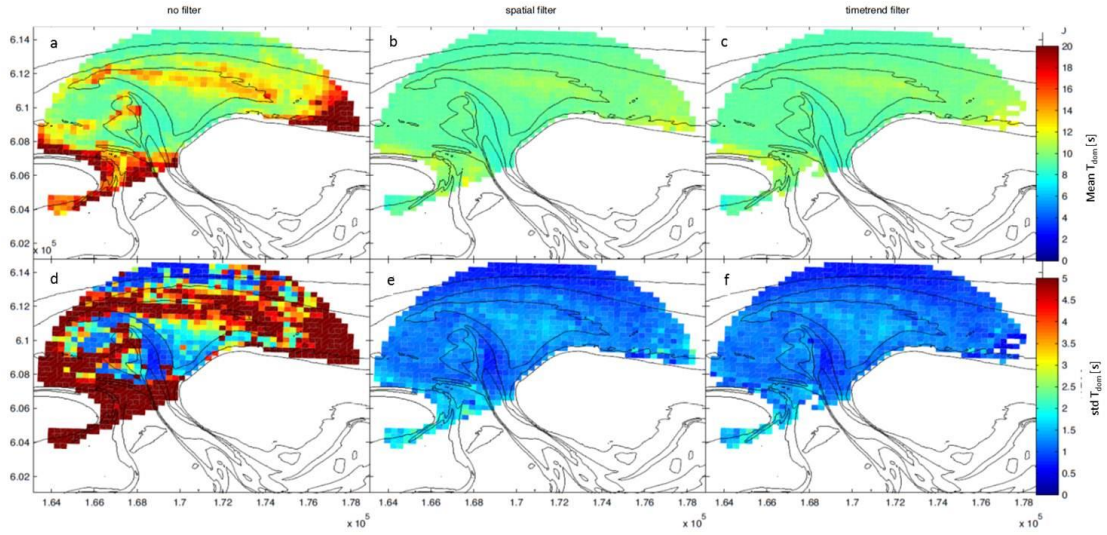

Figure A1. Dominant wave period averaged over time (27th and 28th of January) for each grid point (a-c). The reddish colours show up where outliers were abundant. The standard deviation (d-f) reflects the outliers as well.

Wavelength

Dominant wavelength decreased (increased) above the shoals (deeper water) according to the dispersion relation (eq.2) (Figure A3). Wavelength should increase during rising tide and decrease during lowering tide, though no tidal signal can be observed yet since outliers are still incorporated (Figure A2). Both the spatial pattern of wavelength outliers (Figure A3a) and the temporal variation of outliers (Figure A2) are similar to the variability in wave period outliers (Figure A1a, Figure A2). Again a high standard deviation suggests outliers were present.

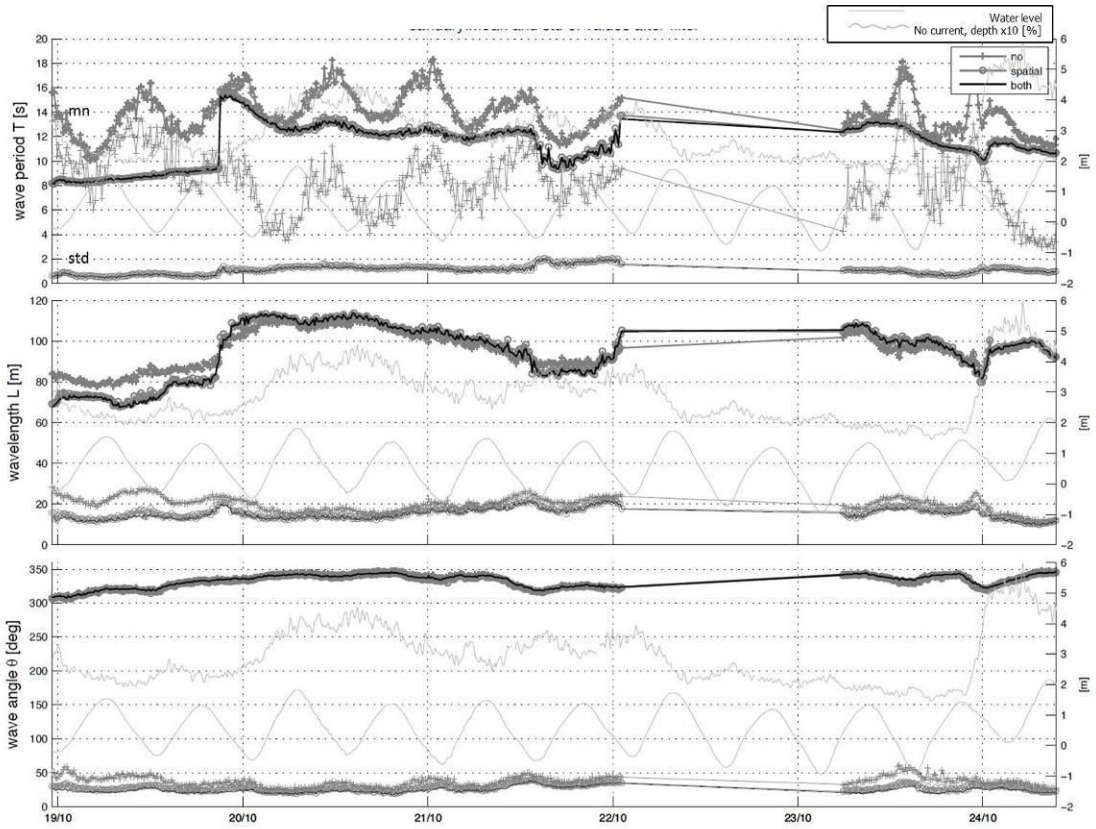

Figure A2. Dominant wave period (top), wavelength (middle) and wave direction (bottom) from 19 to 24 October 2010. For each wave characteristic the time average (upper lines) and standard deviation (lower lines) per image are shown before filtering, after applying the spatial filter and after applying the time-trend filter. The right axis shows the water level and the percentage (x10) of the grid points per image where no current and depth was found.

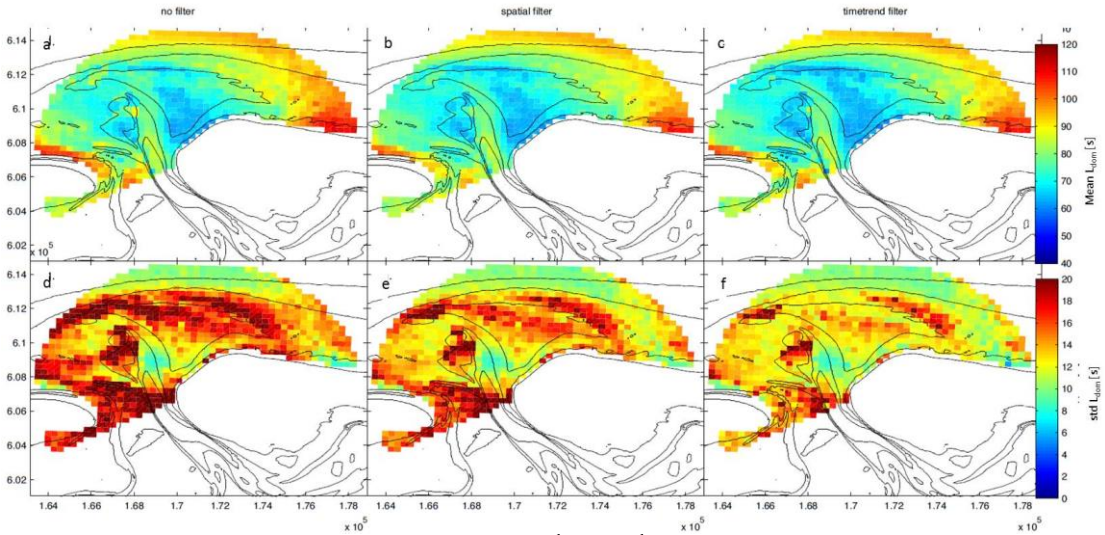

Figure A3. Dominant wavelength averaged over time (27th and 28th of January) for each grid point (a-c). The reddish colours show up where outliers were abundant. The standard deviation (d-f) reflects the outliers as well.

Wave direction

Generally the waves entered from the northwest, refracted onto the shoals and propagated to the south and the east on respectively the large ebb shoal and the western shoal (Figure A4). Waves entered more northerly during storms, while they entered from different directions when the wind was from the southwest. Wave direction varied with time by wave-(tidal) current interaction and due to the amount of outliers (Figure A2). Similar to wave period and wavelength, wave direction had a higher variability during the October storm than during the January storm, which was explained by the higher variety of wave and weather conditions during the longer time series of October.

Less outliers were observed in wave direction than in wavelength or wave period and outliers were more scattered over the radar image. New outliers were found at the southern point of the ebb delta ([171000,609000]) and in the eastern channel along the Ameland shoreline ([172000, 610000]). Similar to wave period and wavelength outliers, the amount of outliers increased during lowering tide and decreased during rising tide, observed from visually analyzing the wave direction time series.

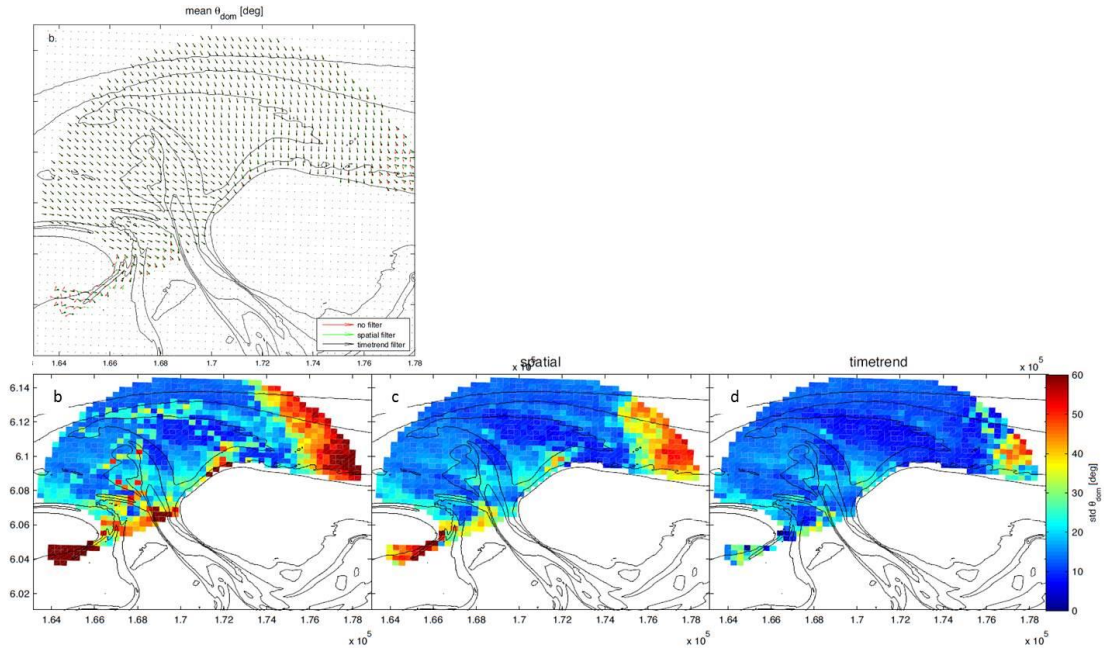

Figure A4. Average dominant wave direction (a) for (27 and 28) January before filtering (red), after applying the spatial filter (green) and after the time-trend filter (black). The standard deviation before (b) and after filtering (c, d) for January shows outliers were found and filtered out in the southern and eastern part of the radar image and around the shoals.

Image spectra analysis

Towards the shore the image energy decreased and above the shoals the peak frequency shifted to lower frequencies, waves refracted out of the ebb channel and toward the shoals, whereby the image intensity spread over the directional and frequency ranges.
The temporal variability in image intensity, position of the peak frequency and the distribution of image intensity over the frequency axis can be noticed from the image intensity time-stacks at the buoy locations (Figure A5). Three conditions were observed, explaining the temporal variability in image spectra: storm intensity, tide and wind direction.

- During storms the radar image intensity increased due to an increase of wind ripples at all buoy locations, particularly at the delta buoys AZB 21 and AZB 22 in October. The image intensity spread over a wider frequency range due to more wind waves. Wave breaking might initiate a change of Bragg scatter on the wind ripples into specular scatter on the white foam, showing up as a high image intensity (AZB 22). Wave non-linearity (by wave breaking) might have shifted the image intensity peak to a rather low frequency (AZB 31 in January, AZB 21 and AZB 22 at 20 and 24 October).
- The peak frequency appears to be related to the tide. The peak shifts respectively to a higher or lower position by a flood or ebb current, the image intensity distributed over the frequency range during a flood current, particularly notable for AZB 22 from 21st of October.
- The spreading of image intensity over the frequency axis is related to wind speed and wind direction.

  Waves from the north(west) have a large fetch and image intensity was distributed over the frequency axis, especially during a high wind speed (24 October). During a southwest wind direction (23 October) the image intensity peak was narrow and the frequency is slightly lower than during the storms from the north(west) (for buoy location AZB 21). Swell waves may occur since the fetch for waves from the southwest is only small.

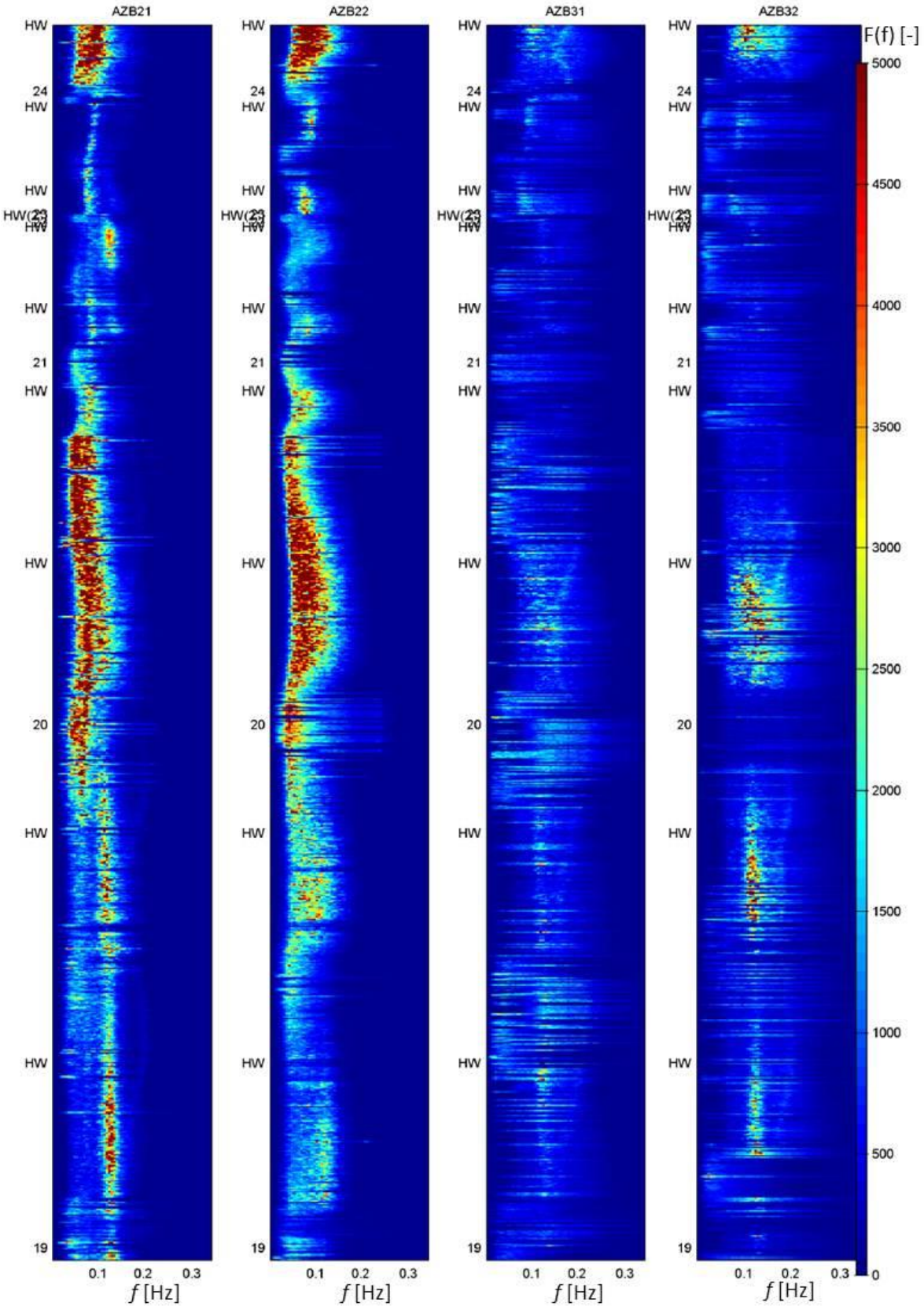

Figure A5 Radar image intensity per frequency from 19 to 24 October, at the four inlet buoys AZB 21, AZB 22, AZB 31 and AZB 32. The timestacks show the temporal variability in the image spectra due to change in wave forcing, water level and wind direction. The time axis (y) is not linear, because hardly any data was saved by the radar system on the low(er) energetic days (22 and 23 October). High tide is indicated as *HW* to help to distinguish the time dependency of the image spectra.

A2 Filter performance

Wave period

Wave period was filtered sufficiently for outliers to yield a representative wave period spatial and time average to study how the wave period looks like, respectively over time (Figure A2) and spatially (Figure A1b-c). The reduced standard deviation (Figure A1f, Figure A2) proves indeed outliers caused the high wave period variability and contaminated the spatial and time average of wave period. Indirectly the reduced standard deviation indicates when and where outliers were abundant. Filter performance seems to vary with time due to storm intensity, wind direction and current direction.

The wave period filters failed during low energetic conditions combined with a southwestern wind and during high energetic conditions, because the corresponding radar images contain one cluster of high wave periods and one smaller cluster of low wave periods (Figure A6). The spatial filter assumed a single spatial median can represent a wave period field and wave periods can be referred to as outlier when deviating with a certain threshold from a single median. Therefore the spatial averages (Figure A2) do not represent wave period fields with two value clusters clearly.

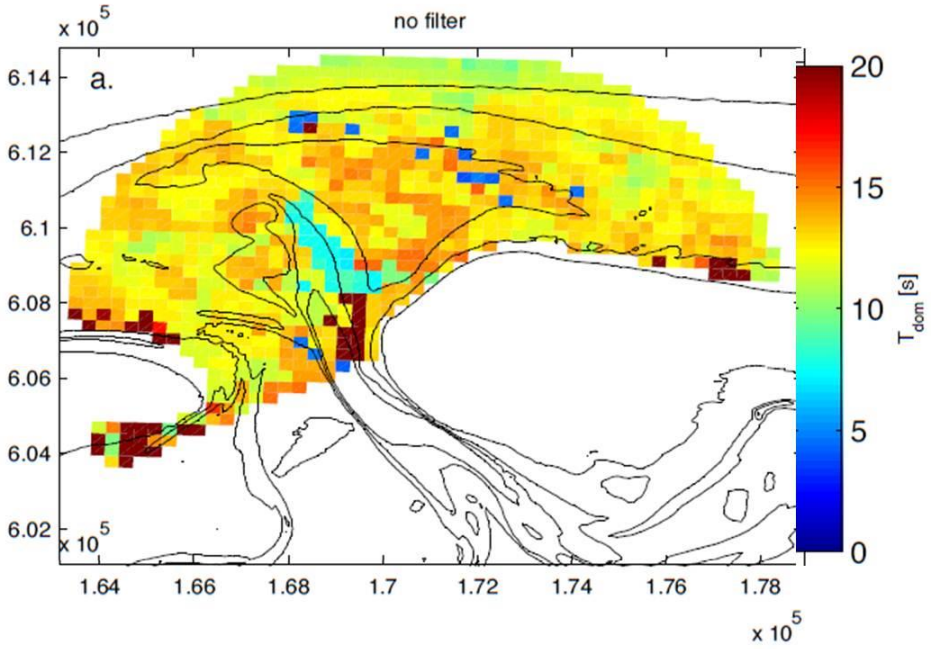

Figure A6. An example of a radar image holding two clusters from 23 October 07:45:52 UTC, mid flood and a southwestern wind. The wave period was approximately 12s, but decreased abruptly in the ebb channel to ~8s.The spatial filter removed the low value cluster.

Wavelength

The wavelength filters functioned not that well compared to the wave period filters (especially in October); the average wavelength did not change much and the standard deviation reduced only slightly after filtering (Figure A2, Figure A3).

Dominant wavelength derived from small computational cells of 960x960m (January and 24 October) showed wavelength clearly and was filtered better than wavelength computed on four times larger computational cells (for 19-23 October). Dominant wavelength from such large computational cells is not representative, since wavelength varies significantly with the water depth (eq. 2). Wave period suffered not that much by the large spatial computational cells, since it varies only significantly with time.

Wave direction

The wave direction filter functioned well, reflected by the reduced standard deviation after filtering (Figure A4c-d). The average wave direction did not change much, since wave direction had only a few outliers (Figure A4a).

The time-trend filter failed where wave direction changed significantly during a tidal cycle. Filter failure was in the areas where waves interacted with currents; channel east of the ebb delta ([172000, 610000]), southeast ebb delta ([171000,609000]) and in the ebb channel ([169000,608000]). Filter failure can happen also where waves can hardly be monitored: eastern part of the radar image and south of y=607000m. The time-trend filter might have failed less for wave period and wavelength in these zones, because their spatial filter with the image specific spatial median removed most of the outliers before executing the time-trend filter. The (image unspecific) spatial wave direction filter only removed extraordinary directions; incident from the east (>30) or south(<225).

Image spectra

Many image spectra of the January and October time series were removed by the filter. Wave period was filtered out often at the four buoy locations, so were the image spectra. Even no image spectra were selected for AZB 31 in January. The image spectra filter failed because time resolution, grid point and size of the computational cells did not correspond for wave period and image spectra time series. A filter based on the standard deviation and a time-average of the image spectra themselves might help. Figure 6.10 indicates image spectra were selected or removed incorrectly when comparing radar to SWAN wave height.

A3 Discussion of the MTF

Figure A7 shows the 30min averaged spectra measured by radar (black) and buoy (gray). The final MTF (Figure A8, blue line) at AZB 21 holds 165 (30min averaged) MTF's (grey lines), based on averaged 6 radar spectra and 3 buoy spectra. The MTF at AZB 22 and AZB 32 hold respectively 65 and 136 MTF's, both based on generally 5 radar spectra and 3 buoy spectra. The wave period was filtered out at (at least) one of the four grid points surrounding AZB 31, for all wave characteristic sample moments in January. Therefore no MTF was computed at this buoy location.

Shape of the MTF

The shape of the MTF's suggests the image spectra are related to wave spectra by a power function as f^b with b=~1.3..4.6, shown in Figure A8 at the log-log axes by the linear trend (green) through the MTF. Nieto Borge et al. (2004) found a power function k^b with b=~-1.2 for the MTF, derived from 1D wave number spectra.

Perhaps the bulb in MTF 32 (around 0.1Hz) arose by the low radar image intensity at the concerned frequency, which is also shown in the selected 30min averages of AZB32 (Figure A7). The higher factor of the MTF should raise the image intensity in the radar spectra at this frequency. MTF 32 increases suddenly below a frequency of 0.05Hz. MTF 21 and MTF 22 increase drastically above a frequency of respectively 0.2 and 0.17Hz. MTF 32 shows such an increase above a frequency of 0.3Hz only. Figure A7 explains these differences in power; the radar spectra contain hardly any energy at frequencies below 0.05Hz compared to the corresponding buoy spectra (particularly at AZB 32) and above 0.2Hz (at AZB 21 and AZB 22), the radar and buoy spectra at AZB 32 are more similar also in high frequencies.

The MTFs increase to inconvenient high values due to the limited (wind) energy in the high frequent part of the radar spectrum. Thereby, image spectra, which do contain energy in higher frequencies, will be raised at these frequencies to incorrect high energies due to the high MTF above ~0.2Hz.

The MTFs were optimized by cutting off the functions at the abovementioned frequencies, where the MTFs start to increase rapidly. MTF 21 was cut off at 0.05Hz and 0.2Hz, MTF 22 at 0.05Hz and 0.17Hz and MTF 32 at 0.3Hz (Figure A8).

Finally, the MTF for AZB 32 was chosen to use as generally applicable transfer function here to estimate wave height for the filtered image spectra. MTF 22 was based on very few image spectra; therefore MTF 21 and MTF 32 would be more representative for wave height estimation. MTF 21 and MTF 32 do not differ much statistically (Table 6b), but the image spectra were transferred to wave spectra by using only the mid-frequencies from 0.05-0.20Hz at AZB 21, while a wider frequency range from 0.05-0.30Hz could be used for AZB32.

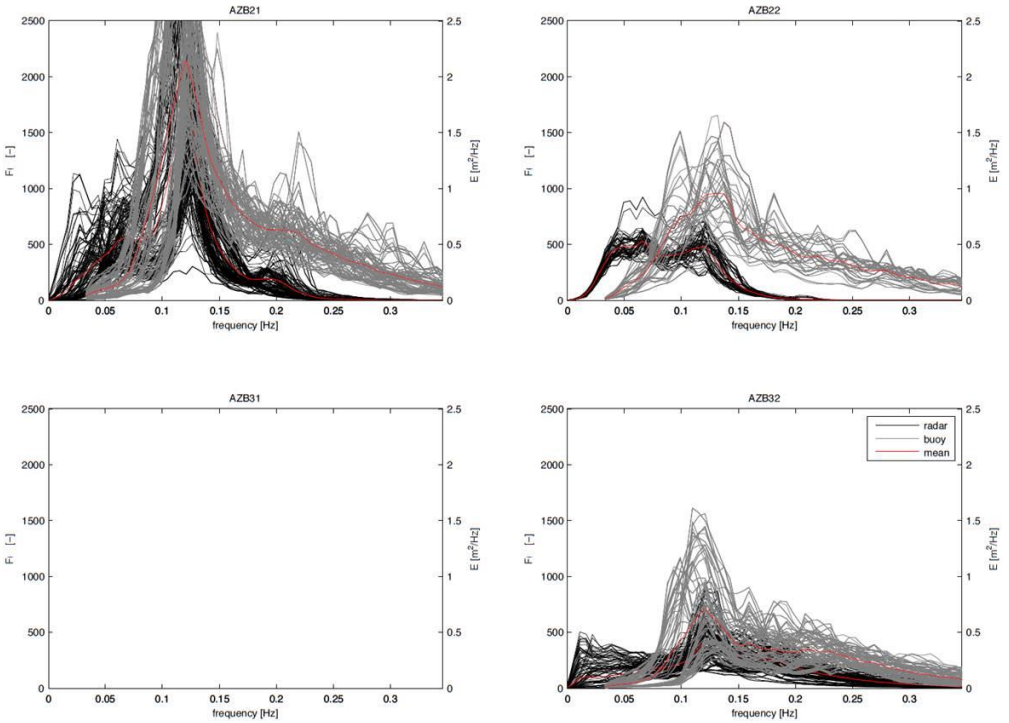

Figure A7. The 30min averages of radar image (black) and buoy wave (grey) spectra, with their mean (red) show the spectra are similar, particularly at AZB32. At AZB31all radar spectra were removed by the image spectra filter.

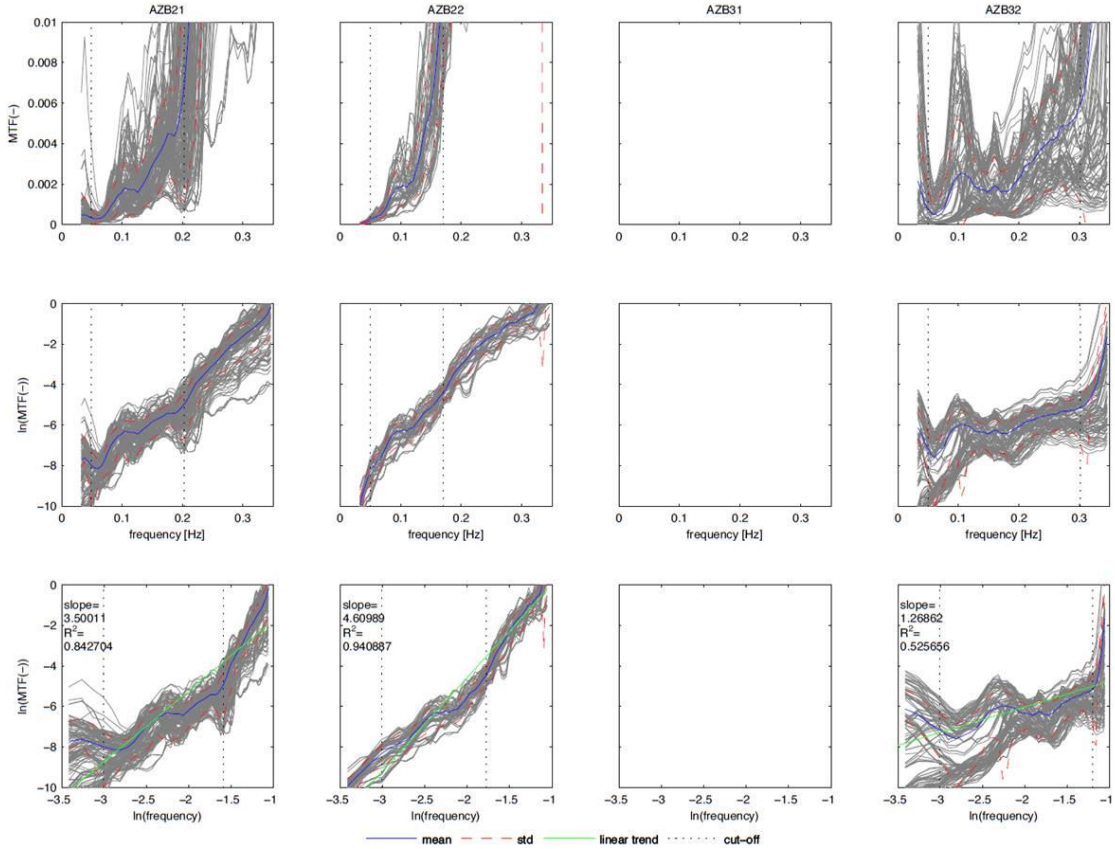

Figure A8. The individual (grey) and final (blue) MTF(s) as ratio of buoy and radar 1D spectrum with corresponding standard deviation (red) at the four different buoy locations. The log axis (middle) and the log-log axes (bottom) help to show the trend through the final MTF and to find the power b of MTF~f^b. The vertical dashed lines indicate the cut-off frequency of each MTF.

Radar wave spectra

As example, Figure A9 shows image spectra converted to wave spectra at the four buoy locations for the five SWAN run moments, using MTF 32.

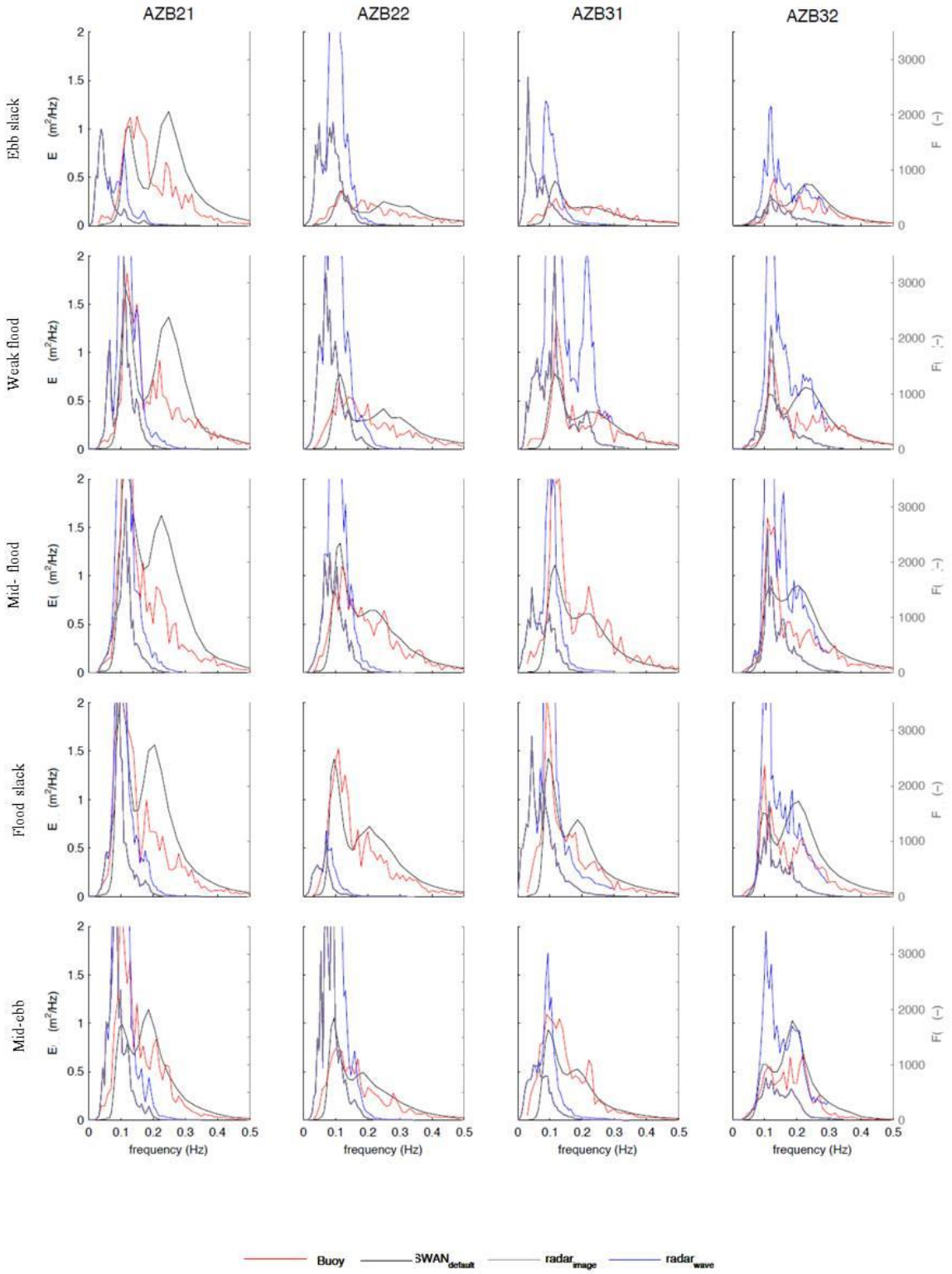

Figure A9. Radar image spectra (grey) converted to wave spectra (blue) at the four inlet buoys at 28 January 2010 (exact time in Table 5a), for comparison buoy (red) and SWAN (black) spectra are shown.

Wave height correlation

Radar derived wave height correlates best to buoy significant wave height at all buoy locations when using MTF32 to transfer the image spectra (Figure A10, Table 6b). Despite the poor correlations it supports the choice to use MTF32 as generally applicable MTF.

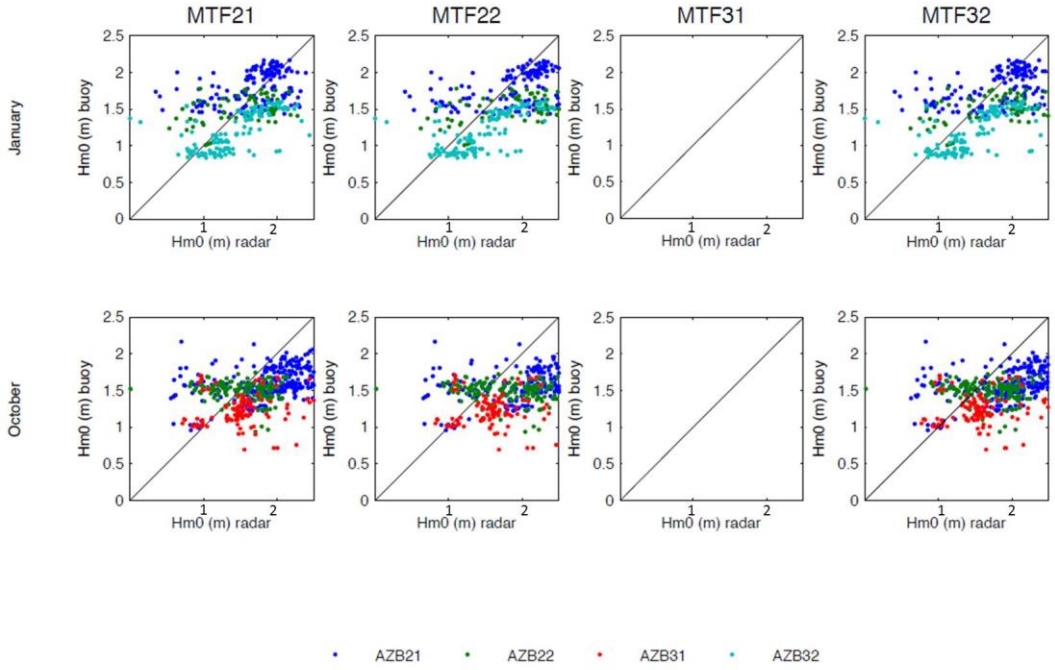

Figure A10.Correlations between buoy and radar wave height in January (top) and October. Using different MTF's (left to right) MTF32 gives the most accurate wave height at all buoy locations (colors). MTF31 was not found.

A4 Sensitivity analysis

SWAN, run with the settings of Section 5.2, predicted the peak frequency and the corresponding wave energy quite well at the four buoy locations within the radar view area at the five run moments in January (Figure A11). Modelled shoreward energy decrease is similar to the energy decrease in the buoy measurements in the inlet (AZB 31, AZB 32) and on the ebb delta (AZB 22). SWAN overestimated the second harmonic at the channel buoy locations (AZB 21, AZB 32), especially during low tide and mid-ebb. An abruptly low dominant wave period was observed in the ebb channel when the second harmonic overpasses the first harmonic in the spectrum (Figure A11 at AZB32 during mid-ebb, Figure 6.3e).
Sensitivity of SWAN on the energy distribution was tested by runs without current, wind or triad wave-wave interactions, giving the following results:

- 1D spectra from SWAN run without current (cyan line) input were quite similar to spectra from SWAN run with default settings for the first and fourth run moment obviously, during ebb and flood slack respectively (Figure A11; Figure 5.4).
- The wind effect was negligible at the buoy locations in the Ameland Inlet during this January and October storm as SWAN running with a very low wind velocity (0.1m/s (for G1 and G2 grid)) (green line) shows hardly any difference with respect to running SWAN with wind. The spectra at AZB 32 do show wind waves were partially locally generated (probably in the ebb channel), since the high frequent energy peak reduced without (strong) wind input. Overall local wave generation was negligible for the Ameland Inlet, during these moderate storms with a wind velocity of approximately 11m/s.
- When no triad wave-wave interactions were included in the SWAN runs, the wave energy did not distribute over higher frequencies (blue line).

Concluding SWAN, including triad wave-wave interaction, appears to predict the waves and their interference accurately in a shoaling area (AZB 22, AZB 31). However SWAN overestimated the high frequent peak in the spectra in the (deeper) ebb channel, which spectra were already deformed by triad interactions.
The bathymetry with alternating shoals and channels might be too complex to predict the frequency-energy distribution accurately. The triad interaction may be too strong incorporated in SWAN or too much simplified by the Lumped Triad Approximation in SWAN for such bathymetries. In addition some physical process in SWAN might amplify the second (or higher) harmonics too much (especially in the ebb channel AZB 21, AZB 32).

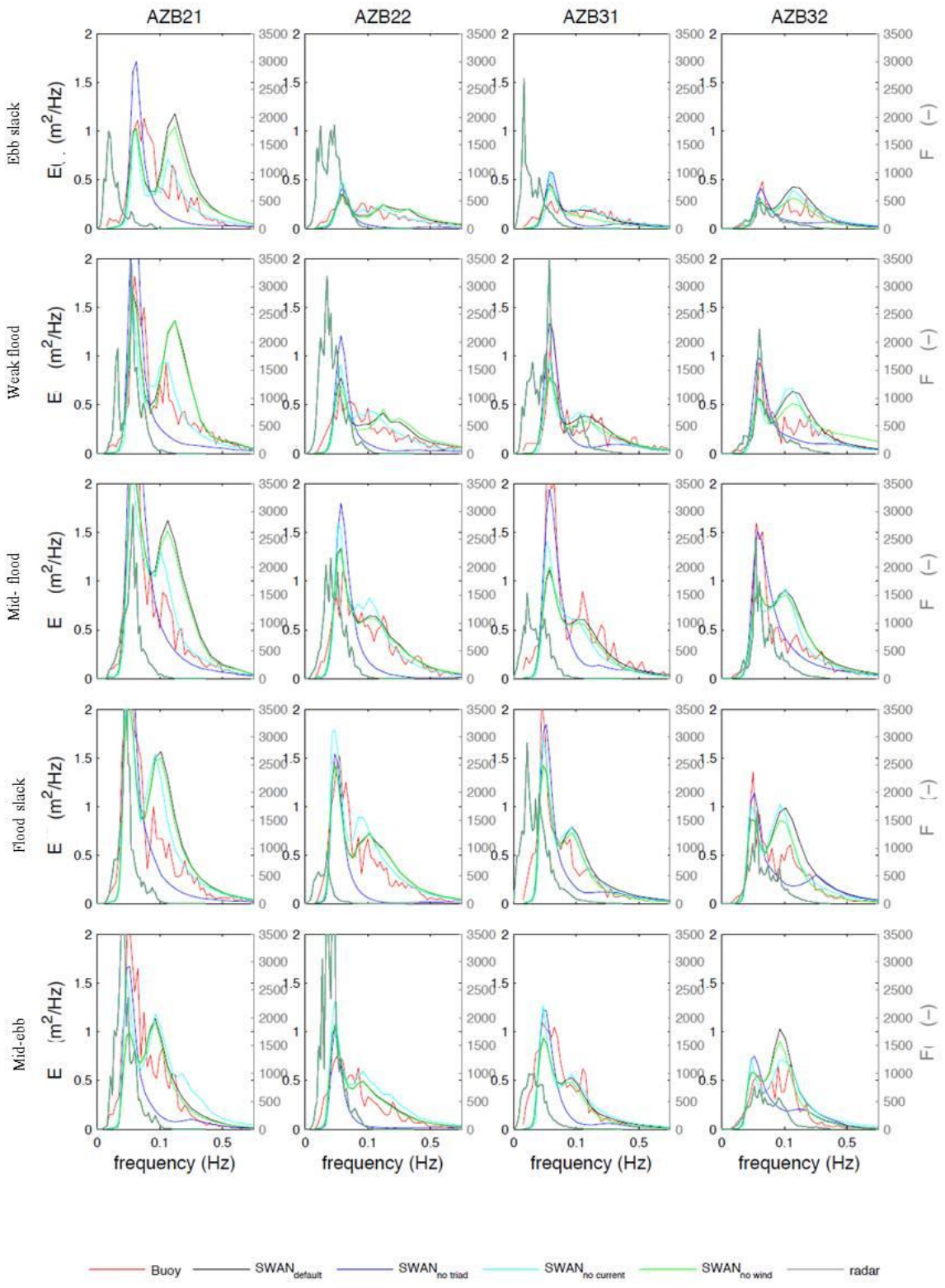

Figure A11. Sensitivity tested for the energy distribution over the frequency axis at the four inlet buoys during five moments in January. SWAN with default settings (black) overestimates the high frequent peak, when compared to the ground truth buoy spectra (red). SWAN without currents (cyan) or without wind (green) has hardly any effect on the high frequent peak. When triads were excluded (blue) the high frequent peak removed entirely. Also radar image spectra (grey) are shown.

Selection of settings

The sensitivity analysis motivated to select the unchanged model settings (Section 5.2) as default for the radar-SWAN comparison. The overestimated high frequent peak in the ebb channel cannot be solved yet. Excluding current, wind or TRIAD wave-wave interactions did not improve the model results. However the high frequent peak was removed entirely when excluding TRIAD wave-wave interactions, providing a correct peak and dominant wave period and overestimated energy at the first harmonic. Wave-wave interactions were still included in the default settings because neglecting wave-wave interaction seems to be physically not correct.

A5 SWAN-radar spectra comparison

Figure A9 shows 1D spectra from the radar and from SWAN with default settings.

- Generally the radar wave energy peak was higher than the SWAN (or buoy) wave energy peak.
- SWAN predicted a second harmonic, which is only observed in the radar wave energy spectra of AZB 32 (and not at AZB 21, AZB 22 and AZB 31). The (transferred) radar spectra correspond well to SWAN at AZB 32, although the first harmonic of the radar was much higher.

  Wave energy at the second harmonic of the SWAN spectrum might be overestimated. On the other hand the lack of high frequent energy at AZB 21 and AZB 22 in the radar spectra can be explained by the shadowing effect for which the MTF is compensating; short waves were shadowed by higher waves especially at far ranges.
- At AZB 22 and AZB 31, the image energy often peaked at lower frequencies than the measured (buoy) or predicted (SWAN) wave energy. This low frequent raw radar spectra at AZB 22 and AZB 31 may be caused by imaging or processing distortions by a quality reduction factor. Unsurprisingly those buoys were located in the zones (Terschelling shoreline and northern edge of the ebb delta) where many outliers were removed by the data filters. All five 1D spectra at AZB 22 and AZB 31 were removed by filtering, except the mid-flood and mid-ebb spectra at AZB 22 (Table 6a).

Overall the radar and SWAN spectra correspond poorly at the buoy locations due to (1) the in SWAN overestimated high-frequent peak at the channel buoys AZB 21 and AZB 32 and (2) the image intensity peaked at a quite low frequency at buoy AZB 22 and AZB 31 by a quality reduction factor.

Tables

Name		Buoy measurements	X [m]	Y [m]	Bed level + NAP [m]
AZB 21	January	Directional Waverider	167307	610978	-9,1
	October		167307	610978	-6,7
AZB 22	January	Non directional Waverider buoy	170688	611040	-3,5
	October		170700	610983	-3,4
AZB 31	January	Directional Waverider	168318	606745	-3,25
	October		168440	606982	-7,6
AZB 32	January	Directional Waverider	169349	607115	-10,7
	October		169519	607141	

Table 4a. Wave buoy measurements in the Ameland Inlet. The buoys has slightly different locations in October 2010 compared to January 2010, because the buoys were removed in the meantime for maintenance. Bed level was given in the buoy .txt files.

Properties	Value
Antenna length +NAP [m]	58
Scanner type	Terma
Scanner width [ft]	18
Range [km]	7,5
Rotation time [s]	2,85
Pulse frequency [GHz]	9,6
Pulse length [ns]	50
Wavelength [cm]	3
Output power [kW]	25
Antenna beam width at 3dB [deg]	19 vertical, 0,41 horizontal
Polarization	HH

Table 4b. Technical characteristics of the X-band radar at the lighthouse of Ameland.

moment		tidal stage	waterlevel [m] +NAP	wind dir [deg]	wind speed [m/s]	H_{rms} [m] at AZB 11
28-Jan	0:40	ebb slack	-0,29	335	10,1	3
28-Jan	2:10	weak flood	-0,06	330	12,3	3,4
28-Jan	4:40	mid-flood	1,15	325	10,9	3,19
28-Jan	6:50	flood slack	1,7	320	9,6	3,21
28-Jan	8:20	mid-ebb	1,29	315	8,4	3,4
20-Oct	10:00	mid-ebb	0,86	335	11	1,96
20-Oct	17:10	(mid-)flood	0,91	330	14,4	4,01
23-Oct	8:00	flood slack	1,16	190	12,7	4,29

Table 5a. Sea and wind conditions during the eight SWAN run moments. The water level was measured at Nes, wind direction follows from the Wierumergronden station, the wind speed is used from the Huibertgat station.

Grid	frequency [Hz]	# frequencies	#cells	cells size ROI [m]
G1	0,03:1,5	42	391x161	400
G2	0,03:2,5	47	286x380	40

Table 5b. Frequency and spatial resolutions (in the Region Of Interest) of the large G1 grid and the nested G2 grid.

	Radar data provided					Analysis by Nortek: computational cubes				
	start time UTC	**end time UTC**	**data**	**#output loc.**	**Length timeseries**	**ΔT [min]**	**#images**	**Pixel size [m]**	**#Pixel**	**Length [m]**
January	27 01 19:16:35	08 01 09:49:26	L, T, θ	946	1:79	12	32	7,5	128	960
	27 01 17:25:53	28 01 09:58:41	spectra	4	1:260	4	32	7,5	128	960
	28 01 02:11:09		spectra	387	1	0	32	7,5	256	1920
October										
	18 10 23:16:01	24 10 01:09:07	L, T, θ	946	1:446	12	32	15	128	1920
	24 10 01:09:07	24 10 09:31:25	L, T, θ	946	447:492	12	32	7,5	128	960
	18 10 23:24:21	20 10 13:09:21	spectra	4	1:589	4	32	7,5	128	960
	20 10 13:09:21	24 10 01:09:07	spectra	4	590:840	4	32	15	128	1920
	24 10 01:09:07	24 10 08:56:47	spectra	4	841:883	4	32	7,5	128	960

Table 4c. Temporal and spatial resolutions of the wave characteristics and image spectra provided by Nortek (left). The right shows the number and the size of radar images for each computational cube (analysis by Nortek).

		AZB21			AZB22			AZB31			AZB32		
moment		**buoy**	**radar**	**SWAN**	**buoy**	**radar**	**SWAN**	**buoy**	**radar**	**SWAN**	**buoy**	**radar**	**SWAN**
28-Jan	00:43:03	1.57	0.81	1.77	0.99	1.67	1.04	0.95	1.05	0.99	0.96	1.21	1.12
28-Jan	02:07:11	1.79	2.04	2.02	1.29	1.94	1.39	1.36	2.45	1.35	1.29	1.92	1.46
28-Jan	04:43:24	2.09	2.03	2.35	1.62	1.84	1.72	1.90	1.33	1.60	1.55	2.06	1.72
28-Jan	06:54:42	2.00	2.08	2.17	1.67	0.64	1.73	1.62	1.71	1.65	1.45	1.80	1.70
28-Jan	08:24:36	1.80	2.17	1.65	1.32	2.24	1.41	1.55	1.09	1.35	1.22	1.61	1.48
20-Oct	10:00:00	1.68	2.47	1.22	1.06	1.80	0.77	1.17	1.91	1.03	NaN	1.81	1.06
20-Oct	17:00:00	1.88	2.31	2.00	1.41	2.10	1.31	1.36	0.99	1.40	NaN	0.96	1.64
23-Oct	08:00:00	1.36	1.44	1.41	1.47	1.56	1.40	0.99	1.77	0.97	NaN	2.16	1.09

Table 6a. Wave height from buoy measurements, radar and SWAN compared at the SWAN run moments in January and October. MTF 32 was used for wave height derived from radar image spectra. Wave height highlighted in grey indicates the corresponding radar spectrum was filtered out.

		AZB21		AZB22		AZB31		AZB32	
		January	**October**	**January**	**October**	**January**	**October**	**January**	**October**
MTF21	Correlation coefficient	0.32	0.55	0.41	-0.24	NaN	0.24	0.63	NaN
MTF22		0.32	0.53	0.42	-0.24	NaN	0.23	0.65	NaN
MTF31		NaN	NaN	NaN	NaN	NaN	NaN	NaN	NaN
MTF32		0.38	0.59	0.42	-0.22	NaN	0.24	0.62	NaN
MTF21	Bias [m]	0.08	-0.43	-0.08	-0.04	NaN	-0.37	-0.26	NaN
MTF22		-0.16	-0.78	-0.35	-0.31	NaN	-0.50	-0.34	NaN
MTF31		NaN	NaN	NaN	NaN	NaN	NaN	NaN	NaN
MTF32		-0.03	-0.61	-0.24	-0.19	NaN	-0.40	-0.32	NaN
MTF21	Symmetric slope	1.02	0.77	0.92	0.95	NaN	0.75	0.79	NaN
MTF22		0.89	0.66	0.78	0.81	NaN	0.70	0.75	NaN
MTF31		NaN	NaN	NaN	NaN	NaN	NaN	NaN	NaN
MTF32		0.95	0.71	0.84	0.86	NaN	0.74	0.76	NaN
MTF21	Scatter index	26.08	23.72	27.05	28.77	NaN	30.63	27.43	NaN
MTF22		27.16	24.28	27.04	28.75	NaN	30.51	28.92	NaN
MTF31		NaN	NaN	NaN	NaN	NaN	NaN	NaN	NaN
MTF32		26.50	24.17	26.41	27.23	NaN	29.63	27.13	NaN

Table 6b. Statistics of buoy and radar inferred H_{m0}, calculated by using a MTF derived from filtered spectra at the buoy locations within the radar view area. All spectra at AZB31 were filtered out in January, thus no MTF was computed. No data was available for AZB 32 in October.

References

Alkyon, 2006. The integration of remote sensing and numerical modelling. A comparison of SHIRA and SWAN, Project GBP 2002-10, Alkyon report A1101.

Alpers, W., Hasselmann, K., 1982. Spectral signal to clutter and thermal noise properties of ocean wave imaging synthetic aperture radars. International Journal Of Remote Sensing 3: 423 446.

Bakker, A.T.M., 2012. Infragravity waves - propagation, dissipation and sediment transport in the inner surf zone of a low sloping beach. Utrecht University, MSc thesis.

Bartholomä, A., Soo Son, C., Flemming, B.W., 2011. Evidence for sediment recirculation on an ebb-tidal delta of the East Frisian barrier-island system, southern North Sea. Geo Marine Letter. DOI 10.1007/s00367-010-0217-0217-8.

Battjes, J.A., Janssen, J.P.F.M., 1978: Energy loss and set-up due to breaking of random waves, Proc. 16th Int. Conf. Coastal Engineering, ASCE, 569-587.

Bell, P.S., 1999. Shallow water bathymetry derived from an analysis of X-band marine radar images of waves. Coastal Engineering 37: 513–527.

Bertin, X., Fortunato, A.B., Oliveira, A., 2009. A modeling-based analysis of processes driving wave-dominated inlets. Continental Shelf Research 29: 819–834.

Booij, N., Ris, R.C., Holthuijsen, L.H., 1999. A third generation wave model for coastal regions, Part I, Model description and validation, Journal of Geophysical Research, 104, C4, 7649-7666.

Bruun, P. and Gerritsen, F., 1959. Natural bypassing of sand at coastal inlets. Journal of Waterway and Harbor Division 85(4):75-107.

Cheung, K.F., Gerritsen, F., Cleveringa, J., 2007. Morphodynamics and sand bypassing at Ameland Inlet, The Netherlands. Journal of Coastal Research 23: 106-118.

Chowdhury, M.Z.R., 2007. Assessment of water flow and the impact on sediment motion in a tidal channel of North Sylt basing on radar observation. Dissertation.

Cleveringa, J., Mulder, S., Oost, A., 2004. Kustverdediging van de Waddeneilanden. De dynamiek van de kust nabij buitendelta's en passende maatregelen voor het kustbeheer. Rijkswaterstaat RIKZ, rapport RIKZ/2004.017, pp. 69.

Dissanayake, D.M.P.K.,Roelvink, J.A., Van der Wegen, M., 2009. Modelled channel patterns in a schematized tidal inlet. Coastal Engineering 56: 1069–1083.

De Fockert, A., Stive, M.J.F., Wang, Z.B., Luijendijk, A.P., De Ronde, J.G., De Boer, G.J., 2008. Impact of relative sealevel rise on the Amelander Inlet morphology. Technical University of Delft, MSc thesis.

De Swart, H.E., Zimmerman, J.T.F., 2009. Morphodynamics of tidal inlet systems. Annual review Fluid Mechanics, 41:203-229.

Deltares (2010). SBW Wadden Sea 2009, Wave hindcast of the storm of 31 January 2008, Deltares Report 1200114-005-HYE-0004 dd 8 February 2010.

Ehlers, J. 1988. The Morphodynamics of the Wadden Sea. Rotterdam: Balkema.

Eldeberky, Y., 1996. Non-linear transformation of wave spectra in the nearshore zone. Delft Technical University, PhD Thesis.

Elias, E.P.L., Van der Spek, A.J.F., 2006. Long-term morphodynamic evolution of Texel Inlet and its ebb-tidal delta (The Netherlands). Marine Geology 225: 5-21.

FitzGerald, D.M., 1988. Shoreline erosional- depostional processes associated with tidal inlets. Lecture notes on Coastal and Estuarine Studies 29: 186-220.

FitzGerald, D.M., 1982. Sediment bypassing of mixed energy tidal inlets. Am. SOC. Civ.Eng., Proc. 18th Conf. Coastal Engineering, pp.1848-1861.

FitzGerald, D.M., Hubbard, D.K. and Nummedal, D., 1978. Shoreline changes associated with tidal inlets along the South Carolina Coast. Coastal Ocean Div., Am. SOC. Civ.Eng., Coastal Zone 78, San Francisco, Calif., 1973-1994.

FitzGerald, D.M., Penland, S., Nummedal, D., 1984. Control of barrier island shape by inlet sediment bypassing: East Frisian islands, west Germany. Marine Geology, 60:355-376.

Flampouris, S., Ziemer, F., Seemann, J., Accuracy of Bathymetric Assessment by Locally Analyzing Radar Ocean Wave Imagery (February 008), IEEE Transactions on Geoscience and Remote Sensing 46(10): 2906 – 2913.

Gautier, C. and Arab (2011). Comparison SWAN, PHAROS and radar wave observations' Report 1204199-002-HYE-0009, Deltares.

Gautier, C., Westhuysen, A., 2010. Wave propagation under influence of currents. Report 1202119 003-HYE-0002, Deltares.

Grilli, S.T., 1998. Depth inversion in shallow water based on nonlinear properties of shoaling periodic waves. Coastal Engineering 35, 185–209.

Hasselman, K., Alpers, W., Barick, D., Crombie, D., Flachi, C., Fung, A., Van Hutten,. Jones, H.W, De Loor, G.P., Lipa, B., Long, R., Ross, D., Rufenach, C., Sandham, W., Shemdin, O., Teague, C., Trizna, D., Valenzuela, G., Walsh, E., Wentz, F., Wright, J., 1978. Radar measurements of wind and waves. Boundary- Layer Meteorology 13: 405-412.

Hessner, K.,Nieto Borge, J.C., 2005. Comparison of WAMOS II with in-situ measurements. In Measuring and analyzing the directional spectra of ocean waves. Ed. Hauser, D., Kahma, K., Krogstad, H.E., Lehner, S., Monbaliu, J.A.J. Wyatt, L.R., Europian Cost Action 714. Luxembourg, pp. 465.

Hessner, K., Reichert, K., 2007. Sea surface elevation maps obtained with a nautical Xband radar Examples from WaMoS II stations, 10th International Workshop on Wave Hindcasting & Forecasting.

Hoekstra, G.W., Van der Vlugt, A.J.M., 2000. Golfmetingen met SHIRA in Petten. Rijkswaterstaat/RIKZ, rapport Radac R99031 v2.1, pp. 38.

Holthuijsen, L.H., 2007. Waves in Oceanic And Coastal Waters. Cambridge University Press, pp.387.

Lillesand, T.M., Kiefer, R.W., Chipman, J.W., 2008. Remote Sensing and Image interpretation, 6ed. Hoboken: Wiley

Masselink, G., Hughes, M.G., 2003. Introduction to coastal processes and geomorphology. London: Hodder Education.

Mattie, M.G, Harris, D.L., 1979. A system for using radar to record wave direction. Techn. 79-1, U.S. Army Corps of Eng., Coastal Engineering Res. Ctr. Fort, Belvair., 50pp.

Nieto Borge, J.C., 2002. Use of nautical radar to study wave fields. German Aerospace Center Remote Sensing Technology Institute. Presentation2nd workshop on water waves, Berlin.

Nieto Borge, J.C., Hessner, K., Jarabo-Amores, P., De La Mata-Moya, D., 2008. Signal-to-noise ratio analysis to estimate ocean wave heights from X-band marine radar image time series. Radar, Sonar and Navigation 2:35-41.

Nieto Borge, J.C., Reichert, K., Dittmer, J., 1999. Use of nautical radar as a wave monitoring instrument. Coastal Engineering 37: 331–342.

Nieto Borge, J.C., Rodriguez, G.R., Hessner, K., Gonzalez, P.I., 2004. Inversion of Marine radar images for surface wave analysis. Journal of Atmospheric and Oceanic Technology 21: 1291-1300.

Nieto Borge, J. C., Sanz González, R., Hessner, K., Reichert, K., and Guedes Soares, C., 2000. Estimation of sea state directional spectra by using marine radar imaging of sea surface. Proc., 19th Int. Conf.on Offshore Mechanics and Arctic Engineering, Paper OMAE2000/S&R-6120.

Nieto Borge, J.C., Soares, C.G., 2000. Analysis of directional wave fields using X band navigation radar. Coastal Engineering 40. 375–391.

Oertel, G.F., 1977. Geomorphic cycles in ebb deltas and related patterns of shore erosion and accretion. Journal of Sedimentary Petrology 47-3: 1121-1131.

Pacheco, A., Ferriera, O., Williams, B., Garel, E., Vila-Concejo, A. Dias, J.A., 2010. Hydrodynamics and equilibrium of a multiple-inlet system. Marine Geology 274: 32-42.

Peters, H. Zeemetingen m.b.v. een navigatieradar op de kust in het kader van SBW Waddenzee. Presentation RWS, april 2010.

Reichert, K., Hessner, K., Dannenberg, J., Traenkmann, I., 2006: X-Band radar as a tool to determine spectral and single wave properties: Proceedings of OMAE2006, Hamburg, Germany.

Reichert, K., Nieto, J.C.N., Dittmer, J., 1998. WaMoS II: an operational wave monitoring system. Proceedings of the Oceanology ’98 conference, (Brighton, England) 3: 455–462.

Ris, R.C., L.H., Holthuijsen, Booij, N., 1999. A third-generation wave model for coastal regions. 2. Verification. Journal of Geophysical Research 104 (C4): 7667-768.

Robin, N., Levoy, F., Monfort, O., Anthony, E., 2009. Short-term to decadal-scale onshore bar migration and shoreline changes in the vicinity of a megatidal ebb delta. Journal of Geophysical Research 114: F04024, doi:10.1029/2008JF001207, 2009.

Ruessink , B.G, Bell, P.S., Van Enckevort, I.M.J., Aarninkhof, S.G.J., 2002. Nearshore bar crest location quantified from time-averaged X-band radar images. Coastal Engineering 45(1): 19-32

Senet C.M., Seemann, J., Flampouris, S., Ziemer, F.,2008. Determination of Bathymetric and Current Maps by the Method DiSC Based on the Analysis of Nautical X-Band Radar Image Sequences of the Sea Surface. IEEE Transactions on Geoscience and Remote Sensing 46-8:2267-2279.

Sha, L.P., 1989a. Sand transport patterns in the ebb-tidal delta off Texel Inlet, Wadden Sea, The Netherlands. Marine Geology 86: 137-154.

Sha, 1989b. Variation in ebb-delta morphologies along the West and East Frisian Islands, The Netherlands and Germany. Marine Geology 89: 11-28.

Sha, L.P., Van den Berg, J.H., 1993. Variation in ebb-tidal delta geometry along the coast of The Netherlands and the German Bight. Journal of Coastal Research 9 (3), 730–746.

Shemdin, O.H., Brown, W.E.Jr., Staudhammer, F.G., Shuchman, R., Rawson, R., Zelenka, J., Ross, D.B., McLeish, W., Berles, R.A., 1978. Comparison of in-situ and remotely sensed ocean waves off Marineland, Florida. Boundary Layer Meteorology 13: 193-202.

Shi, F., Hanes, D.M., Kirby, J.T., Erikson, L., Barnard, P., Eshleman, J. Pressure gradient-driven nearshore circulation on a beach influenced by a large inlet-tidal shoal system. Journal of Geophysical Research 116: C04020, doi:10.1029/2010JC006788, 2011.

Steetzel, H., 1995. Voorspelling ontwikkeling kustlijn en buiten-delta's waddenkust over de periode 1990–2040. Delft Hydraulics report no. H1887 prepared for Rijkswaterstaat. The Hague, The Netherlands.

SWAN Technical documentation, SWAN cycle III version 40.51.

Swinkels, C.M., 2011. Storm Hindcast January 2010. Analysis of the application of radar current data for hindcast purposes. Report 1202119-001-HYE-0003.Version 2, Deltares.

Valenzuela, 1978. Theories for the interaction of electromagnetic and oceanic waves- a review. Boundary-Layer Meteorology 13:61-85.

Van Dongeren, A.R., Van der Westhuysen, A.J., Van Vledder,G.P., Wenneker, I., 2009. Penetration of North Sea waves into the Wadden Sea SBW-Waddenzee - phase 3: fallback options. Report 1200114-002 Final, Deltares.

Van Heesen, J., Kleijweg J., 2010. Toelichting resultaten Amelander Zeegat. Presentation RWS DID, april 2010.

Van Rijn (1989). Principles of Fluid flow and surface wave s in ricer, estuaries, seas and oceans. Aqua publications.

Van Rijn, L.C. (2007). Unified view of sediment transport by currents and waves. 1:Initiation of motion, bed roughness, and bed-load transport. ASCE, 2007.

Wenzel, L. B., 1990: Electromagnetic scattering from the sea at low grazing angles. In Surface Waves and Fluxes, G. L. Geernaert and W. J. Plant, Eds., Kluwer Academic, 41–108.

Wright, J. W., 1966. Backscattering from capillary waves with application to sea clutter. I2.6 Transactions. AF-14, 749-754.

Wyatt, L.R., Green, J.J., Gurgel, K.-W., Nieto Borge, J.C., Reichert, K., Hessner, K.,Günther, H., Rosenthal, W., Saetra, O., Reistad, M.,2003. Validation and intercomparisons of wave measurements and models during the EuroROSE experiments. Coastal Engineering 48:1-28.

Young, I.R., Rosenthal, W., Ziemer, F., 1985. A three dimensional analysis of marine radar images for the determination of ocean waves directionality and surface currents. Journal of Geophysical Research 90:1049-1059.